UNIVERSITÀ DELLA CALABRIA

**UNIVERSITÀ DELLA CALABRIA**

Dipartimento di Ingegneria Civile

**Dottorato di Ricerca in**

Ingegneria Civile e Industriale

**CICLO**

XXIX

# Turbulence characteristics in open-channel flows with highly rough beds

**Settore Scientifico-Disciplinare**

**ICAR/01-Idraulica**

**Coordinatore:** Ch.mo Prof. Ing. Franco Furgiuele

Firma _____

**Supervisori/Tutor:** Ch.mo Prof. Ing. Roberto Gaudio

Firma _____

Ch.mo Prof. Ing. Costantino Manes

Firma _____

**Dottorando:** Dott. Ing. Domenico Ferraro

Firma _____

I would like to dedicate this thesis to my beloved parents …

# Declaration

I hereby declare that except where specific reference is made to the work of others, the contents of this dissertation are original and have not been submitted in whole or in part for consideration for any other degree or qualification in this, or any other university. This dissertation is my own work and contains nothing which is the outcome of work done in collaboration with others, except as specified in the text and Acknowledgements.

Eng. Ferraro Domenico

October 2017

# Acknowledgements

To my life-coaches, my parents, because I owe it all to you. Thanks you from the bottom of my heart! My eternal gratitude goes to my "patient" and affectionate sister who supports me all the times I need it.

I am grateful to my grandparents, who have provided me moral and emotional support throughout my life. I am also grateful to my other family members who have supported me along the way.

I cannot forget my tireless friends, they are part of my life. The afterwork time was always gladdened thanks to these loving and loved persons. Thanks for every single, disparate but always useful, moment spent together.

Very special gratitude is reserved to my Tutor Prof. Eng. Roberto Gaudio who has supported me with professionality since the beginning of this long path. Of course I wish to thank my supervisor, Prof. Eng. Costantino Manes who encourage me to climb the scales of turbulence. His enthusiasm for this topic is a real inspiration.

I wish to thank Dr. Sergio Servidio who initiated me in a turbulent and passional world. I could never have discovered turbulence without his priceless and highly professional help.

I am also grateful to the laboratory staff for their unfailing support and assistance.

Thank you all for your encouragement!

# Abstract

River motion is one of the most attractive and fascinating phenomena in nature. Since ancient times many scientists have been drawn into a vortex of confusion observing river motion. Flow observation is often simplified, running tests in a laboratory under controlled conditions, in order to test a specific phenomenon of a much more complex issue. A great number of these phenomena has been collected by researchers throughout the history of science, and other researchers have tried to merge the available knowledge to clarify the tangled phenomena. This work is focused on the turbulent characteristics of Open-Channel Flows (OCFs) over a highly rough bed. The use of coarse sediments is an attractive technique to solve many problems in rivers as well as to safeguard aquatic life. Issues like sediment transport phenomena or erosion and local scour, e.g. at bridge piers and abutments, can be counteracted by introducing coarse sediments. In this work the bed roughness effect on the turbulence characteristics of the flow is investigated through the relative submergence parameter $\Delta$, which is the ratio between the roughness characteristic dimension and the water depth. Most of the theories and literature works has been developed for smooth-wall flows and rough-bed flows at very high relative submergence, whereas its applicability in OCFs with low relative submergence remains questionable; the simplest example is the velocity distribution (i.e., the universal logarithmic law). This thesis aims at improving the knowledge of turbulence structure developed over a highly

rough bed in OCFs by varying the relative submergence. According to the relative submergence definition given before, it can be changed by modifying the water depth for a fixed roughness or varying the roughness keeping the water depth constant. The choice settled on the second strategy, because of the measurement instrument configuration. It will be described in detail in the chapter “Experimental equipment and procedures”. The relative submergence varied in the range from 3.13 to 10.07. Three long-duration experiments (each one with a given coarse sediment size) were performed in uniform flow conditions by using a 100 Hz ADV down-looking probe, in order to record the 3D velocity vector in each point of a given grid of measurements. The contribution of the Reynolds stress, the viscous and the form-induced shear stress was analysed, as well as the averaged velocity profiles, second- and third-order moments .

A statistical tool will be proposed to verify the frozen-in Taylor hypothesis by comparing two typical time-scales, namely the large scale advection time and the characteristic nonlinear time. The proposed method based on the characteristic eddies timescales is more restrictive with respect to the classic frozen-in Taylor hypothesis, in which a simple comparison of the flow velocity and the fluctuation magnitude is made.

Furthermore, one-point temporal correlations analysis will be performed in order to give a first indication of the integral scales lengths along the channel varying the relative submergence.

Spectral analysis is introduced both in the frequency and in wavenumber domain. In experimental practice it is quite hard to obtain direct measures, which can allow computing directly a wavenumber spectrum. Temporal velocity signals are commonly recorded in a single point, and they are used to compute the frequency spectrum and then converted to wavenumber spectrum

through the Taylor frozen-in hypothesis. Hence, the $k^{-5/3}$ slope is investigated in the longitudinal velocity spectra. $k$ is the wavenumber.

Spectral analysis will be introduced in order to test the observed $k^{-5/3}$ slope, in order to confirm that the inertial subrange is well visible at the investigated *Re* numbers. Furthermore, the validity of the $-5/3$ scaling region will be also tested by using the third-order longitudinal velocity structure function, which is expressed as a function of the turbulent kinetic energy (TKE) dissipation rate.

The third-order longitudinal velocity structure function will be also used to provide an estimate of the magnitude of the TKE dissipation rate.

In addition, in order to quantify the energy contribution of different eddy-scales, premultiplied spectra will be employed. Thanks to this analysis, the Large Scales (LSs) and the Very Large Scale (VLSs) will be investigated. These scales will be associated with a characteristic wavenumber and intensity.

ADV velocity measurement also allows exploring the longitudinal-vertical velocity co-spectra.

In order to locate the normalized wavenumber associated with the peak in the premultiplied spectra, a systematic procedure to find the correct position of the peaks based on the center of mass concept will be proposed. Moreover, the peak distribution over the water depth will be plotted in inner and outer coordinates.

# Table of contents

# List of figures

# List of tables

# List of Symbols

$a$ Gamma function shape parameter $[-]$
$B$ channel breadth $[\mathrm{L}]$
$b$ Gamma function inverse scale parameter $[\mathrm{L}]$
$c$ celerity of sound in the fluid $[\mathrm{LT}^{-1}]$
$C$ Bernoulli's function $[\mathrm{LT}^{-2}]$
$C$ drag coefficient $[-]$
$C_k$ $2/3$-law constant $[-]$
$d$ characteristic diameter $[\mathrm{L}]$
$d_{50}$ median grain size $[\mathrm{L}]$
$\dot{d}$ vortex dimension $[\mathrm{L}]$
$f$ frequency $[\mathrm{T}^{-1}]$
$f_e$ ADV acoustic wave frequency $[\mathrm{T}^{-1}]$
$f_r$ ADV reflected frequency $[\mathrm{T}^{-1}]$
$F_D$ Drag force $[\mathrm{MLT}^{-2}]$
$Fr$ Froude number $[-]$
$G_{u_i u_i}$ one-sided density spectra $[\mathrm{L}^2\mathrm{T}^{-3}]$
$G_{u_i u_j}$ one-sided density cospectra $[\mathrm{L}^2\mathrm{T}^{-3}]$
$g$ gravitational acceleration $[\mathrm{LT}^{-}2]$
$h_w$ water depth $[\mathrm{L}]$
$K$ Kinetic energy $[\mathrm{ML}^2\mathrm{T}^{-2}]$

$k$ wavenumber $[\mathrm{L}^{-1}]$
$k_x$ streamwise wavenumber $[\mathrm{L}^{-1}]$
$k_s$ mean roughness length $[\mathrm{L}]$
$L$ large eddies length $[\mathrm{L}]$
$l$ characteristic length $[\mathrm{L}]$
$l_t$ largest eddies length $[\mathrm{L}]$
$p$ fluid pressure $[\mathrm{ML}^{-1}\mathrm{T}^{-2}]$
$\bar{p}$ time averaged fluid pressure $[\mathrm{ML}^{-1}\mathrm{T}^{-2}]$
$p'$ fluid pressure fluctuation $[\mathrm{ML}^{-1}\mathrm{T}^{-2}]$
$Q$ flow discharge $[\mathrm{L}^3\mathrm{T}^{-1}]$
$Re$ Reynolds number $[-]$
$Re_{l_t}$ large eddies Reynolds number $[-]$
$Re_\eta$ Kolmogorov Reynolds number $[-]$
$r$ spatial increment $[\mathrm{L}]$
$r_B$ *Burgers* vortex radius $[\mathrm{L}]$
$S$ bed slope $[-]$
$S_{u_iu_i}$ two-sided densities spectra $[\mathrm{L}^2\mathrm{T}^{-3}]$
$S_{u_iu_j}$ two-sided densities cospectra $[\mathrm{L}^2\mathrm{T}^{-3}]$
$S_{int}$ water-bed interface surface in the control volume $[\mathrm{L}^2]$
$T_u$ Free-stream turbulence $[-]$
$t$ time $[\mathrm{T}]$
$\mathfrak{T}$ time-lag $[\mathrm{T}^2]$
$U_{\mathrm{inf}}$ mean free-stream velocity $[\mathrm{LT}^{-1}]$
$\mathbf{u}$ full three-dimensional velocity vector $[\mathrm{LT}^{-1}]$
$u$ instantaneous velocity in $x$ direction $[\mathrm{LT}^{-1}]$
$\bar{u}$ time averaged $u$ velocity component $[\mathrm{LT}^{-1}]$
$u'$ velocity fluctuation of instantaneous velocity $[\mathrm{LT}^{-1}]$
$u_i''$ spatial disturbance in the velocity fluctuation $[\mathrm{LT}^{-1}]$

$\tilde{u}$ spatial perturbation in time-averaged velocity [$LT^{-1}$]
$\hat{u}$ velocity fluctuation in space decomposition [$LT^{-1}$]
$u_\eta$ Kolmogorov microscale velocity [$LT^{-1}$]
$u_r$ velocity at the elevation $z_r$ [$LT^{-1}$]
$u_{rms}$ rout mean square velocity [$LT^{-1}$]
$u_T$ large eddies velocity [$LT^{-1}$]
$u_R$ hydraulic radius shear velocity [$LT^{-1}$]
$u_{h_w}$ water depth shear velocity [$LT^{-1}$]
$u_*$ shear velocity at crest level [$LT^{-1}$]
$\dot{u}$ orbital velocity [$LT^{-1}$]
$v$ instantaneous velocity in $y$ direction [$LT^{-1}$]
$\bar{v}$ time averaged $v$ velocity component [$LT^{-1}$]
$V_0$ total volume a fixed region [$L^3$]
$V_f$ volume occupied by fluid within a fixed region [$L^3$]
$w$ instantaneous velocity in $z$ direction [$LT^{-1}$]
$\bar{w}$ time averaged $w$ velocity component [$LT^{-1}$]
$x$ streamwise direction [L]
$\mathbf{x}_*$ probe position [$-$]
$y$ spanwise direction [L]
$z$ vertical direction [L]
$z_c$ maximum grain crest level [L]
$z_r$ upper bound elevation of the roughness layer [L]
$\hat{z}$ dimensionless elevation [$-$]
$\Gamma$ Gamma function [$-$]
$\Delta$ relative submergence [$-$]
$\varepsilon$ kinetic energy dissipation rate per unit of mass and time [$L^2T^{-3}$]
$\eta$ Kolmogorov microscale length [L]
$\kappa$ von Kaŕma'constant [$-$]

$\lambda$ Taylor microscale length [L]
$\lambda_c$ correlation length [L]
$\lambda_e$ ADV acoustic wavelength [L]
$\lambda_r$ ADV reflected wavelength [L]
$\mu$ dynamic viscosity coefficient [$ML^{-1}T^{-1}$]
$\nu$ kinematic viscosity coefficient [$L^2T^{-1}$]
$\rho$ water density [$ML^{-3}$]
$\rho_s$ sediments density [$ML^{-3}$]
$\sigma$ standard deviation of a variable
$\tau$ total shear stress [$ML^{-1}T^{-2}$]
$\tau_0$ total shear stress at crest level [$ML^{-1}T^{-2}$]
$\tau_\eta$ Kolmogorov temporal scale [T]
$\tau_T$ large eddies temporal scale [T]
$\tau_R$ hydraulic radius shear stress [$ML^{-1}T^{-2}$]
$\tau_{h_w}$ water depth shear stress [$ML^{-1}T^{-2}$]
$\tau_{nl}$ characteristic nonlinear time [T]
$\tau_{\bar{u}}$ large scale advection time [T]
$\Phi_{u_iu_i}$ one-sided wavenumber spectra [$L^2T^{-2}$]
$\Phi_{u_iu_j}$ one-sided wavenumber cospectra [$L^2T^{-2}$]
$\phi_s$ roughness geometry function or porosity [$-$]
$\psi$ Taylor frozen-in parameter [$-$]
$\omega$ three dimensional vorticity vector [$T^{-1}$]
$\omega'$ rms of the vorticity fluctuation [$L^{1/2}T^{-1/2}$]
$\omega_x$ vorticity in $x$ direction [$T^{-1}$]
$\omega_y$ vorticity in $y$ direction [$T^{-1}$]
$\omega_z$ vorticity in $z$ direction [$T^{-1}$]
$C_{u_iu_i}$ auto-covariance function
$C_{u_iu_j}$ cross-covariance function

$R_{u_i u_i}$ auto-correlation function

$R_{u_i u_j}$ cross-correlation function

$\mathbb{E}$ expected value of a variable

$\langle\rangle$ double average operator

# Chapter 1

# Introduction

*"In rivers, the water that you touch is the last of what has passed and the first of that which comes; so with present time."*
*Leonardo da Vinci*

River motion is one of the most attractive and fascinating phenomena in nature. Since ancient times many scientists have been drawn into a vortex of confusion observing river motion.

The first one to discover the turbulent nature of water flow in a river was Leonardo da Vinci in a writing titled *La Turbolenza* (15th century). In this essay, da Vinci splits the flow into two components: the former describes the mean flow, the latter the chaotic movement of the fluid particles. This approach sounds familiar to modern scientists. In fact, 400 years after da Vinci, this idea was rediscovered by Reynolds at the end of the 19th century and applied to the Navier-Stokes equations, giving rise to the most famous approach in fluid dynamics.

A set of complex phenomena is always found in a natural watercourse. Complex thalweg paths, complex cross-section geometry, vegetated paths,

coarse sediment paths, structures interfering with water (such as bridge piers or abutments): all these aspects make it very hard to predict the flow evolution.

The influence of the different hydraulic characteristics is often investigated under controlled conditions in a laboratory, by changing each parameter and keeping the others constant. Simplifications are adopted, i.e. complex thalweg paths become straight in a flume, complex cross-section geometry is often neglected in channels of regular cross-sections, varied flow is studied as steady-uniform flow, the presence of structures interfering with the flow is not considered, and the flume bed is compounded only by coarse sediments, randomly but uniformly spread on the bottom, neglecting the presence of cohesive sediments.

The present work is focused on the effect of highly rough beds on the flow field and the relevant turbulent quantities. It is important to underline the importance of rough beds in engineering practice, from environmental engineering interventions (e.g., safeguarding of aquatic life) to sediment transport phenomena, countermeasures against erosion and local scour (e.g., at bridge piers/abutments), many phenomena can be addressed by using coarse sediments, as reported in Figure 1.1.

Researchers and engineers need mathematical tools in order to study problems like turbulence. Many techniques were developed in the past, like spectral analysis, which emerged in the 1930s from a regular correspondence between Ludwig Prandtl and Geoffrey Ingram Taylor [30]. Spectral analysis in the related Fourier space is still the most accredited technique to analyze turbulent issues, like the energy cascade, which was formulated by Richardson in the 1920s and later formalized by Kolmogorov in 1941 [50]. Anyway, most of the physical discussions between Kraichnan [81] and Batchelor [10] dealt also with the real space, which is an important and meaningful tool of analysis in turbulence. In particular, Kármán–Howarth [31] derived the

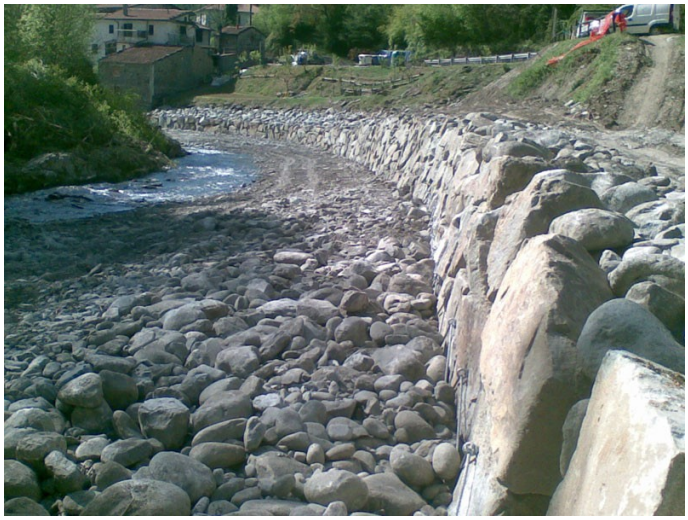

**Figure 1.1:** Example of erosion protection through coarse-sediments coating in *Crespiano Comunita Montana Lunigiana*, Tuscany, Italy

structure function of order $p$, which was used by Kolmogorov [79] to derive his 4/5 law [30].

The knowledge of the involved scales in rivers is also a fundamental question. The wide range of turbulent eddies, present in a river, are large coherent structures, which are commonly called energy containing scales. These coherent structures arise in the bottom boundary layer, where a prominent shear is present, and their generation is due to the interaction between regions with different momentum [50]. Different scales are employed in the mechanisms of sediment entrainment in river flows [126, 20]. For instance, the knowledge of the energy amount through different scales (from larger to smaller) can help to understand how they act on the Reynolds stress. In addition, many efforts in the literature on wall turbulence in OCFs are related to high relative submergence, whereas intermediate and low relative submergence are still an open field of investigation. The present work is based on a laboratory campaign aimed at investigating the effect of highly rough beds

(or, better, relative submergence) on the characteristics of wall turbulence. In particular, it is the intention to characterize the influence of bed roughness on the generation, transport and dissipation of the energy process operated by turbulence. Furthermore, a significant portion of the work will be dedicated to detecting the characteristic scales of turbulence.

Hence, the aim of the thesis is to investigate the effect of a highly rough bed, consisting of granular sediment particles (pebble and gravel), in terms of relative submergence on the properties of turbulent OCFs, specifically:

1. to investigate the influence of the relative submergence on the validity of classical paradigms of wall turbulence, such as the outer layer similarity hypothesis by Townsend (1976) and the occurrence of the log-law of the wall;

2. to investigate the dependence of large scale eddies on the relative submergence, in terms of both size and contribution to the TKE production and momentum transport.

In order to achieve the above aims, Chapter 1 describes the state-of-the-art review on turbulence, starting from the Navier-Stokes (NS) equations, the Reynolds-averaged Navier-Stokes (RANS) equations and the Double-Averaging Method (DAM) to the turbulence characteristics in both real space (Kolmogorov's 4/5 law of turbulence, from which the TKE dissipation rate is assessed) and Fourier space (Kolmogorov's -5/3 law of turbulence, scales of motion). Chapter 2 illustrates the laboratory experiments in which the detailed turbulence measurements were carried out for different relative submergences in turbulent OCFs. Chapter 3 presents preliminary results of the experiments. First of all, the uniform flow condition is verified through the momentum balance, as well as the outer layer similarity hypothesis by Townsend (1976) and the non-occurrence of the log-law of the wall. Chapter 4 presents the

results of the experiments about turbulent analysis. In particular, the Taylor frozen-in approximation is validated through a new statistical tool developed on purpose. Once the Taylor hypothesis is verified, a systematic spectral analysis is proposed. The first step is to identify the inertial subrange, where Kolmogorov's -5/3 law is tested and in which Kolmogorov's 4/5 law is used to compute the TKE dissipation rate. Spectral analysis, in premultiplied form, is extended to all the velocity components, including co-spectra, in order to investigate the dependence of the turbulence scales on the relative submergence. A new method is proposed to locate the peaks in the premultiplied spectra and the analysis is carried out to identify the contribution of LSs and VLSs to the TKE and turbulent momentum transport, by varying the relative submergence within a range of values that are typical of gravel bed flows.

# Chapter 2

# Theoretical background

*"I am an old man now, and when I die and go to heaven*
*there are two matters on which I hope for enlightenment.*
*One is quantum electrodynamics, and the other is*
*the turbulent motion of fluids.*
*And about the former I am rather optimistic."*
*Horace Lamb*

## 2.1 Turbulence phenomena in rivers

To date, two large classes of flow are recognized, laminar flow and turbulent flow. Laminar flow is characterized by the regularity and predictability of the streamlines. A main feature of laminar flow is motion organized in immiscible layers. It occurs at relatively low flow velocity. This kind of flow does not commonly occurs in rivers, which most often show a turbulent motion nature.

Turbulent flow is a mixture of streamlines that have a chaotic motion, which includes continuous impacts of the fluid particles. This motion is more complex than the laminar one and the chaotic nature of the turbulence gener-

ates an unpredictable pattern. The first step to define the motion univocally was made by Reynolds [118], who found a dimensionless group, "*Re*", which relates the inertial forces to the viscous forces (see below). This parameter establishes whether the flow is in laminar condition, for $Re < 10^3$ (viscous forces prevails over inertial forces), or it becomes turbulent, for $Re > 10^6$ (inertial forces prevails over viscous forces). This dimensionless group is known as the *Reynolds number*. Inertial forces are characterized by the product of the density $\rho$ times the mean velocity $\bar{u}$ times the gradient of the velocity $d\bar{u}/dz$. Viscous forces are characterized by the kinematic viscosity coefficient $\mu$ times the second gradient of the velocity $d^2\bar{u}/dz^2$. The Reynolds number *Re* then becomes

$$Re = \frac{\rho\bar{u}}{\mu}\frac{d\bar{u}/dz}{d^2\bar{u}/dz^2},$$

Replacing the velocity gradient with the proportional quantities $d\bar{u}/dz \propto \bar{u}/l$ and $d^2\bar{u}/dz^2 \propto \bar{u}/l^2$. Then

$$Re = \frac{\rho\bar{u}}{\mu}\frac{\bar{u}/l}{\bar{u}/l^2},$$

obtaining:

$$Re = \frac{\rho\bar{u}l}{\mu}. \tag{2.1}$$

High Reynolds numbers indicate that inertial forces prevail over viscous forces and the flow can be considered inviscid. On the other hand, low Reynolds numbers confirm an important role of viscous forces.

## 2.2 Time averaged equations

As a first step, before dealing with relevant equations, a clarification on the continuum hypothesis is needed. Pope [115] demonstrates that, in almost all

the applications in fluid dynamics, the typical time-scales and length-scales allow the continuum hypothesis to be considered as correct. In the next sections, the Navier-Stokes (NS) equation will be presented. It provide the description of the rate of change of momentum of a certain mass of fluid under the action of a system of external forces [9]. They will be completed by the continuity equation (mass-conservation equation). A further equation will be found applying the vector operator *curl* to the NS equation to obtain the vorticity equation.

### 2.2.1 Navier-Stokes equation

The NS equation is universally recognized to describe the momentum balance of all fluid flows according to the continuum hypothesis. They are a generalization of Euler's equation, which is derived for an ideal and inviscid fluid and describe a fluid system characterized by density $\rho(\mathbf{x},t)$, velocity $\mathbf{u}(\mathbf{x},t)$ and pressure $p(\mathbf{x},t)$; at given position ($\mathbf{x}$) and time ($t$).

Here, the NS equation is presented in a tensorial form, which is valid for an incompressible Newtonian fluid characterized by an inability to support shear stresses. In other words, the viscosity effects are introduced in Euler's equations.

$$\rho\frac{\partial \mathbf{u}}{\partial t} = -\rho\mathbf{u}\nabla\mathbf{u} - \nabla p + \rho\mathbf{f} + \rho\nu\nabla^2\mathbf{u} \tag{2.2}$$

where the gradient is represented by the symbol $\nabla$, $\nabla^2$ is the Laplacian operator given by the divergence of the gradient of a function and $\mathbf{f}$ is an external force system.

In equation 2.2, a deterministic character can be observed. How can NS equation describe a turbulent motion which is, conversely, a chaotic motion? This oddity was resolved by Lorentz in 1963, who demonstrated how a nonlinear equation system can suffer from imperceptible perturbations in the

initial conditions to the extent of producing very different solutions [115]. It is possible to manipulate the equation 2.2 in order to make some considerations about the evolution of kinetic energy over time and, consequently, about the effect of the individual terms. According to the definition of kinetic energy ($K$) of an incompressible fluid in a control volume $V$

$$K = \frac{1}{2}\rho \int_V \mathbf{u}\cdot\mathbf{u}dV, \tag{2.3}$$

and its time derivative

$$\frac{dK}{dt} = \rho \int_V \mathbf{u}\cdot\frac{\partial \mathbf{u}}{\partial t}dV, \tag{2.4}$$

multiplying the equation 2.2 by $\mathbf{u}$ and using the continuity equation definition $\nabla\cdot\mathbf{u}$, the kinetic energy variation over time is recognizable at the right hand side (rhs) of equation 2.2

$$\frac{\partial K}{\partial t} = \int_V \left[-\rho\mathbf{u}\nabla(\mathbf{u}\mathbf{u}) - \mathbf{u}\nabla p + \rho\mathbf{u}\mathbf{f} + \mu\mathbf{u}\nabla^2\mathbf{u}\right] dV. \tag{2.5}$$

Some of the terms of equation 2.5 can be rewritten, using again the continuity as

$$\begin{aligned}
\mathbf{u}\nabla(\mathbf{u}\mathbf{u}) &= \frac{1}{2}\nabla\left(\mathbf{u}\left|\mathbf{u}\right|^2\right), \\
\mathbf{u}\nabla p &= \nabla\cdot(p\mathbf{u}), \\
\mathbf{u}\nabla^2\mathbf{u} &= \nabla\cdot\nabla(\mathbf{u}\cdot\mathbf{u}).
\end{aligned} \tag{2.6}$$

Applying the divergence theorem (or Gauss's theorem), after some mathematical derivations and considering that the velocity is zero at the control volume

edge, the following result is achieved

$$\frac{dK}{dt} = \int_V \rho \mathbf{f} \cdot \mathbf{u} dV - \int_V \rho \nu \left|\nabla \mathbf{u}\right|^2 dV, \tag{2.7}$$

in which the last term of equation 2.7 contains the definition of the energy dissipation of kinetic energy in the unit mass

$$\varepsilon = \nu \left|\nabla \mathbf{u}\right|^2 dV. \tag{2.8}$$

The integral form of the kinetic energy equation 2.7 shows a dependence of the volume force and viscous force, leaving no trace of the pressure field or the non-linear term. In other words, the presence of the pressure and convective derivative does not operate on the global budget of kinetic energy, but their presence in the differential equations 2.2 suggests a role in the energy transfer only.

Considering a (statistically) stationary flow, in equation 2.7 the term $dK/dt$ becomes 0 obtaining that $\int_V \rho \mathbf{f} \cdot \mathbf{u} dV = \int_V \rho \varepsilon dV$. Namely, the energy produced by the system is dissipated proportionally to the fluid viscosity. Although it can be asserted that viscosity is not a predominant phenomenon in a turbulent flow (i.e, at high Reynolds numbers), according to the last sentence and the experimental evidences, the kinetic energy is kept constant through the viscosity. This statement suggests that a turbulent flow is also a strongly dissipative motion.

The explanation resides in the scales of motion involved. The energy, extracted at the energy containing scale, is transferred towards a smaller scale until it becomes so much smaller that it is comparable to the viscous scales. Finally, according to the equation 2.7, the energy transferred to the viscous scales can be dissipated, maintaining the system in equilibrium.

A further comment about the NS equation is related to the pressure field. According to Davidson [29] the pressure $p$ can be matched with the velocity vector thanks to its solenoidal nature. This relationship is summarized as

$$p(x) = \frac{\rho}{4\pi} \int \frac{[\nabla \cdot (\mathbf{u} \cdot \nabla \mathbf{u})]'}{|\mathbf{x} - \mathbf{x}'|} d\mathbf{x}'. \tag{2.9}$$

In his book, Davidson [29] highlights that $p$ is no-local in an incompressible fluid, where the pressure travels infinitely fast. Taking into account a space-bounded motion like an "eddy" located in $\mathbf{x}$, it sends out pressure waves, which are felt everywhere in space. Hence, "every part of a turbulent flow feels every other part and this means that eddies which are spatially remote can interact with each other" [29]. The main implication of this view is the fact that the velocity vector $\mathbf{u}$ have no spatial size (it is not localized in a finite space), whereas the turbulent eddies have a definite size. A typical eddy size will be introduced; thus, a new quantity, instead of $\mathbf{u}$, needs to be defined. Hence, the vorticity field $\omega = \nabla \times \mathbf{u}$, which is localized in space, is preferred over the $\mathbf{u}$, which instead can be instantaneously redistributed throughout space by the pressure field [29].

### 2.2.2 Vorticity equation

The energy cascade concept, treated below, foresees an interaction through a vortex set of different dimensions. The Kelvin theorem [72] suggests that a potential flow, with negligible viscous effects, in a conservative force field and isotropic pressure field will remain indefinitely irrotational. Last sentence suggests that a non-swirling flow cannot be a turbulent motion. It is also useful to introduce vorticity and the concept of energy cascade.

The vorticity field is defined by

$$\omega = \nabla \times \mathbf{u}. \tag{2.10}$$

The vorticity equation is a form of evolution equation, which is simpler than NS equation. Although $\mathbf{u}$, $\omega$ cannot be created or destroyed in a control volume, it is transferred throughout the flow field through advection and diffusion. Thus, the term "eddy" in a turbulent flow denotes a blob of vorticity and its associated rotational motion [29].

Applying equation 2.10 to equation 2.2, it can be rearranged in the form

$$\frac{\partial \mathbf{u}}{\partial t} = \mathbf{u} \times \omega - \nabla C + \nu \nabla^2 \mathbf{u}, \quad C = \frac{p}{\rho} + \frac{u^2}{2} \tag{2.11}$$

where $C$ is Bernoulli's function which is identically equal to

$$\nabla \left( \frac{u^2}{2} \right) = (\mathbf{u} \cdot \nabla)\,\mathbf{u} + \mathbf{u} \times \omega \tag{2.12}$$

applying the curl to equation 2.11 and recalling

$$\nabla \times (\mathbf{u} \times \omega) = (\omega \cdot \nabla)\,\mathbf{u} - (\mathbf{u} \cdot \nabla)\,\omega$$

the vorticity equation is obtained

$$\frac{D\omega}{Dt} = (\omega \cdot \nabla)\,\mathbf{u} + \nu \nabla^2 \omega \tag{2.13}$$

in which the first term in the right hand side (rhs) is the vortex stretching.

Some extra comments on the vortex stretching phenomenon can lead to two important aspects of turbulent flows, like Reynolds stress distribution and a first introduction of the Kolmogorov scale.

In general, coherent structures need a shear to maintain their energy and the most energetic eddies are those that can absorb energy from the shear flow. These vortexes are those which can rotate faster. The experimental evidence of this process is given by the quadrant analysis, which links the higher values of Reynolds stress in zones where the vortex stretching is larger (ejection and sweep regions). Taking into account the following term in streamwise direction $x$

$$(\omega \cdot \nabla)\,\mathbf{u} \cdot x = \omega_x \frac{\partial u_x}{\partial x} + \omega_y \frac{\partial u_x}{\partial y} + \omega_z \frac{\partial u_x}{\partial z}. \tag{2.14}$$

The first term in the rhs describes the vortex stretching and considering valid the conservation of angular momentum, the rotational velocity will increase and consequently the vorticity will increase. This process is due to the velocity gradient in $x$-direction (figure 2.1 a). The latter two terms describe the rotation of the vortex in the remaining direction: this process is called vortex tilting. Furthermore, vortex tilting tends to align a vortex which has, for instance, only $\omega_z$ to the velocity gradient $d\bar{u}/dz$. After some time, this process will convert part of $\omega_z$ in a streamwise vorticity component, say $\omega_x$ (figure 2.1 (b)).

Taking into account Figure 2.1(a) having only $\omega_x \neq 0$ and applying the time derivation of the non-viscous term of equation 2.13, the follow equation is obtained

$$\frac{\partial \omega_x}{\partial t} = \alpha \omega_x \Rightarrow \omega_x(t) = \omega_x(0)\, e^{\alpha t} \tag{2.15}$$

which reveals an exponential increase. The $\alpha$ exponent is the eigenvalue of the correlated eigenvector $x$. Figure 2.1(a) suggests that there is a link between the diameter reduction of the tube and the vorticity increment, namely a scale reduction.

This scale reduction is infinite and theoretically can reach the molecular scales. Anyway, to respect the continuum hypothesis for which equation 2.15

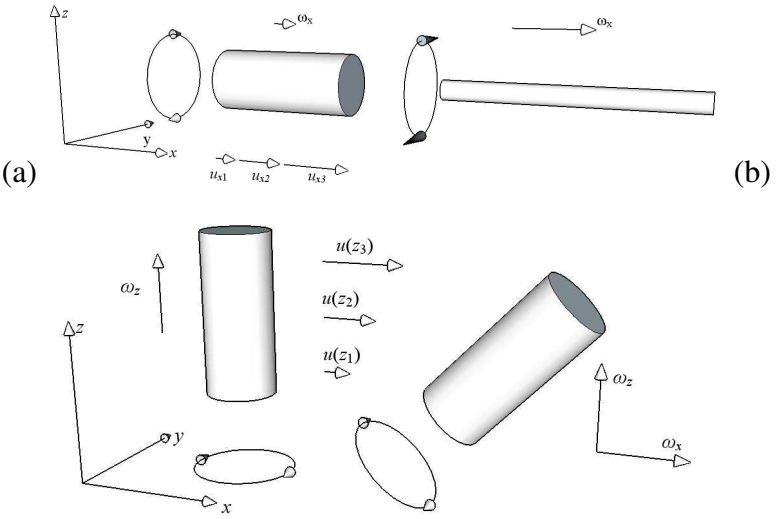


**Figure 2.1:** vortex stretching propagation; (a) pure $x$-direction stretching; (b) tilting stretching vortex

has been developed, the viscous term in equation 2.13 has to compensate the scale reduction.

This equilibrium is translated into a process in which the vorticity increment is balanced by the radial diffusion. It is a stationary process in *Burgers* vortex [54], in which the vortex radius is

$$r_B = \sqrt{\frac{\nu}{\omega'}}; \tag{2.16}$$

where $\omega'$ is the *rms* of the vorticity fluctuation, thus

$$\omega' = \sqrt{\frac{\varepsilon}{\nu}} \Rightarrow r_B = \left(\frac{\nu^3}{\varepsilon}\right)^{1/4} \tag{2.17}$$

which is defined as *Kolmogorov* scale.

### 2.2.3 Reynolds-Averaged Navier-Stokes (RANS) equation

Averaging the Navier-Stokes equations over the realization/time/space after application of Reynolds decomposition where a generic turbulent flow variable can be divided in a turbulence-averaged component and a fluctuating component [50]. Although several researchers have presented different forms of the Reynolds-Averaged Navier-Stokes (RANS) equations [113, 105], to the purpose of this section the time-averaged approach is considered. Hence, the Reynolds decomposition is the first stage to account the fluctuation of the variables due to turbulence . Taking into account a temporal series like a velocity signal, it can be divided into two components, a mean velocity $\bar{u}$ and a fluctuation $u'$, provided it is long enough to assert that the phenomenon can be considered ergodic. This idea was applied in hydraulics by Osborne Reynolds in 1883 [118] (see figure 2.2).

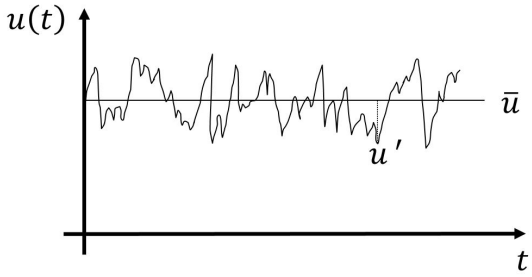


**Figure 2.2:** Reynolds variables decomposition

The instantaneous value of velocity $u(t)$ can be written as

$$u(t) = \bar{u} + u' \tag{2.18}$$

where $t$ is time. A statistical approach to turbulence is contained in this simple concept. An important issue in turbulence is conjugate variables (joint random variables). A simplest example of these are Cartesian components of velocity

in a generic velocity vector. Leaving aside the statistical analysis of a single variable, one can take into account the statistical behavior of two (or more) variables ($f$ and $g$) and try to extrapolate important information. Applying the mean, which is a linear operator, to another linear operator like sum, it is obtained $\overline{f+g} = \bar{f} + \bar{g}$; the mean of a constant multiplied to the variable is $\overline{af} = a\bar{f}$; the mean of the mean value is $\bar{\bar{f}} = \bar{f}$ and again the mean of an averaged variable multiplied to another variable is $\overline{\bar{f}\bar{g}} = \bar{f}\bar{g}$. As regards the derivative operator, the mean produces $\overline{\frac{\partial f}{\partial \mathbf{x}}} = \frac{\partial \bar{f}}{\partial \mathbf{x}}$, where $\mathbf{x} = (x_i, t)$ and $x_i$ is the direction ($x_1 = x$, $x_2 = y$, $x_3 = z$).

The previous statistical properties of the mean operator will be useful in the next sections, where a statistical approach of the theory of turbulence is presented. As highlighted in Davidson [29], any theory of turbulence has to be a statistical one. Taking into account a velocity signal registered in a set of controlled experiments, with identical conditions, identical statistical properties are shown even though the signals will appear different. This is true owing to the imperceptible variations of the boundary and initial conditions; these variations will be amplified in the velocity signal.

Owing to the fluctuating nature of the velocity and then of the motion of the fluid particles, a very high uncertainty is introduced in the following equations, justifying the use of a statistical approach.

The NS equation presents an extreme detail in terms of scales. Namely, the NS equations can solve the entire flow field from the biggest to the smallest scale motions; this detail requires a huge processing power to reach a solution in a reasonable time using a direct method of computational mathematics. Furthermore, the knowledge of the average value of the generic variable is enough for most engineering applications.

A variable-like velocity is therefore split into two components: its average value and the fluctuations around it, as specified in equation 2.18. In equation

2.18 the mean is defined as

$$\bar{\mathbf{u}} = \lim_{T\to+\infty} \frac{1}{T}\int_0^T \mathbf{u}(t)\,dt, \tag{2.19}$$

and the fluctuations

$$\mathbf{u}'(t) = \mathbf{u}(t) - \bar{\mathbf{u}}, \tag{2.20}$$

hereinafter, $\mathbf{u}(t) = \mathbf{u}$, $\mathbf{u'}(t) = \mathbf{u'}$.

Before exploring the RANS equations, it is useful to see the effect of the Reynolds decomposition on the following instantaneous continuity equation

$$\nabla\mathbf{u} = \nabla\left(\bar{\mathbf{u}} + \mathbf{u}'\right) = 0 \Rightarrow \nabla\bar{\mathbf{u}} = 0, \nabla\mathbf{u}' = 0. \tag{2.21}$$

where the latter relation is the instantaneous continuity equation.

Applying Reynolds decomposition to the NS equation

$$\frac{\partial\mathbf{u}}{\partial t} + \nabla\cdot(\mathbf{u}\mathbf{u}) = -\frac{1}{\rho}\nabla p + \nu\nabla^2\mathbf{u}, \tag{2.22}$$

in which

$$\frac{\partial\mathbf{u}}{\partial t} = \frac{\partial\bar{\mathbf{u}}}{\partial t} + \frac{\partial\mathbf{u}'}{\partial t},\ \ \nabla p = \nabla\bar{p} + \nabla p',\ \ \nabla^2\mathbf{u} = \nabla^2\bar{\mathbf{u}} + \nabla^2\mathbf{u}'. \tag{2.23}$$

the non-linear term in equation 2.22 is decomposed as follows

$$\nabla\cdot(\mathbf{u}\mathbf{u}) = \nabla\cdot\left[\left(\bar{\mathbf{u}} + \mathbf{u}'\right)\left(\bar{\mathbf{u}} + \mathbf{u}'\right)\right] = \nabla\cdot(\bar{\mathbf{u}}\bar{\mathbf{u}}) + \nabla\cdot\left(\bar{\mathbf{u}}\mathbf{u}'\right) + \nabla\cdot\left(\mathbf{u}'\bar{\mathbf{u}}\right) + \nabla\cdot\left(\mathbf{u}'\mathbf{u}'\right), \tag{2.24}$$

knowing that $\nabla\cdot\left(\overline{\bar{\mathbf{u}}\mathbf{u}'}\right) = \nabla\cdot\left(\overline{u'\bar{\mathbf{u}}}\right) \equiv 0$ is obtained

$$\frac{\partial\mathbf{u}'}{\partial t} + \nabla\cdot(\bar{\mathbf{u}}\bar{\mathbf{u}}) + \nabla\cdot\left(\overline{\mathbf{u}'\mathbf{u}'}\right) = -\frac{1}{\rho}\nabla\bar{p} + \nu\nabla^2\bar{\mathbf{u}}. \tag{2.25}$$

The non-zero second-order $\overline{\mathbf{u}'\mathbf{u}'}$ or higher statistical moments are a track of a turbulent flow. Davidson [29] highlights that $\overline{\mathbf{u}'\mathbf{u}'}$ is not a true stress, but it represents the mean momentum fluxes induced by turbulence. In other words, using the $\overline{\mathbf{u}'\mathbf{u}'}$ tensor the effect of turbulence on the stress can be captured.

Franca and Brocchini [50] states that in the instantaneous NS equation new terms related to the fluctuations, which appear in the momentum equation, introduce non-linearity. In particular, the term $\nabla \cdot \overline{\mathbf{u}'\mathbf{u}'}$ contains the indeterminacy of the RANS equations. Namely, the NS equation is formally a closed system, whereas the RANS equations are made up of 4 equations, which contain 13 unknown variables ($\mathbf{u}$, $p$ and the second-order tensor $\overline{\mathbf{u}'\mathbf{u}'}$). This indeterminacy is known in the literature as the *closure problem*.

Trying to solve it, one can get a new equation for fluctuations. Hence, subtracting equation 2.25 from equation 2.22

$$\frac{\partial \mathbf{u}'}{\partial t} + \nabla \cdot \left(\mathbf{u}'\mathbf{u}'\right) + \nabla \cdot \left(\bar{\mathbf{u}}\mathbf{u}'\right) + \nabla \cdot \left(\mathbf{u}'\bar{\mathbf{u}}\right) - \nabla \cdot \left(\overline{\mathbf{u}'\mathbf{u}'}\right) = -\frac{1}{\rho}\nabla \bar{p}' + \nu \nabla^2 \mathbf{u}', \tag{2.26}$$

which has to be multiplied by $\mathbf{u}'$; applying an averaging operator and summing it to its transpose equation, after some algebraic passages, it is obtained

$$\underbrace{\frac{\partial \overline{\mathbf{u}'\mathbf{u}'}}{\partial t}}_{1} + \underbrace{\bar{\mathbf{u}} \cdot \nabla \overline{\mathbf{u}'\mathbf{u}'}}_{2} + \underbrace{\overline{\mathbf{u}'\mathbf{u}'} \cdot \nabla \bar{\mathbf{u}}}_{3} + \underbrace{\left[\overline{\mathbf{u}'\mathbf{u}'} \cdot \nabla \bar{\mathbf{u}}\right]^T}_{4} + \underbrace{\nabla \cdot \overline{\mathbf{u}'\mathbf{u}'\mathbf{u}'}}_{5} =$$
$$\underbrace{-\frac{1}{\rho}\left[\overline{\mathbf{u}'\nabla p'} + \overline{\mathbf{u}'\nabla p'}^T\right]}_{6} + \underbrace{\nu\left[\overline{\mathbf{u}'\nabla^2\mathbf{u}'} + \overline{\mathbf{u}'\nabla^2\mathbf{u}'}^T\right]}_{7}. \tag{2.27}$$

The main point is that in equation 2.27 a triple correlations term arose ($\overline{\mathbf{u}'\mathbf{u}'\mathbf{u}'}$). A new equation can be found for the triple correlations term, using the same process, but a further fourth-order correlation term like $\overline{\mathbf{u}'\mathbf{u}'\mathbf{u}'\mathbf{u}'}$ is found

triggering a never-ending process. This procedure highlights the *closure problem of turbulence*.

Equation 2.27 can be still interpreted from the physical point of view, where terms 1 and 2 can be seen as a material derivative, whilst terms 3 and 4 represent the interaction between the Reynolds stress and the flow field. Terms 3 and 4 are equal to zero in the case of isotropic turbulence and, conversely, they set the production of the Reynolds stress in zones where a velocity gradient is present (like wall layer). Term 5 is the momentum transfer operated by the fluctuations $\mathbf{u}'$ in the relative Cartesian directions. Term 6 describes the interaction between pressure and velocity fields. The latter term 7 is the dissipation of turbulent fluctuation through the viscous effects.

## 2.3 Double-Averaged equations

In aerodynamics, like canopy flows, the spatially-averaging approach has been used since the 1970s [144, 117, 47, 48]. Recently, the Double-averaging Method (DAM) was also used in porous media hydrodynamics for describing high Reynolds number flows [4, 103, 33, 111, 66, 32] and in order to model flows between rough surfaces in sliding motion [116]. The DAM is obtained by applying the spatially-averaging approach to time-averaged variables. Double-average equations can be obtained applying the time-average to spatially-averaged variables [4, 33, 32]. Another way to obtain double-averaged equations was drawn by Wilson and Shaw [144], Raupach and Shaw [117], Finnigan [47], Giménez-Curto and Lera [58]. They took the RANS equations, which are already time-averaged, and applied the spatially-averaging. Nikora et al. [110] stated that this second way is physically more transparent and supported by several experimental campaigns differently from space-time averaging which is strong experimental supported.

Monin and Yaglom [99] defined the spatially-averaging operation as a convolution integral, which has the physical meaning of an average in the appropriate space or volume [47]. The use of volume is preferred, as it is easily measurable in tests. Considering a generic flow variable in time and space, Nikora et al. [107] defined the following equation

$$\langle\theta\rangle(x,y,z,t) = \frac{1}{V_f}\int_{V_f}\theta dV \tag{2.28}$$

$$\langle\theta\rangle_s(x,y,z,t) = \frac{1}{V_0}\int_{V_f}\theta dV \tag{2.29}$$

where $\theta$ is the flow variable in the space of the bed occupied by the fluid, the angle brackets denote the spatial average in the volume, $x$, $y$ and $z$ are the three Cartesian coordinates, $t$ is time, $V_f$ the volume occupied by fluid within a fixed region, $V_0$ the total volume and $\langle\theta\rangle_s = \phi_s\langle\theta\rangle$, where $\phi_s = V_f/V_0$ is the roughness geometry function or porosity in the case of permeable bed [107]. Slattery [129] defines the equation 2.28 as intrinsically spatially-averaged and the equation 2.29 as superficially spatially-averaged. In the following part of the text, the equations will be written only in the intrinsic spatially-averaged form, keeping in mind that they can be easily converted into superficially spatially-averaged form.

Two theorems are available to obtain the double-averaged variables in the rough-bed flow region [110]. The two following formulae have been derived from the transport theorem and the Gauss theorem, respectively

$$\left\langle\frac{\partial\theta}{\partial t}\right\rangle = \frac{1}{\phi_s}\frac{\partial\phi_s\langle\theta\rangle}{\partial t} + \frac{1}{V_f}\int\int_{S_{int}}\theta v\cdot ndS \tag{2.30}$$

$$\left\langle \frac{\partial \theta}{\partial x_i} \right\rangle = \frac{1}{\phi_s} \frac{\partial \phi_s \langle \theta \rangle}{\partial x_i} + \frac{1}{V_f} \int \int_{S_{int}} \theta n_i dS \tag{2.31}$$

where $S_{int}$ is the extension of the water-bed interface bounded by the averaging domain, $v$ the velocity in proximity to the bed-surface, $n$ the normal unit vector directed towards the bed surface, $x_i$ the $i^{th}$ direction (with $i$=1, 2, 3 for $x, y, z$, respectively) and $n_i$ the $i^{th}$ component of $n$; angle brackets again denote spatially-averaged instantaneous values.

In the case of a fixed bed, the bed-surface velocity is zero and in equation 2.30 the instantaneous variable is replaced with the time-averaged variable [110]. On the other hand, in mobile bed surfaces Nikora et al. [110] proposed the Gray and Lee [60] volume-averaged approach extended to time-space averaging as follows

$$\left\langle \phi_t \overline{\frac{\partial \theta}{\partial t}} \right\rangle = \frac{1}{\phi_s} \frac{\partial \phi_s \langle \bar{\theta} \rangle}{\partial t} + \frac{1}{V_f} \overline{\int \int_{S_{int}} \theta v \cdot n dS}^{S} \tag{2.32}$$

$$\left\langle \phi_t \overline{\frac{\partial \theta}{\partial x_i}} \right\rangle = \frac{1}{\phi_s} \frac{\partial \phi_s \langle \bar{\theta} \rangle}{\partial x_i} + \frac{1}{V_f} \overline{\int \int_{S_{int}} \theta n_i dS}^{S} \tag{2.33}$$

where $\phi_t = T_f / T_0$ is the time function (in analogy with the roughness geometry function), $T_0$ the total averaging time (e.g., in the case of solid particle movement this time includes the period in which the space point is occupied by solid particles), $T_f$ the averaging time interval (the period in which the space point is occupied by fluid only) and $\bar{\theta}^S = \phi_S \langle \theta \rangle$, where the overbar denotes time-averaged values. In the case of coarse gravel beds, the bed geometry is almost fixed or changes slowly over time. In this case, $T_0$ and $V_0$ can be considered as constants, with $\phi_t = 1$ and $v = 0$. Equations 2.32 and

2.33 are modified in the following way:

$$\left\langle \overline{\frac{\partial \theta}{\partial t}} \right\rangle = \frac{1}{\phi_s} \frac{\partial \phi_s \left\langle \bar{\theta} \right\rangle}{\partial t} \tag{2.34}$$

$$\left\langle \overline{\frac{\partial \theta}{\partial x_i}} \right\rangle = \frac{1}{\phi_s} \frac{\partial \phi_s \left\langle \bar{\theta} \right\rangle}{\partial x_i} + \frac{1}{V_f} \int \int_{S_{int}} \bar{\theta} n_i dS \tag{2.35}$$

Below, it is possible to see how the DAM acts on the equations of fluid dynamics and their terms. Moreover, the DAM can be applied to several analyses, in order to characterize the behavior of a rough-bed flow.

### 2.3.1 DAM equations

Hereinafter, the Einstein notation (or Einstein summation convention) will be adopted. Properties resulting from the DAM have been previously introduced. In fact, procedures available in time-averaging are also applicable to space-averaged variables, operating a decomposition of the variables with respect to time and space.

According to the previous section, a generic fluid dynamics equation can be derived in both time-space and space-time, obtaining the same result in both cases [111]. Square brackets and straight overbar denote spatial and temporal averages, respectively, whereas deviations from the spatial and temporal average are identified by tilde overbar and prime, respectively.

Pedras and de Lemos [111] identified the primary time decomposition as $u_i = \bar{u}_i + u_i'$, where $u_i$ is the instantaneous velocity, as before the overbar denotes the time-averaged velocity ($\bar{u}$) and the related velocity fluctuation $u_i'$; the subscript $i$ indicates the velocity component in the $i^{th}$ direction. The primary space decomposition is $u_i = \langle u_i \rangle + \hat{u}_i$, where $\langle u_i \rangle$ is the space-averaged

velocity in the $x_i$ direction and $\hat{u}_i$ is the spatial fluctuation of velocity. In addition, it is possible to perform a second decomposition in time-space: $u_i' = \langle u_i' \rangle + u_i''$,$\hat{u}_i = \tilde{u}_i + u_i''$, or in space-time: $\langle u_i \rangle = \langle u_i \rangle + \langle u_i \rangle'$, $\hat{u}_i = \tilde{u}_i + u_i''$. Using the property for which the spatial average of the $u$-fluctuation is equal to the fluctuation of the spatial average of $u$, the following relationship is obtained [114]

$$u_i = \langle \bar{u}_i \rangle + \tilde{u}_i + \langle u_i' \rangle + u_i'' \tag{2.36}$$

where $\langle \bar{u}_i \rangle$ is the double-averaged velocity in the $x_i$ direction, $\tilde{u}_i$ the spatial fluctuation of time-averaged velocity, $\langle u_i' \rangle$ the spatially-averaged velocity fluctuation and $u_i''$ the spatial variation in the velocity fluctuation.

### 2.3.2 Stress term decomposition

As is well-known, the DAM produces additional terms in the NS equation, as a combination of velocity components averaged in time and space [107]. The non-viscous fluid stress can be expressed as follows

$$\left\langle \overline{u_i u_j} \right\rangle = \left\langle \bar{u}_i \right\rangle \left\langle \bar{u}_j \right\rangle + \left\langle \tilde{u}_i \tilde{u}_j \right\rangle + \left\langle \overline{u_i' u_j'} \right\rangle \tag{2.37}$$

with $j$ =1, 2, 3; using the space-time averaged properties of the variables shown previously, one can obtain

$$\left\langle \overline{u_i u_j} \right\rangle = \overline{\langle u_i \rangle} \overline{\langle u_j \rangle} + \overline{\langle u_i \rangle' \langle u_j \rangle'} + \left\langle \hat{u}_i \hat{u}_j \right\rangle \tag{2.38}$$

In the case of fixed bed or slowly changing bed topography, commutative properties can be used: $\overline{\langle u_i \rangle} = \langle \bar{u}_i \rangle$ and $\overline{\langle u_i \rangle' \langle u_j \rangle'} = \langle u_i' \rangle \left\langle u_j' \right\rangle$. Using equations 2.37 and 2.38, Nikora et al. [110] and Pokrajac et al. [114] highlighted how time/space and space/time averaging and decomposition approaches lead

to the same result

$$\left\langle \tilde{u}_i \tilde{u}'_j \right\rangle + \left\langle \overline{u'_i u'_j} \right\rangle = \overline{\left\langle u'_i \right\rangle \left\langle u'_j \right\rangle} + \overline{\left\langle \hat{u}_i \hat{u}_j \right\rangle} \tag{2.39}$$

where in the left hand side (lhs) there is a sum of form-induced (or dispersive) stresses $\left\langle \tilde{u}_i \tilde{u}_j \right\rangle$ and space-averaged Reynolds stresses $\left\langle \overline{u'_i u'_j} \right\rangle$, whereas in the rhs there are large scale contributions of the Reynolds stresses $\overline{\left\langle u'_i \right\rangle \left\langle u'_j \right\rangle}$ and the time-averaged correlations of spatial fluctuations $\overline{\left\langle \hat{u}_i \hat{u}_j \right\rangle}$.

### 2.3.3 Double-Averaged continuity equation

The double-averaged continuity equation is

$$\left\langle \overline{\frac{\partial \rho}{\partial t} + \frac{\partial \rho u_i}{\partial x_i}}^{S} \right\rangle_S = \rho \frac{\partial \phi_s}{\partial t} + \rho \frac{\partial \phi_s \left\langle \bar{u}_i \right\rangle}{\partial x_i} = 0 \tag{2.40}$$

where $\rho$ is the fluid density, which is constant for an incompressible fluid ($\partial \rho / \partial t = 0$) and $u_i$ is the $i^{th}$ component of the velocity vector.

### 2.3.4 Double-Averaged Navier-Stokes (DANS) equations

A double-averaged version of the Navier-Stokes equations is found in Nikora [104]. Equations 2.41 were derived from the Navier-Stokes equation by applying double-averaging theorems 2.34 and 2.35 to each term of the RANS equation 2.27; in addition, instantaneous velocity decomposition shown in

equation 2.36 and stress-term decomposition in equation 2.39 were used.

$$\underbrace{\frac{\partial \langle \bar{u}_i \rangle}{\partial t}}_{1} + \underbrace{\langle \bar{u}_j \rangle \frac{\partial \langle \bar{u}_i \rangle}{\partial x_j}}_{2} = \underbrace{g_i}_{3} - \underbrace{\frac{1}{\rho \phi_s} \frac{\partial \phi_s \langle \bar{p} \rangle}{\partial x_i}}_{4} - \underbrace{\frac{1}{\phi_s} \frac{\partial \phi_s \langle \tilde{u}_i \tilde{u}_j \rangle}{\partial x_i}}_{5} - \underbrace{\frac{1}{\phi_s} \frac{\partial \phi_s \left\langle \overline{u_i' u_j'} \right\rangle}{\partial x_j}}_{6}$$
$$+ \underbrace{\frac{1}{\phi_s} \frac{\partial}{\partial x_j} \phi_s \left\langle \overline{\nu \frac{\partial u_i}{\partial x_j}} \right\rangle}_{7} + \underbrace{\frac{1}{\rho \langle \phi_t \rangle V_f} \overline{\int\int_{S_{int}} p n_i ds}^{S}}_{8} - \underbrace{\frac{1}{\langle \phi_t \rangle V_f} \overline{\int\int_{S_{int}} \nu \frac{\partial u_i}{\partial x_j} n_j ds}^{S}}_{9}. \tag{2.41}$$

The first and second terms of equation 2.41 are the local (or temporal) acceleration and the convective acceleration, respectively; the third term is gravity (not subjected to the DAM, inasmuch the gravity field is constant); the fourth term is the pressure gradient; the fifth term is the form-induced (or dispersive) term; the sixth term is the space-averaged Reynolds stress; the seventh term is the DA viscous fluid stress; the eighth and ninth terms represent the DA pressure and viscous drag terms, respectively.

### 2.3.5 Double-Averaged shear stress

The DAM decomposition has implications on the shear stress definition as well as in equation 2.41, where the sum of the fifth, sixth and seventh terms can be enclosed in the total double-averaged shear stress in the streamwise direction [57, 110, 90], as follows

$$\langle \bar{\tau} \rangle = -\rho \langle \tilde{u}_i \tilde{u}_j \rangle - \rho \langle u_i' u_j' \rangle + \rho \nu \frac{\partial u_i}{\partial x_j} \tag{2.42}$$

where the first, second and third term of equation 2.42 are the corresponding stress terms seen in equation 2.41. In fact, in the roughness layer a new term

(form-induced term) arose to take into account the effects of the "form" of the bed composed of a statistically chaotic distribution of roughness elements. Manes et al. [90] observed how the Double-Averaged Reynolds Shear Stress (DARSS) $-\rho\left\langle u_i' u_j' \right\rangle$ along the vertical axis is dominant in the outer layer and in the logarithmic layer (if applicable), where it reaches its maximum value before decreasing. In the near bed region, where the flow is influenced by individual roughness elements, the DARSS decrement is compensated in the roughness layer by the Form-Induced Shear Stress (FISS) $-\rho\left\langle \tilde{u}_i \tilde{u}_j \right\rangle$ and down to the roughness, very close to the solid surface, the Viscous Shear Stress (VSS) $\rho\nu\frac{\partial u_i}{\partial x_j}$. The same trends were found by Dey and Das [40], who compared data sets by Nikora et al. [107], Mignot et al. [98], Sarkar and Dey [123]: in these papers a damping was observed in the DARSS profile in correspondence to the roughness layer, owing to a turbulence reduction partially compensated by FISS and VSS. This particular behavior of the FISS profile is useful also to delimit the form-induced sublayer in a thickness interested by a non-negligible FISS value. In addition, Dey and Das [40], comparing the aforementioned datasets, related the magnitude of the FISS increase with the bed roughness increase through a greater velocity fluctuation $\left\langle \tilde{u}_i \tilde{u}_j \right\rangle$. This finding confirmed the results by Aberle et al. [2], who asserted that the FISS vertical distribution is governed only by bed roughness characteristics.

The bed roughness characteristics introduce not only "form-induced" stress but also further complexity by adding locally induced scales to the flow. In a simplistic way, the last sentence introduces a much more complex issue as the scales in a turbulent flow.

## 2.4 Mean velocity distribution

Nezu and Nakagawa [101] proposed to classify a flow over a smooth walls in layers. In particular, the flow is divided into two distinct flow layers of a two-dimensional turbulent open-channel stream, namely the inner layer, which is composed of a viscous sublayer and the buffer region, and the outer layer, which is formed by the intermediate region and the free surface region. Despite the smooth wall, which contains two typical scales (the viscous length scale in the inner layer and the boundary layer thickness in the outer layer), the presence of roughness at the wall introduces a new relevant length scale, which is the characteristic roughness height, $k_s$. Through the roughness length scale a new dimensionless group can be computed, the roughness Reynolds number, $Re_{k_s} = u_* k_s / \nu$. This parameter can be of help to classify the flow in terms of force:

- $Re_{k_s} < 5$ suggest an important influence of the viscous force with respect over the inertial one, the viscous sublayer is higher than the roughness dimension and the flow is classified as hydrodynamically smooth;
- $5 < Re_{k_s} < 70$ although the inertial forces prevails on the viscous ones, the effect of the second is still important and the viscous sublayer is of the order of the roughness dimension. The flow is called transitionally rough;
- $Re_{k_s} > 70$ in this case the inertial forces are bigger than the viscous ones; this condition reduces the viscous sublayer uncovering roughness elements. The flow regime is called fully rough.

To account for a very high bed roughness, Nikora et al. [107] introduced the roughness effects and bed permeability in a new subdivision of the flow

in an open-channel into five layer. The outer layer and the overlap layer are identical to the those of the classification proposed by Nezu and Nakagawa [101]; the form-induced sublayer is the layer where the effects of roughness elements on the above flow are tangible; the interfacial sublayer is located within the roughness elements themselves; finally, the last two layers belong to the roughness layer.

Since the origin of the vertical coordinate is placed at the roughness crests, $z_c = 0$; $h_w$ and $h_t$ are the water depths measured above the maximum grain crest level and the minimum trough level, respectively. From these statements the relative submergence, which is given by the ratio of the flow depth to the roughness height, is $\Delta = h_w/\Delta_R$, $\Delta_R$ being the roughness height. According to Nikora et al. [107], the flow in OCFs can be classified according to the following flow types:

1. high relative submergence; all flow layers are present;

2. intermediate submergence; the roughness layer and the outer layer are present whereas the overlap layer, where the velocity distribution is logarithmic, is questionable;

3. low submergence; the roughness layer extends across the entire flow depth;

4. the roughness elements protrude through the free surface, the interfacial sublayer covers the entire water column.

It can be anticipated that the experiments in this thesis are carried out in flow type 2.

### 2.4.1 Logarithmic layer

The distribution of mean streamwise velocity is described through the universal logarithmic law, above the rough-bed, thanks to equation 2.43.

$$\frac{\langle \bar{u} \rangle}{u_*} = \frac{1}{\kappa} ln \left( \frac{z+d}{\Delta_R} \right) + B \tag{2.43}$$

where $\kappa$ is the well-known von Kármán constant ($= 0.41$), $d$ the zero-plane displacement and $B$ the wall constant. The use of the logarithm law is subordinated to the presence of a region where the only relevant length scale is the distance from the wall ($z$).

In contrast to the indication of Jiménez and del Alamo [71], who placed 40 as the lower limit of relative submergence to obtain an overlap region, the logarithmic law is often applied to intermediate relative submergence flows. This forced application produced a point of disagreement on the universality of $\kappa$ value. Values of $\kappa$ contained between 0.41 and 1.6 were found by Bayazit [12] in a flow having $1 < \Delta < 4$. Koll 2006 proposed $\kappa$ as a function of $\Delta$ for low relative submergence flows and found a minimum value of 0.18 for $4 < \Delta < 7$. In these studies problems related to the accuracy of the measurements and overfitting issues can conduce to misinterpretation of results.

Townsend [135] states that within the overlap layer the TKE production and dissipation are commonly assumed to be in equilibrium. Nikora and Goring [106] supposed that TKE production and dissipation are in equilibrium in flow regions where TKE flux is nearly constant. This most rigorous approach can be used to have a direct measurement of the overlap layer at intermediate relative submergences.

### 2.4.2 Outer layer

Out of upper edge of the overlap layer a deviations of the velocity profile from the log law is observed. to account this deviation a further and empirical function is added $W(z/h)$

$$\frac{\langle \bar{u} \rangle}{u_*} = \frac{1}{\kappa} ln \left( \frac{z+d}{\Delta_R} \right) + B + W(z/h) \tag{2.44}$$

and

$$W(z/h) = \frac{2\Pi}{\kappa} \sin^2 \left( \frac{\pi}{2} \frac{z}{h} \right) \tag{2.45}$$

where $\Pi$ is the wake strength parameter. The defect law, proposed by Coles [24], was expressed in the form of equation 2.45 by Hinze [64] and confirmed for OCFs in Nezu and Nakagawa [101].

### 2.4.3 Interfacial sublayer

The nearness to the bed of this region does not allow a model to be found to describe the velocity distribution. Possible velocity distributions were investigated by Nikora et al. [108], who proposed three velocity distributions: constant, linear and exponential, respectively. To the purpose of this work, this region is not further considered.

## 2.5 Scales in river flow

A wide range of scales is present in river dynamics. Temporal scales cover time from centuries to micro-seconds and the corresponding spatial scales contain distance from kilometers to micro-meters [50]. In a simplistic way, one may say that matter in the fluid is often subjected to two main kinds of random movements: one on the molecular scale, the thermal agitation

of molecules, and one on a macroscopic scale, turbulence [28].The main differences between molecular agitation and turbulent motions are the scales involved (i.e. a typical turbulent motion, say a 'sweep', is ordinarily very large, compared to one molecular free path).

The larger scales are the most important for engineering work, which is related to the interaction between water and structures, covering space scales from kilometers to centimeters and time-scales from years to seconds. One can just think about the erosion and sediment transport issue, bridge sour problem or flood protection to have an idea of the large-scale range which engineers are interested in. Events like sweep or burst are large-scale turbulent expressions and their statistical occurrence also contributes to the formation of an undular sediment bed, which in turn produces a flow separation and an eddy system, which can influence the main flow even up to the free surface. This process triggers a continuous interaction between bed and flow [44]. In the next sections it will be clarified that every scale is characterized by an energy level and how it is transferred to the near scales. An energy distribution model across the scales is given in Figure 2.3 [50].

To talk about scales in a non-arbitrary way, some mathematical concepts should be introduced. In this regard, as said in previous chapters, statistical concepts are needed.

### 2.5.1 Stochastic processes

Turbulent occurrence can be seen from a stochastic point of view. Namely, two random time variables $x(t)$ and $y(t)$ can be defined from their expected

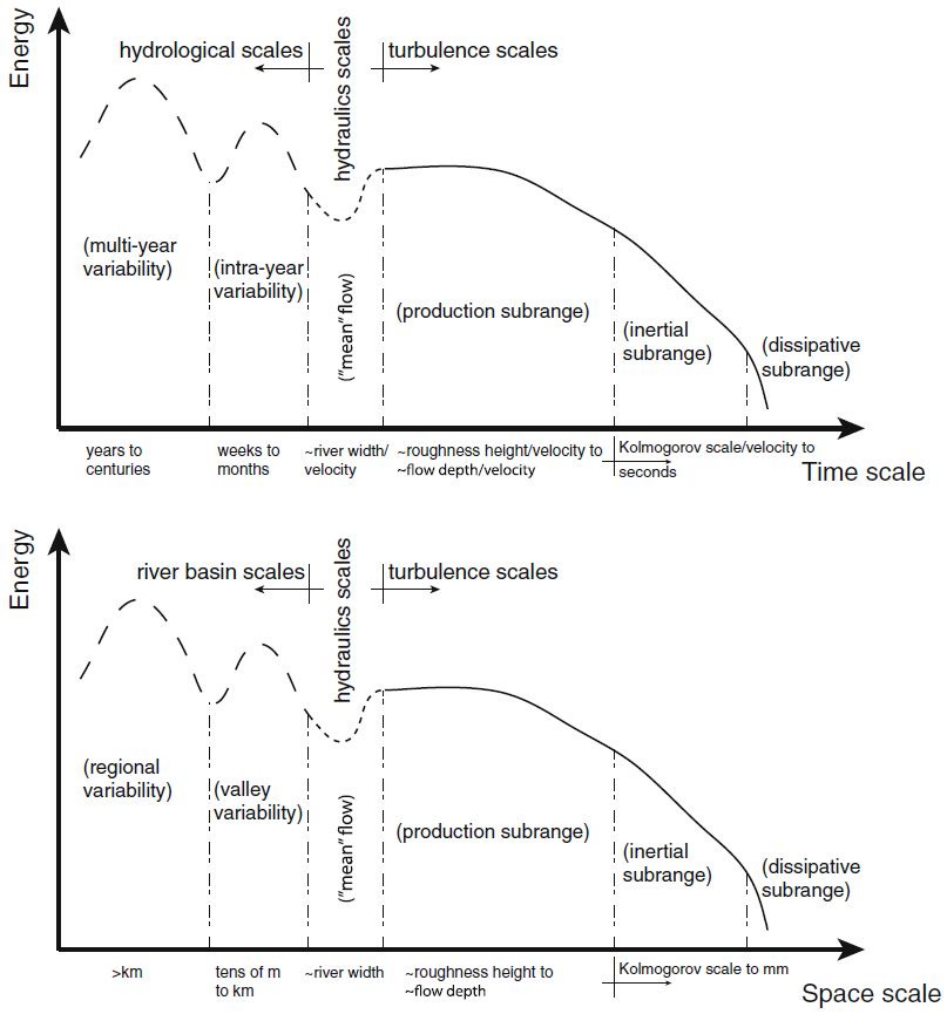


**Figure 2.3:** Distribution of flow energy with time and spatial scales in river taken from Franca and Brocchini [50].

value

$$\mu_X(t) = \mathbb{E}[x(t)]$$
$$\mu_Y(t) = \mathbb{E}[y(t)]\,. \tag{2.46}$$

Considering two instants $t_1 = t, t_2 = t + \mathfrak{T}$, where $\mathfrak{T}$ is the time-lag, *Covariance function* can be defined as

$$\begin{aligned} C_{xx}(t, t+\mathfrak{T}) &= \mathbb{E}\left[(x(t) - \mu_X(t)) \cdot (x(t+\mathfrak{T}) - \mu_X(t+\mathfrak{T}))\right] \\ C_{yy}(t, t+\mathfrak{T}) &= \mathbb{E}\left[(y(t) - \mu_Y(t)) \cdot (y(t+\mathfrak{T}) - \mu_Y(t+\mathfrak{T}))\right] \\ C_{xy}(t, t+\mathfrak{T}) &= \mathbb{E}\left[(x(t) - \mu_X(t)) \cdot (y(t+\mathfrak{T}) - \mu_Y(t+\mathfrak{T}))\right] \end{aligned} \tag{2.47}$$

Equation 2.47 suggests that $C_{xy} \neq C_{yx}$, unless when $\mathfrak{T} = 0$; in that case, $C_{xy} = C_{yx}$; $C_{xx}$ and $C_{yy}$ are the variance of $x$ and $y$ respectively.

Assuming a Gaussian process, the equations are functions only of the time-lag $\mathfrak{T}$ (stationary process) and the *auto-covariance function* can be defined as

$$\begin{aligned} C_{xx}(\mathfrak{T}) &= \mathbb{E}\left[(x(t) - \mu_X) \cdot (x(t+\mathfrak{T}) - \mu_X)\right]; \\ C_{yy}(\mathfrak{T}) &= \mathbb{E}\left[(y(t) - \mu_Y) \cdot (y(t+\mathfrak{T}) - \mu_Y)\right]; \end{aligned} \tag{2.48}$$

whereas, the cross-covariance function is

$$C_{xy}(\mathfrak{T}) = \mathbb{E}\left[(x(t) - \mu_X) \cdot (y(t+\mathfrak{T}) - \mu_Y)\right]; \tag{2.49}$$

Developing the polynomial in 2.48 and 2.49

$$\begin{aligned} R_{xx}(\mathfrak{T}) &= \mathbb{E}\left[x(t) \cdot x(t+\mathfrak{T})\right]; \\ R_{yy}(\mathfrak{T}) &= \mathbb{E}\left[y(t) \cdot y(t+\mathfrak{T})\right]; \end{aligned} \tag{2.50}$$

and

$$R_{xy}(\mathfrak{T}) = \mathbb{E}\left[x(t) \cdot y(t+\mathfrak{T})\right]. \tag{2.51}$$

where $R_{xx}$ and $R_{yy}$ are the auto-correlation function whereas $R_{xy}$ is the cross-correlation function. Finally,

$$\begin{aligned} C_{xx}(\mathfrak{T}) &= R_{xx}(\mathfrak{T}) - \mu_X^2; \\ C_{yy}(\mathfrak{T}) &= R_{yy}(\mathfrak{T}) - \mu_Y^2; \\ C_{xy}(\mathfrak{T}) &= R_{xy}(\mathfrak{T}) - \mu_X \mu_Y. \end{aligned} \tag{2.52}$$

Hence, it is possible to assert that the covariance function is the second order moment computed with respect to the time-lag [8]. The auto-correlation and cross-correlation functions are the basis for the turbulence analysis conducted through the Fourier Transform (FT).

It can be useful to introduce the Schwartz inequality [125] for stationary processes

$$\left|R_{xy}(\mathfrak{T})\right|^2 \leq R_{xx}(0) \cdot R_{yy}(0). \tag{2.53}$$

Equation 2.53 suggests that any $\mathfrak{T}$ considered, the cross-correlation function square must be at least equal to the product of the auto-correlation functions (also called one-point correlation).

At this stage, taking into account a generic variable as the velocity fluctuations in a river, i.e. $u'$ and $w'$ which are the fluctuations in streamwise and vertical direction, respectively, equation 2.53 at $\mathfrak{T} = 0$ assumes the meaning of the Reynolds stress $R_{xz}(0) = \overline{u'w'}$, confirming the link between the correlation function and the second-order moments. In fact, using the same process one can find all the components of the Reynolds stresses $u'u'$, $v'v'$ and $w'w'$ from the auto-correlation function and $u'v'$, $v'w'$ and $u'w'$ from the cross-correlation function.

In Figure 2.4 a typical behavior of the dimensionless correlation function versus lag-time is shown. The lag-time increment generates an exponential

decrease in the correlation function. This trend becomes unstable at the lag-time for which no more correlation is observed.

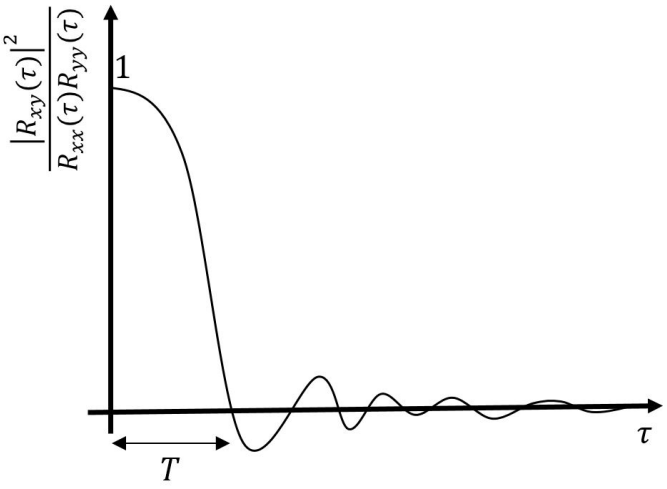


**Figure 2.4:** Time correlation of two variables

Still considering a fluid particle subjected to velocity fluctuations, the trend shown in figure 2.4 suggests a "memory" of the fluid particle motion in the elapsed time $T$, whereas for a lag-time greater then $T$ such memory is deleted and there is no correlation through the velocity fluctuations.

Alternatively, the correlation can be seen as a function of space ($r$). Namely, considering a vortex and two points belonging to the same coherent structure, varying the distance $r$ between the points the correlation function assumes the shape shown in figure 2.5.

The use of the time-correlation function or the space-correlation function is connected, in experimental field, to the instrument. Namely, two-points measurements can exploit the space-correlation function, whereas single-point measurements requires time-correlation function. However, space and time are linked by the relation $T = r/\bar{u}$.

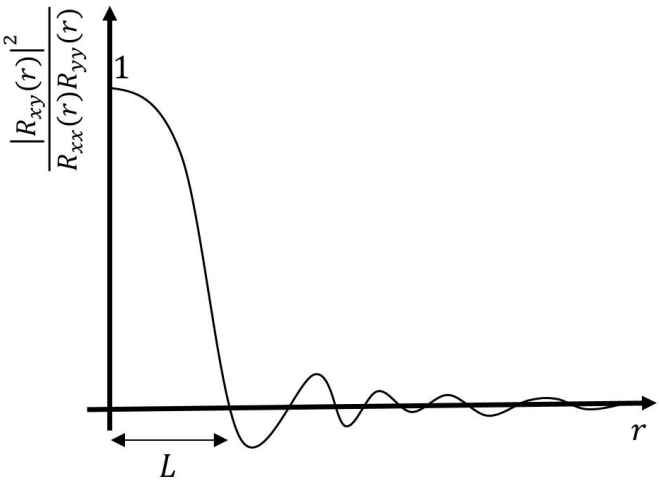


**Figure 2.5:** Space correlation time of two variables

Unfortunately, the relation $T = r/\bar{u}$ presents some limitations, in order to be applied to the measurements. In fact, measuring the instantaneous velocity by using a sensor at one location (single-point measurement) for a period of time one can observe the vortex drift through the sensor. These eddies could change size and shape as they drift by, making the measurement unclear and difficult to interpret. This problem was solved by Taylor [133], thanks to the *Taylor frozen-in hypothesis* (simply called the Taylor hypothesis).

### 2.5.2 Taylor frozen-in hypothesis

Just figure that a sensor measures the instantaneous flow velocity in a location. In Figure 2.6 the passage of a vortex through the measurement point is observable. The Taylor hypothesis asserts that, in order to use the measurement for instance in the FT analysis, the stream velocity should be much greater than the variance of the velocity fluctuations ($\langle\bar{\sigma}_u\rangle = \left\langle\sqrt{\overline{u'u'}}\right\rangle$), which cause the vortex distortion.

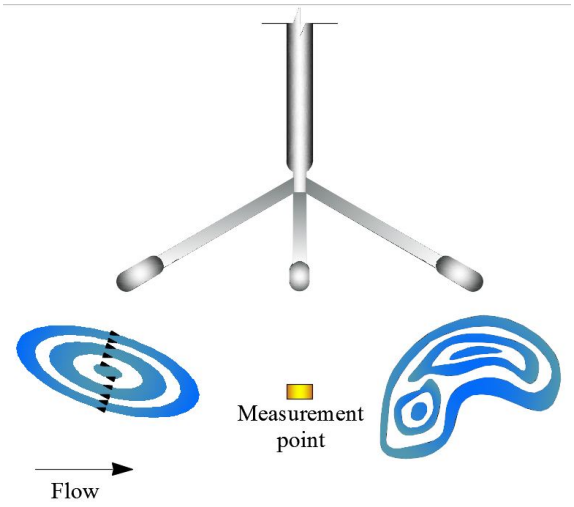


**Figure 2.6:** Distortion process of a vortex which drift in a measurement point

The condition $\bar{u} \gg \langle \bar{\sigma}_u \rangle$ is what is called *Taylor frozen-in hypothesis*. Moreover, when the aforementioned quantities are measured in a turbulent flow it is challenging to link the temporal fluctuations with the spatial ones. Furthermore, the main approximation in experimental turbulence studies is the switching between frequency and wavenumbers. The frozen-in hypothesis, proposed by Taylor [133], assumes that the flow field pushes the vortex through the sensor measurement point in a quasi-frozen manner. Namely, the velocity fluctuations evolve slowly, compared to the mean velocity, and the vortex does not stretch nor distort during the measurement. This assumption naturally restricts its application to low turbulence intensities, namely when the variance of the velocity fluctuations is much smaller than the characteristic mean flow.

The Taylor hypothesis can be easily respected in systems characterized by fast fluids, such as in the case of solar wind as well as atmospheric flows far from the boundary surface, contrariwise this hypothesis becomes difficult to satisfy in bounded flows, especially near the wall. The Taylor hypothesis

in OCFs is a delicate issue, which requires more and more attention, as highlighted in Del Alamo and Jiménez [35] and Smits et al. [130].

### 2.5.3 Taylor microscale

The analytic behavior of the dimensionless correlation function is such that it is equal to the unity in the origin, implying that its first derivative reveals a maximum at $r = 0$ and the second derivative is always negative at $r \approx 0$. The correlation function shape, hypothesized by Taylor [132], is described by equation 2.54.

$$\lim_{\delta r \to 0} \overline{\left| \frac{u(r+\delta r) - u(r)}{\delta r} - \frac{du(r)}{dr} \right|^2} = 0. \tag{2.54}$$

where $u(r)$ is a velocity component, which is function of the distance increment $r$ and $\delta r$ is the space increment. This limit describes the obscuring parabolic curve of the correlation function (see Figure 2.7).

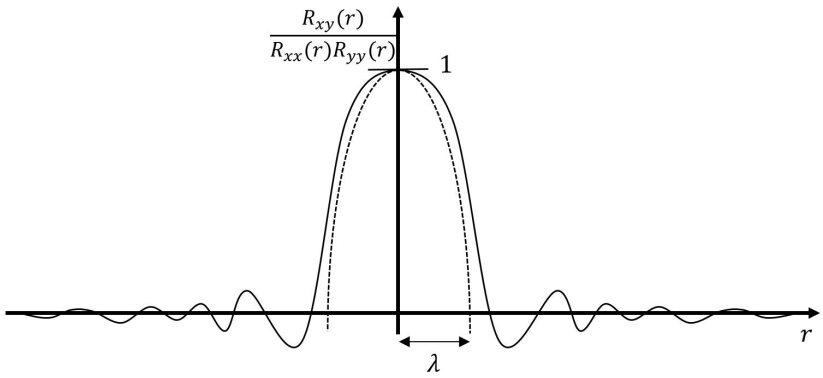


**Figure 2.7:** Graphic interpretation of Taylor microscale, the solid lines represent the correlation function versus a distant $r$ and the dashed line is the obscuring parable that defines the Taylor microscale to the intersection with $r$ axes.

The Taylor microscale is defined as the intersection between the zero axes of correlation function and the mentioned obscuring parabolic curve. According to Taylor [132]

$$2\frac{\overline{u'^2}}{\lambda^2} = -\overline{\left(\frac{du(r)}{dr}\right)^2}. \tag{2.55}$$

where $\lambda$ is called Taylor microscale. Assuming valid the isotropy condition, the energy dissipation rate $\varepsilon$ is defined by

$$\varepsilon = 15\nu\overline{\left(\frac{du(r)}{dr}\right)^2}; \tag{2.56}$$

From equation 2.55 and 2.56, the Taylor microscale is obtained as

$$\lambda = \sqrt{15\nu\frac{\overline{u'^2}}{\varepsilon}}. \tag{2.57}$$

Using equation 2.57, it is possible to link the Taylor microscale to the Reynolds number $Re_R = uR/\nu$ (related to the largest eddies $R \propto K^{3/2}/\varepsilon$) as follows

$$\lambda = \sqrt{\frac{10R}{Re_R}}. \tag{2.58}$$

This microscale has an historical importance, since it was replaced by the more well-known Kolmogorov microscale.

### 2.5.4 Kolmogorov hypothesis

To introduce the Kolmogorov hypothesis, a qualitatively analysis of the turbulence behavior with respect the main flow should be done. It is possible to analyze how the energy of the large scale (LS) moves towards to the small scale (SS), in particular from the large eddies, which take energy from

the main flow and yield energy to the smaller eddies, which have universal behavior in the universal subrange. In particular, the LS having a length scale $L$ and a velocity scale $\bar{u}$ does not influence the SS, which has a length scale $l$ and a velocity scale $u'$. This involves a net scale separation and a statistical independence between LSs and the isotropic SS structures. The isotropic term implies that $\overline{u_1'u_1'} = \overline{u_2'u_2'} = \overline{u_3'u_3'}$. Nevertheless, the mean flow acts on the SSs indirectly. In fact, the energy flux through the LSs (which depends on *Re*) towards the SSs should be balanced by the dissipation rate per mass unit ($\varepsilon$). Namely, large *Re* numbers produce large $\varepsilon$, in order to have equilibrium; then, the exchange between LSs and SSs should be a function of *Re* [8].

Briefly, $\varepsilon$ can be defined through the velocity components

$$\varepsilon = \frac{1}{2}\nu \sum_{i,j} \overline{\left(\frac{\partial u_i}{\partial x_j} + \frac{\partial u_j}{\partial x_i}\right)}. \tag{2.59}$$

In turbulent flow, in which the viscosity effects are negligible, one can obtain

$$\varepsilon = \frac{1}{2}\nu \sum_{i,j} \overline{\left(\frac{\partial u_i'}{\partial x_j} + \frac{\partial u_j'}{\partial x_i}\right)}. \tag{2.60}$$

Equation 2.60 suggests how the SSs are statistically independent of the mean flow; therefore, the SSs are universal in each flow having the same *Re* number. The SS hypothesis of isotropic condition is also known as the *Kolmogorov first hypothesis*.

### Kolmogorov first hypothesis - Kolmogorov microscale

The first similarity hypothesis asserts that the SS motions (at scales much larger than $\eta$) are statistically isotropic and the distribution of the velocity difference $[u(x+r,t) - u(x,t)]$ between two points in space is determined by

the local length scale $\eta = |r|$, the kinematic viscosity $\nu$ and the mean energy dissipation rate per mass unit $\varepsilon$ [143]. Applying the Vaschy-Buckingham theorem, a definition for the length scale $\eta$, the velocity scale $u_\eta$ and the temporal scale $\tau_\eta$ is found

$$\eta \equiv \left(\frac{\nu^3}{\varepsilon}\right)^{1/4};\ u_\eta \equiv (\nu\varepsilon)^{1/4};\ \tau_\eta \equiv \left(\frac{\nu}{\eta}\right)^{1/2}; \tag{2.61}$$

where $\eta$ is known as the Kolmogorov microscale, which is the threshold under which the viscous force is converted into heat by the dissipation process. The small-vortex Reynolds number can be obtained as follows

$$Re_\eta = \frac{u_\eta \eta}{\nu} = \frac{(\varepsilon\nu)^{1/4}\left(\nu^3/\varepsilon\right)^{1/4}}{\nu} = 1. \tag{2.62}$$

In addition, $Re_\eta$ is a marker related to the edge between the inertial subrange and the dissipation range. Dey [39] asserts that $Re_\eta < 1$ indicates a dissipation process, whereas $Re_\eta > 1$ identifies an energy transfer process. It can be useful to establish the relation between the Kolmogorov scale $\eta$ and the LSs, taking into account the definition $\varepsilon \sim u^3/L$

$$\begin{aligned} \frac{\eta}{L} = \left(\frac{\nu^3}{\varepsilon}\right)^{1/4}\frac{1}{L} \approx \left(\frac{\nu^3}{u^3L^3}\right)^{1/4} &= Re^{-3/4}; \\ \frac{u_\eta}{u} &\approx Re^{-1/4}; \\ \frac{\tau_\eta}{\tau_L} &\approx Re^{-1/2}. \end{aligned} \tag{2.63}$$

Its wording means that an increasing of the Reynolds number produces a decrease in the Kolmogorov scale number. Hence, is possible to anticipate that a net separation of scales between $L$ and $\eta$ occurs at high $Re$ numbers.

The last sentence introduces the need to have a net separation of scales and then a criterion to set experiments.

#### Kolmogorov second hypothesis - scales separation

The Kolmogorov second hypothesis speculates the existence of a range where there are no effects of viscosity; moreover, this range occurs at scales smaller than the energy containing scales. This range is called *inertial subrange*; it is delegated to pure energy transfer, where no generation nor dissipation are present; this process is called *Energy Cascade*.

In the inertial subrange the main parameter is the energy dissipation rate $\varepsilon$, which is the vector between the production range and the dissipation range. Exploiting the dimensional analysis $\varepsilon$ can be defined as

$$\varepsilon = \frac{u_\eta^3}{\eta} \Longrightarrow u(l) = u_\eta \left(\frac{l}{\eta}\right)^{1/3} \sim u_T \left(\frac{l}{L}\right)^{1/3}; \tag{2.64}$$

$$\varepsilon = \frac{\eta^2}{\tau_\eta^3} \Longrightarrow \tau(l) = \tau_\eta \left(\frac{l}{\eta}\right)^{2/3} \sim \tau_T \left(\frac{l}{L}\right)^{2/3}; \tag{2.65}$$

where $L$ represents the LS dimension and $\varepsilon$ corresponds to the vortex in the inertial subrange of size $l$.

Once the inertial subrange is defined, it is important to understand the energy transfer mechanism in it.

### 2.5.5 Richardson energy cascade concept

In the following sections, one of the most difficult problems in turbulence is introduced: predicting the evolution of freely decaying in isotropic turbulence; where 'freely decaying' means turbulence free from a mean shear which might maintain and shape the turbulence [29].

Before approaching the problem of freely decaying turbulence, it is important to fix the range of vortex (shapes and dimensions) where it is applicable. According to Figure 2.11, the isotropic turbulence is bounded in the upper part by the integral length scale (or energy containing scale) and in the lower part by the Kolmogorov length scale.

Freely decaying turbulence (hereinafter called isotropic turbulence) is made up of a set of shapeless turbulent vortex tubes interacting in a chaotic manner. The isotropic turbulence properties permit themselves to be interpreted by a rather formal, mathematical approach. Richardson speculates that, in a turbulent flow, the energy flux is continually passed down from the large-scale structures to the small scales, after which it is destroyed by viscous stresses. On the other hand, Kolmogorov's theory asserts that the statistical properties of the small scales depend only on the viscosity and on the rate at which energy is passed down through the energy cascade. Furthermore, the main assumption of Kolmogorov's theory is that the small scales are statistically isotropic and universal.

The idea underlying the energy cascade process is that the largest vortex splits or evolves into smaller vortices, without any energy loss. The smaller vortices are themselves unstable; in turn, they pass their entire energy into even smaller structures, and so on. Thus, at every instant a continual cascade of energy from the LS down to the smaller one takes place. The whole process is essentially driven by inertial forces, without any viscosity effect, until the cascade comes to a halt (the size of the smallest vortices becomes so small that $R_\eta \approx 1$). The viscous forces become significant and the dissipation process can start. The range affected by this process is called *the dissipation range* [29] (see Figure 2.8).

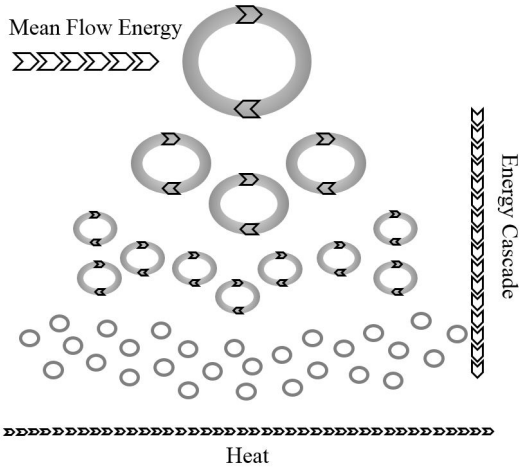


**Figure 2.8:** Energy migrations through the scales

Kolmogorov's theory [79] of a universal equilibrium range is quite a robust result in turbulence, which makes a very specific prediction (*two-thirds law*). The starting point is the structure function 2.66

$$(D_{u_i})^2(r) = \left[u_i'(x_i + r\hat{e}_i) - u_i'(x_i)\right]^2 \tag{2.66}$$

where $(D_{u_i})^2$ is the second order structure function, $u_i'$ is the velocity fluctuation in $x_i$ direction and $r$ is the spatial increment times the unit vector $\hat{e}_i$.

Davidson [29], using a limited list of parameters $(u, l, r, t, \nu)$, assumes that

$$(D_{u_i})^2(r) = F(u, l, r, t, \nu), \tag{2.67}$$

where $F(u, l, r, t, \nu)$ is an universal function in isotropic turbulence (or better the inertial subrange). Using the similarity theory, equation 2.67 can be reduced to

$$(D_{u_i})^2(r) = u_i^2 F\left(\frac{r}{\eta}\right), \quad r \ll l \tag{2.68}$$

where $F\left(\frac{r}{\eta}\right)$ is still a universal function in isotropic turbulence (in the inertial subrange).

Following Kolmogorov [79], the scales of size $r \ll l$ do not retain any of the information which relates to the largest eddies (of size of $l$). Furthermore, the SSs do not feel the effect of the LS structures, because of the different velocities which these scales have. Namely, the characteristic time-scale of the small eddies is very fast compared by the large eddies time-scale [29]. To complete the comment, Davidson [29] suggested that: "the small structures do not feel the large-scale anisotropy, nor do they feel the overall time-dependence of the flow except to the extent that the flux of energy down the energy cascade changes. So, at any instant the small eddies are in approximate statistical equilibrium with the LSs and they are more or less isotropic. This is what Kolmogorov meant by local isotropy and statistical equilibrium. The regime $r \ll l$ is known as the universal equilibrium range".

Going back to the function $D_{u_i}\left(\frac{r}{\eta}\right)$, it is a consequence of *Kolmogorov's First Similarity Hypothesis*, which for large *Re* and $r \ll l$, asserts that $\overline{(D_{u_i})^2}$ have universal form. Recalling that, in isotropic turbulence, the dissipation energy rate is

$$\varepsilon = 15\nu\overline{\left(\frac{\partial u_1}{\partial x_1}\right)^2}; \tag{2.69}$$

where $x_1$ is the streamwise direction.

Moreover, considering an inertial sub-range $\eta \ll r \ll l$, the viscosity is not expected to be a relevant parameter, according to *Kolmogorov's Second Similarity Hypothesis*. Hence, the function $F(r)$ is uniquely determined by $r$

and $\varepsilon$.

$$F_1(r) = \frac{\varepsilon}{15\nu} r^2; \tag{2.70}$$

where the subscript 1 indicates the streamwise direction $x_1$; hereinafter simply named $F$. Following the similarity theory and paying attention to the dimensions, one can yield

$$F(r) = C_k (\varepsilon r)^{2/3}; \tag{2.71}$$

which, in terms of structure function 2.68, that is redefined thanks to 2.71 as follows

$$\overline{(D_{u_i})^2}(r) = u_i C_k (\varepsilon r)^{2/3}. \tag{2.72}$$

Equation 2.72 is known as *two-thirds law* and is valid in the inertial subrange. Pope (2000) fixed the $C_k$ constant equal to 2.0.

In general, $p$ order structure can be defined as

$$(D_{u_i})^p (r) = \left[u_i'(x_i + r\hat{e}_i) - u_i'(x_i)\right]^p \tag{2.73}$$

which, according to Kolmogorov's second similarity hypothesis, in the inertial sub-range $\eta \ll r \ll l$ the $p$ order structure assumes the following form

$$(D_{u_i})^p (r) = C_p (\varepsilon r)^{p/3}. \tag{2.74}$$

For $p = 3$ the four-fifths law is derived and the constant is universal when the turbulence is globally isotropic and the value is $C_p = 4/5$. Hence, under the hypothesis of three-dimensional homogeneous isotropic turbulence, limited

to high Reynolds numbers, equation 2.74 can be rewrote as [80]

$$D_{u_i}^3 = -\frac{4}{5}\varepsilon r, \tag{2.75}$$

or

$$\left\langle D_{u_i}^3 \right\rangle = -\frac{4}{5}\left\langle \varepsilon \right\rangle r, \tag{2.76}$$

The angle brackets $\langle\cdot\rangle$ denote the DA value of a generic quantity. Da in specific flow regions (far from the wall) is equivalent to the ensemble averaging which in turn is equivalent to time averaging over a sufficiently long period of time in a statistically steady turbulence at a high Reynolds number [53]. The law in 2.76 was obtained assuming that the TKE dissipation rate remains constant as kinematic viscosity $\nu$ tends to zero ($\nu \to 0$) in the inertial subrange $\eta \ll r \ll l$. It is important to note that, since the TKE dissipation rate $\varepsilon$ is constant throughout the inertial subrange, the large-scale TKE generation rate is equivalent to the small scale dissipation rate, as suggested by equation 2.69. The use of one velocity component is supported by experimental results, which reveals that the $4/5$-law is applicable even when data is analyzed in a single direction [131]. The $4/5$-law essentially states the energy conservation in the inertial subrange, i.e. the measure of the TKE flux through scales. The key assumption of the Kolmogorov hypothesis is the local isotropy (or the isotropy at small scales), which holds in high Reynolds number turbulence. The difference between equation 2.72 and 2.76 is that the total energy of increments $D_{u_i}$ is taken into account in the two-thirds law, where $u_i$ is the full three-dimensional vector and $D_{u_1}$ refers only to the longitudinal increments, as described in 2.76. Equation 2.72 can be derived directly from the two-point correlation functions of the RANS equations [53, 7]. It expresses the nonlinear normal stress fluxes through scales in the inertial subrange as a function of measurable third-order moments. Both the third-order moments in 2.76 and

2.72 arise from the hypothesis of homogeneous isotropic turbulence. They are the exact laws and provide unique information in the inertial subrange, such as characteristic length-scales and, most importantly, the TKE dissipation rate. They require much more precision and effort to have a simple statistical convergence, where many data sets are required. The third-order moments were used successfully to determine and characterize the turbulent cascade in atmospheric boundary layer flows [21]. In addition to homogeneity and isotropy, the main assumptions were stationarity and high flow Reynolds number. Regarding the isotropy, an alternative derivation is anyway possible [100]. It is important to emphasize that the assumption of isotropy may not be verified in many realistic situations, such as in a geophysical turbulence in the presence of physical factors (e.g. rotation and strong stratification) which modify the flow dynamics with different invariants and instabilities and break the isotropic condition. Generally, the lack of isotropy renders the derivation of the counterpart of the $4/3$-law far more difficult to obtain [45].

### 2.5.6 Energy spectrum in turbulence

As already mentioned, in the inertial subrange the structure function 2.72 should have a universal behavior. To corroborate the last sentence, spectral analysis can be useful. Taking a velocity record, it is made up of harmonics in Fourier modes (see Figure 2.9).

It is quite hard to distinguish turbulent phenomena from a signal in time domain and a further technique is useful to extrapolate information from it; this technique was found in the Fourier analysis, which translate the signal in the so-called Fourier space.

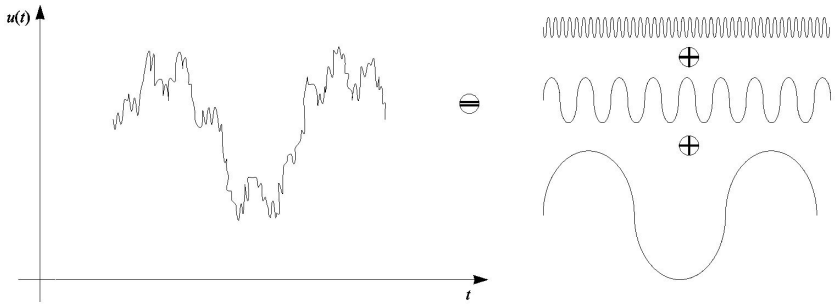


**Figure 2.9:** Harmonics superposition in Fourier Analysis

In general, the direct Fourier transform is defined by

$$U(f) = \frac{1}{2\pi} \int_{-\infty}^{+\infty} u(\tau) e^{-\imath f \tau} d\tau \tag{2.77}$$

and the inverse transform by

$$u(\tau) = \int_{-\infty}^{+\infty} U(f) e^{\imath f \tau} df \tag{2.78}$$

where $u(t)$ is a velocity signal in the time domain and $U(f)$ the corresponding signal in the Fourier space; $f$ is the frequency or temporal frequency, i.e. the number of occurrences of a repeating event per unit time. A recognizable second type of frequency is the space frequency, which is indicated with the name of wavenumber $k$. Using the dimensional analysis, one can easily find the link between frequency and wavenumber. In fact, frequency is defined as $f = [T^{-1}]$, whereas wavenumber has the following dimension structure $k = [L^{-1}]$. Combining these parameters, $f/k = [LT^{-1}] = u$ is obtained, where $u$ is a velocity. In particular, the velocity chosen to transform the wavenumber into frequency and vice versa is the local mean velocity $\bar{u}$. One can write

$$k = \frac{Cf}{\bar{u}}; \tag{2.79}$$

where $C$ is a constant coming from the Fourier transform (it is often $= 2\pi$). The wavenumber is also defined as $k = C/l$. Therefore, Dey [39] yields the length scale as a function of wavenumber as

$$(k_\eta, k_\lambda, k_L) = C\,(l_\eta, l_\lambda, l_L)\,. \tag{2.80}$$

As shown in Figure 2.10, the LSs are on the right side, whereas the dissipation scales are placed on the left side.

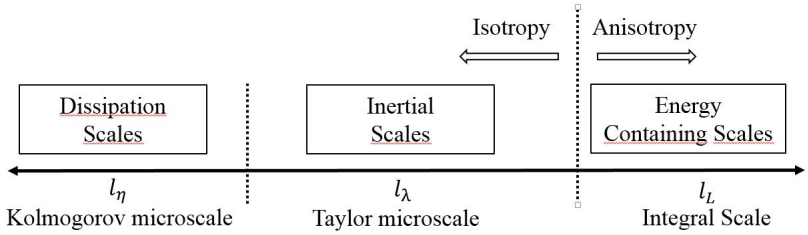


**Figure 2.10:** Turbulent length scales

Assuming a stochastic and ergodic process $u(t)$ and its average value $\bar{u}$, the related fluctuations $u'(t)$ is sill definable as stochastic and ergodic. Hence, the autocorrelation function $R_{u_i u_i}(\tau)$ can be computed

$$R_{u_i u_i}(\tau) = \mathbb{E}\left[u_i'(t) \cdot u_i'(t+\tau)\right] \Rightarrow R_{u_i u_i}(0) = \sigma^2_{u_i u_i}; \tag{2.81}$$

Assuming a signal with zero mean, as $u'(t)$, the autocorrelation of this signal coincides with the auto-covariance, which is twice the TKE ($K$).

In a limited time signal, it is licit to admit that

$$\int_{-\infty}^{+\infty} |R_{u_i u_i}(\tau)| \cdot d\tau < \infty; \tag{2.82}$$

and then the Fourier transform is computable as

$$S_{u_iu_i}(f) = \int_{-\infty}^{+\infty} R_{u_iu_i}(\tau) \cdot e^{-\imath 2\pi f\tau} d\tau; \tag{2.83}$$

where $S_{u_iu_i}(f)$ is the two-sided spectral densities (or simply spectra) and $\imath$ the imaginary unit. The inverse Fourier transform is defined as

$$R_{u_iu_i}(\tau) = \int_{-\infty}^{+\infty} S_{u_iu_i}(f) \cdot e^{-\imath 2\pi f\tau} df. \tag{2.84}$$

Equations 2.83 and 2.84 are called Wiener-Khinchine relations [136].

As stated, in a turbulent signal, where $\tau = 0$, replacing in (2.84) highlights how the sum of all harmonics represent twice the TKE ($K$) [61]

$$R_{u_iu_i}(0) = \sigma^2_{u_iu_i} = \int_{-\infty}^{+\infty} S_{u_iu_i}(f) df. \tag{2.85}$$

This result can be converted easily from the frequency domain to the wavenumber space using the 2.80, giving a faster comparison with the turbulent scales.

Moreover, the one-sided density spectra is preferred, since it is applied easily to the most common equipment. Since the autocorrelation function is even and real, the one-sided density spectra are defined as [61]

$$G_{u_iu_i}(f) = 2S_{u_iu_i}(f) = 2\int_{0}^{+\infty} R_{u_iu_i}(\tau) \cdot e^{-\imath 2\pi f\tau} d\tau. \tag{2.86}$$

Taking into account equation 2.80 and its derivative ($dk = 2\pi df/\bar{u_i}$), it is possible to switch from the frequency to the wavenumber domain

$$\int_{0}^{\infty} G_{u_iu_i}(f) df = \sigma^2_{u_i} = F_{u_iu_i}(k) dk \tag{2.87}$$

to yield

$$G_{u_iu_i}(f) = \frac{2\pi}{\bar{u}_i} F_{u_iu_i}(k)_{k=2\pi f/\bar{u}_i} \Rightarrow f \cdot G_{u_iu_i}(f) = k \cdot F_{u_iu_i}(k); \tag{2.88}$$

which is the premultiplied spectrum (or rather compensated spectrum). This special representation of the energy spectrum gives direct and faster information like peaks or specified spectrum slope (e.g. $k^{5/3} \cdot F_{u_iu_i}(k)$ is used to identify the inertial subrange). Using the Einstein notation, $F_{u_iu_i}$ are simply called spectra. Using the mixed components $F_{u_iu_j}$, one can define the cospectra (or cross-spectra). In general, $F_{u_iu_i}$ is related to the TKE and $F_{u_iu_j}$ to the energy transport in the main directions.

In general, the cross-correlation function, already seen in 2.51, can be rewritten with the Einstein notation

$$R_{u_iu_j}(\tau) = \mathbb{E}\left[u_i(t) \cdot u_j(t+\tau)\right]. \tag{2.89}$$

The relative Wiener-Khinchine function are given by

$$\begin{aligned} R_{u_iu_j}(\tau) &= \int_{-\infty}^{+\infty} S_{u_iu_j}(f) e^{\imath 2\pi f \tau} df \\ S_{u_iu_j}(f) &= \int_{-\infty}^{+\infty} R_{u_iu_j}(\tau) e^{-\imath 2\pi f \tau} d\tau. \end{aligned} \tag{2.90}$$

being the relation 2.85 symmetric $R_{u_iu_j}(\tau) = R_{u_ju_i}(-\tau)$; then

$$S_{u_iu_j}(-f) = S^*_{u_iu_j}(f) = S_{u_ju_i}(f) \tag{2.91}$$

where $S^*_{u_iu_j}(f)$ is the complex conjugate function of $S_{u_iu_j}(-f)$. As it was for 2.53, also the 2.90 for $\tau = 0$ is recognized as the Reynolds stress in the

frequency space [61].

$$R_{u_i u_j}(0) = \overline{u_i' u_j'} = \int_{-\infty}^{+\infty} S_{u_j u_i}(f) df. \tag{2.92}$$

Guala et al. [61] use to convert the two-sided estimate cross-power spectral density to one-sided wavenumber cospectrum

$$\Phi_{u_i u_j}(k) = S_{u_i u_j}(-k) + S_{u_i u_j}(k) = 2Re\left\{S_{u_i u_j}(k)\right\}. \tag{2.93}$$

**-5/3 law**

The use of the velocity correlation function instead of the pure velocity signal is supported by the hypothesis that small scales are statistically isotropic [53] and then

- space translations $x + r$;
- scaling $(t, x, u) \rightarrow \left(\lambda^{1-h} t, \lambda x, \lambda^h v\right)$ for any $h$ and $\lambda > 0$;

where $x$ is a space position, $r$ a generic space increment and $u$ a velocity vector. The Kolmogorov treatment of small scale turbulence is based on the hypothesis that, at high Reynolds numbers and far from boundaries, the symmetries of Navier-Stokes equation are restored for statistical quantities. Hence, considering the velocity increment $\Delta u(x,l)$ with $l \ll L$ the homogeneity in a statistical sense requires $\Delta u(x+r,l) \overset{law}{=} \Delta u(x,l)$. The last relation attributes an equal probability distribution function (PDF) of $\Delta u(x+r,l)$ and $\Delta u(x,l)$ [141]. The second Kolmogorov similarity hypothesis states that, at large Reynolds number, in the inertial range, the PDF of $\Delta u(x,l)$ becomes independent of viscosity $\nu$. This hypothesis implies that the scaling invariance is statistically recovered in the values of the scaling exponent $\Delta u(x,\lambda l) \overset{law}{=} \lambda^h \Delta u(x,l)$. As highlighted in section 2.5.5, the exponent is positive and $h = p/3$.

According to the second-order structure, the spectrum associated to the 2/3-law in Fourier space is

$$\Phi_{u_i u_i}(k) = C\varepsilon^{2/3}k^{-5/3}. \tag{2.94}$$

This is the most important implication of the Kolmogorov hypothesis, providing the turbulent energy spectrum as a function of the wavenumber. The analysis of the spectral density function involves the individuation of the inertial subrange. Furthermore, the determination of the inertial subrange enables turbulence scales and energy dissipation rates to be found. Hence, in the inertial subrange the universal form of the Kolmogorov spectrum (equation 2.94) is observed. This is a consequence of the already mentioned Kolmogorov hypotheses applied to the second-order structures.

### 2.5.7 Large scales

Kolmogorov's law is considered to be one of the successful results in turbulence. As already mentioned, it is confined only at the small scales. This is unfortunate, because of the small scales having slight practical importance in the engineering field. Phenomena such as dispersal of pollutants or transport of momentum are usually controlled by the large eddies [29].

Unfortunately, the LS motion can be influenced by the geometry of the flow and the associated time-scales are comparable to the mean flow time-scale. This statement suggests a memory of the LS towards the flow histories and thus a non-universal form of the turbulent characteristics, not even in statistical form, as in the inertial subrange [115].

According to the previous sections, there are enough elements to give a rough graphical representation of the turbulent scales in Figure 2.11 [39].

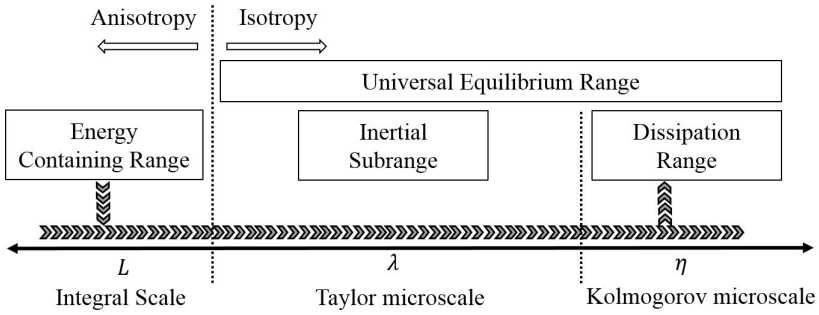


**Figure 2.11:** Energy flux through the scales

Hence, the turbulence can be split into two main ranges: isotropic turbulent scale, in which universal laws seem to work quite well, and anisotropic scale, where the mean flow influence makes any prediction more complex.

In addition, the LS structures play a key role in the transport phenomena, explaining why they have been the target of numerous investigations, not only in OCFs, but also in any canonical turbulent wall flow, such as pipe, channel or Turbulent Boundary Layer (TBL) flows. In fact, the influence of the topographic wall characteristics, regarded as the manifestation of the shear instability [138, 137], is the major actor in LS energy production.

Moreover, large eddies in wall flows are classified according to the nomenclature introduced by Kim and Adrian [73], which distinguish LS from and VLS. Kim and Adrian [73], using single hot-film probe and premultiplied spectra analysis, found hairpins aligned coherently, which represent a LS of about 2 times the pipe radius, and conjectured that the VLSs are formed by hairpins packets, in turn, aligned coherently to reach dimension of about 10 times the pipe radius.

Adrian et al. [3] focused their attention on energy-containing structures in the outer region, using 2D Particle Image Velocimetry (PIV), finding packets of hairpins, which can be seen as VLSs (more than 1000 wall units).

This result was substantiated by Ganapathisubramani et al. [55], using a 15 Hz stereoscopic PIV. Dennis and Nickels [38], through 3D PIV measurements, found that most of the structures had a length minor than 7 wall units, which contradicts the existence of VLS. On the contrary, LS alignment in the streamwise direction was observed; this fact suggests the existence of long meandering streaks. Through Direct Numerical Simulation (DNS), VLSs with a dimension of 10 times the water depth were also found by del Álamo and Jiménez [34]. Further, Hutchins and Marusic [69] used the term "superstructure" to identify meandering-type long structures captured through 10 hot-wires and compared with PIV and DNS literature results. They visualized meandering structures with a dimension of 20 times the outer length. Mejia-Alvarez et al. [97] describe a large spatial heterogeneity in the form of low- and high-momentum flow pathways, suggesting that these pathways could represent the meandering of the LS.

Nevertheless, the previous literature is in accord with the hairpin packs conjecture, Hwang and Cossu [70] designed a "conceptual" numerical experiment, where they gradually remove the smaller scales from the flow. The authors found that the LSs can self-sustain, even when smaller-scale structures, populating the near-wall and logarithmic regions, are artificially quenched. Despite the fact that natural OCFs are almost always in rough-bed condition, rough-wall received less attention, because of the undoubted difficulties in measuring inside the layers influenced by the roughness. Often, such measures encounter errors, identified as high noise. This noise is difficult to eliminate without a strong data manipulation, which can distort the measures and then the results. One of the first works is due to Klaven [77], who observed LSs with dimensions between 4 and 7 times the water depth, which decrease as roughness increases. LSs in low-submergence OCFs was also observed by Kirkbride and Ferguson [76],Buffin-Bélanger et al. [16],

Shvidchenko and Pender [127], Hofland and Booij [65], Roy et al. [122], Marquis and Roy [92] and Franca and Lemmin [52]. Kirkbride [75] refers the LSs origin with vortex shedding and wake flapping in the lee of asperity bed roughness elements. Moreover, a feedback mechanism between large-scale coherent structures and vortex shedding in the nearness of pebble clusters was proposed by Roy et al. [121] and Roy and Buffin-Bélanger [120].

Rosenberg et al. [119], through the streamwise velocity spectra reported for smooth- and rough-wall turbulent pipe flow over a large range of Reynolds numbers, found that the turbulence structure far from the wall is seen to be unaffected by the roughness. An approach to identify LS structures formed by flow interaction with large roughness elements was proposed by MacVicar and Roy [87, 88], Lacey and Roy [82], who detected the LSs using turbulent wake statistics. Most recently, Cooper and Tait [25, 27, 26] and Hardy et al. [62, 63] used PIV to have the whole flow field view in flume experiments in rough-wall conditions at high Reynolds numbers. The key findings suggest that, as the Reynolds number increases, the visual distinctiveness of the coherent flow structures becomes more defined, and these are clearly seen as 'bulges' of lower velocity fluid originating at the bed and intruding into the outer flow. To my knowledge, the only results that show coherent flow structures similar to VLSs of velocity fluctuations measured in a gravel-bed river, describing the so-called flow pulsations, are reported in Marquis and Roy [93], in which LSs and VLSs are recognized to occupy the entire flow depth.

As one can see, in the literature no deal has been attained about the LS and VLS formation process or even existence. Hence, the open question on the nature of LS structure in OCFs over a rough-wall promotes new works. In the next chapters, a systematic analysis, using premultiplied power spectra of autocorrelation and cross-correlation velocity function, is proposed to

establish which scales are involved in the TKE and turbulent momentum transfer in the main directions.

# Chapter 3

# Experimental equipment and procedure

*"The best way to show that a stick is crooked*
*is not to argue about it or to spend time denouncing it,*
*but to lay a straight stick alongside it."*
*Dwight Lyman Moody*

## 3.1 Flume description

The experiments on turbulent OCFs over rough beds were performed at the *Laboratorio "Grandi Modelli Idraulici"*, *Università della Calabria*, Italy, in a 1 m wide, 0.8 m deep and 16 m long rectangular tilting flume. A 2.5 m long test section was placed at 10 m from the inlet. It had glass walls, in order to permit the observation of the runs. The flume inlet consisted of a stilling tank, an uphill slipway, a perforated-pipe diffuser, a fine grid (having cell size of 1 mm $\times$ 1 mm) and a honeycomb to straighten the flow and to damp the residual pump vibrations. The honeycomb was made of polycarbonate triangular ducts.

Each duct was 40 cm long and had 1 cm long sides. An adjustable tailgate was placed at the outlet in order to set the water depth. Water was collected in a downstream tank, from which it fell in a restitution channel, where another honeycomb and a Bazin weir were placed to measure the discharge before the water entered the main sump. In the sump, a submerged pump was placed to feed the flume inlet (see Figure 3.1 (a) and (b)).

(a)


(b)

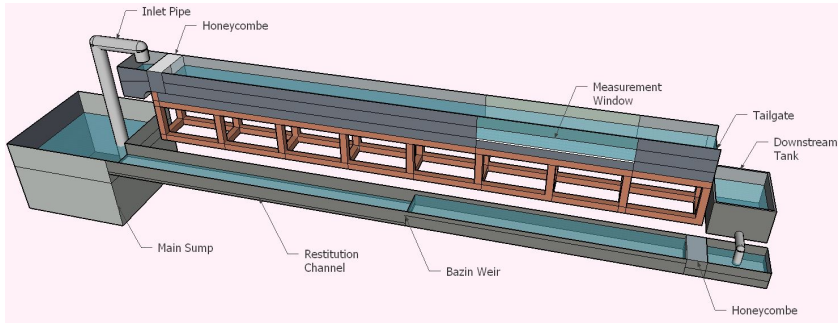


**Figure 3.1:** Flume details; (a) picture of the installation; (b) 3D flume reconstruction.

The slope was adjusted through two hydraulic jacks, whereas the water depth was set through the downstream tailgate, which was never moved after having set the design water depth. The hydraulic conditions were fixed at the beginning of each experiment and kept constant easily by switching the pump on/off.

## 3.2 Flow rate measurement

The flume ends with a stilling chamber which feeds an underground restitution channel. The 13.5 m long and 0.993 m wide restitution channel was fitted out with a flow rate measurer, a Bazin weir. The discharge predictive formula for a rectangular weir is given by Kindsvater and Carter [74]

$$Q = C_e B_e H_e^{2/3} \tag{3.1}$$

where $Q$ is the discharge, $H_e = H_s + 0.001$ m is the effective water depth (in which $H_s$ is the water depth above the weir and 0.001 m a calibration correction factor), $B_e = B_s + 0.001$ m $= 0.994$ m is the effective channel breadth ($B_s$ being the channel breadth) at the weir edge level and 0.001 m a calibration correction factor. The discharge coefficient $C_e$ is given by the following formula

$$C_e = 1.78 + 0.22\frac{H_e}{p_s} \tag{3.2}$$

where the weir height is $p_s = 0.355$ m. The constancy of the flow rate was carefully checked during the experiment through the Bazin weir, which had an accuracy of less than 2%.

## 3.3 Bed surface acquisition

Before each test started, the bed surface was acquired with a 3D laser scanner (model Vivid 300/VI-300, produced by Minolta, Figure 3.2).


**Figure 3.2:** Laser scanner Vivid 300/VI-300, produced by Minolta.

The laser scanner adopts the principle of similar triangles to identify the location of points on the surface. This technique is one of the most commonly used methods by 3D scanners, since the laser can digitize data with high accuracy during the acquisition time. To illuminate the object surface, the beam of light emitted by the laser diode and propagating towards the object was adequate (Figure 3.3).

The light beam reflected from the object was projected by a lens system and then acquired with a device sensitive to light (the receiver) or a position sensitive photo-detector (PSD). Two amplifiers convert the two photocurrents generated by the PSD voltage signals. Afterwards, these signals are processed from analogue signals into digital signals through the A/D converters and a processor. The displacement of the light stripe along a relevant predetermined

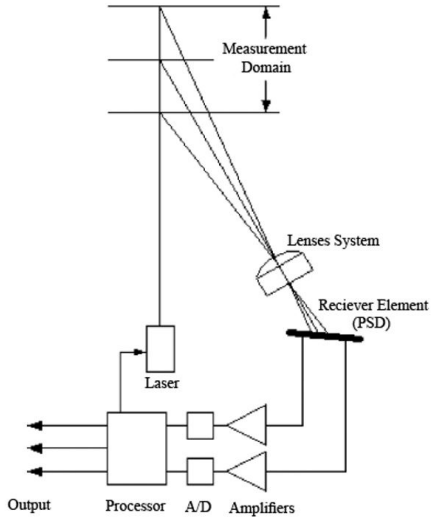


**Figure 3.3:** Schema of a sensor that operates on the basis of the principle of similar triangles.

direction was carried out through the use of a Galvano mirror. This device consisted of a mirror able to rotate around a horizontal axis. Therefore, changing the mirror inclination angle resulted in the movement of the light beam reflected from the same location (Figure 3.4). As Figure 3.4 shows, all the surface can be acquired through the light beam emitted from inside the scanner.

Accuracy and installation of 3D laser scanner By using the 3D laser scanner Minolta Vivid 300/VI-300, the object surface elevation can be captured from the distance of $H_L = 0.55$ m to a maximum distance of 1.2 m from the instrument (Figure 3.5). The acquisition range consisted of a square area with side size varying from 185 mm at the minimum distance (0.55 m) to 395 mm at the maximum distance $H_L = 1.2$ m. The accuracy of the instrument depends on $H_L$ and on the direction. In fact, the accuracy along the parallel direction (with respect to the flume bed) varies from 0.95 mm at the minimum

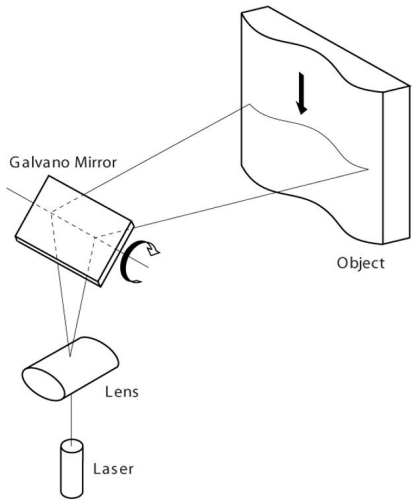


**Figure 3.4:** Operation of the Galvano mirror for emission of laser on predetermined area.

$H_L$ to 1.91 mm at the maximum $H_L$; analogously, along the vertical direction it ranges from 0.45 mm to 1 mm. As the distance from the instrument to the surface decreases, the resolution and accuracy of the acquisition increases. In contrast, at a lower distance more images are usually needed and the measure uncertainty increases during the operation of image merging, since the corresponding points of two different images cannot always be superimposed exactly. In this study, in order to measure the bed surface, the laser scanner was placed on a suitable support-box and carriage, so that the laser emission window and entrance of the camera were parallel to the flume bed; in addition, the baseline of the instrument was set in accordance with the flow direction, i.e. the longitudinal flume axis (Figure 3.5). The support-box was installed on a carriage moving longitudinally along the rails mounted on the flume walls and transversally along other rails orthogonal to the previous ones. In order to acquire the sediment bed surface and to process the related data, the 3D laser scanner was connected through an SCSI port to a computer with a 2.2

GHz processor and 512 MB RAM. In this study, the laser scanner was located at a distance of $H_L \approx 70$ cm from the bed surface, with accuracy along the parallel and vertical directions (with respect to the bed surface) at 1.2 and 0.6 mm, respectively. For each image, the acquisition window was a rectangular area of about 22.5 cm $\times$ 24.5 cm.

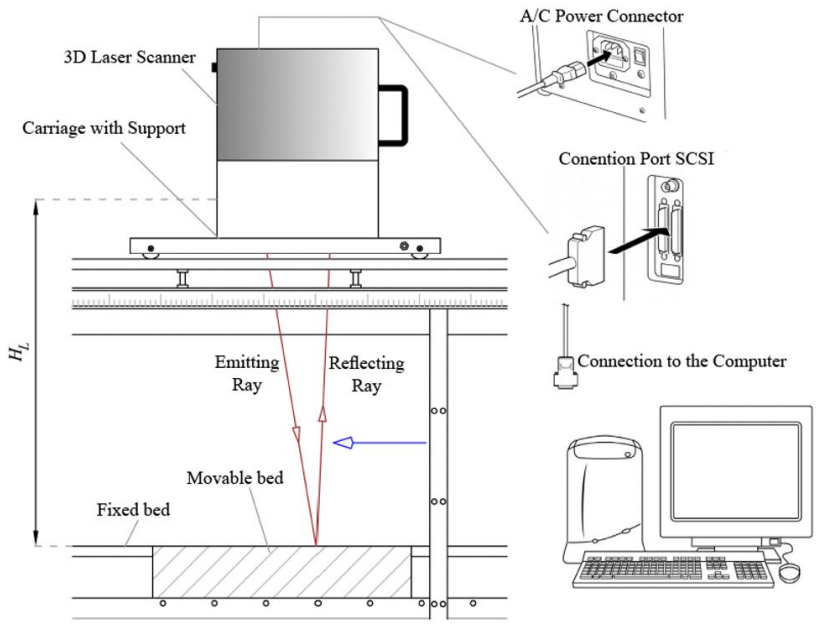


**Figure 3.5:** Details of the installation used to acquire the surface.

In the next section, the laser scanner data will be used to define a statistical function ($\phi_s$), in order to find unambiguous values characterizing the bed roughness.

## 3.4 Roughness geometry function

A characteristic of fluvial gravel beds is their poor sorting. To simulate these beds, gravel was randomly spread in a layer of height equal to approximately

of $4d_{50}$, in order to create the sediment bed. Many authors attempted to derive a roughness parameter from the grain size distribution [83, 86, 17, 15, 11]. The median diameter $d_{50}$ is often used as a parameter to describe the bed roughness. Three sediments were selected for the experimental campaign: pebbles, medium gravel and coarse gravel; the median diameters are reported in table 3.1. Figure 3.6 shows three samples of the sediment grains used in the experiments; three tests were performed, each one for a given $d_{50}$.


**Figure 3.6:** Beds sediment grains.

| | *Test* 1.1 | *Test* 1.2 | *Test* 1.3 |
|---|---|---|---|
| $d_{50}$ (mm) | 70.0 | 30.0 | 10.0 |

**Table 3.1:** Sediment median size.

The single parameter $d_{50}$, is not sufficient to give statistical information as required by the DAM. In fact, different sediment beds with the same $d_{50}$ but different grain-size distribution present different roughness. In addition, pebbles are not easy to sieve, and the oblong shapes produce inaccurate results. Hence, according to the DAM, a roughness geometry function (RGF) is

introduced to characterize the sediment bed in terms of sediment distribution. The use of the laser scanner for bed surface acquisition is crucial in order to assess an accurate roughness geometry function. Figure 3.7 shows the laser scanner acquisitions of the three beds.

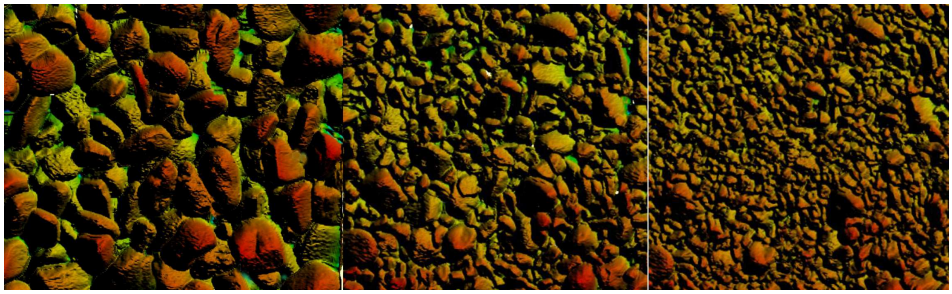

**Figure 3.7:** Bed acquisition through laser scanner. In the left side figure pebbles bed surface, in center of figure the coarse gravel and in right side figure the gravel bed surface.

In the technical literature [41], the Gaussian Distribution (GD) was found to be adequate to describe a gravel bed. In the present tests, the GD described well the gravel bed statistical parameters, but it was inappropriate in the pebble bed case. Therefore, several statistical distributions were tested and the best fit between experimental and statistical distributions was obtained through the gamma distribution (here named $\phi_s$). It is more general than the GD and, through the variation of its parameters, it can assume different shapes. The gamma distribution $\phi_s$ has two free parameters, usually named $a$ and $b$. In brief, $\phi_s(\hat{z})$ is

$$\phi_s(\hat{z}) = \int_0^{\hat{z}} \Gamma(\hat{z})d\hat{z};\ \Gamma(\hat{z}) = \frac{b^a}{\Gamma(a)}\hat{z}^{a-1}e^{b\hat{z}};\ \Gamma(a) = \int_0^{\infty} \hat{z}^{a-1}e^{b\hat{z}}d\hat{z} \qquad (3.3)$$

where, with respect to the maximum crest level, $\hat{z} = z/h_w$ is the dimensionless elevation, $z$ is the elevation and $h_w$ is the water depth; $\Gamma$ is the Gamma function with shape parameter $a$ and inverse scale parameter $b$ (both parameters are

positive real numbers). Figure 3.8 shows the $\phi_s$ function computed through the Gamma function for both gravels and pebble tests.

Note that, by using a point gauge or an overhead scanner, the estimation of the $\phi_s$-function is only suitable for the upper 70% of the interfacial sub-layer thickness, in order to avoid the function becoming zero below the maximum crest level of the porous medium [1, 40]. In the present tests, the use of the laser scanner produced $\phi_s$ functions equal to zero at negative elevations (Figure 3.8); however, no velocity measurements were taken in the lower 30% of the interfacial sub-layer thickness and hence the $\phi_s$ functions were used only in the appropriate range.

The value of the standard deviation of $\phi_s$ is assumed as the mean roughness length, $k_s = a^{0.5}b$. Table 3.2 reports the values of $k_s$ and the statistical roughness scale ($\Delta_R = 3 \cdot k_s$), which is defined as the biggest gap ($\approx 99\%$) into the granular bed.

| | *Test*1.1 | *Test*1.2 | *Test*1.3 |
|---|---|---|---|
| $k_s$ (mm) | 16.91 | 8.86 | 6.19 |
| $\Delta_R = 3k_s$ (mm) | 50.73 | 26.28 | 18.57 |

**Table 3.2:** Roughness parameters.

According to the DAM, $\phi_s(\hat{z})$ was used to compute the form-induced stress, whereas $\Delta_R$ was be tested as a possible scale of many quantities.

## 3.5 Velocity measurements

A four-beam down-looking Acoustic Doppler Velocimeter (ADV) probe (Nortek Vectrino) was used to measure the 3-D instantaneous velocity components (streamwise, $u$, spanwise, $v$, and vertical, $w$, with fluctuations $u'$, $v'$ and $w'$, respectively).

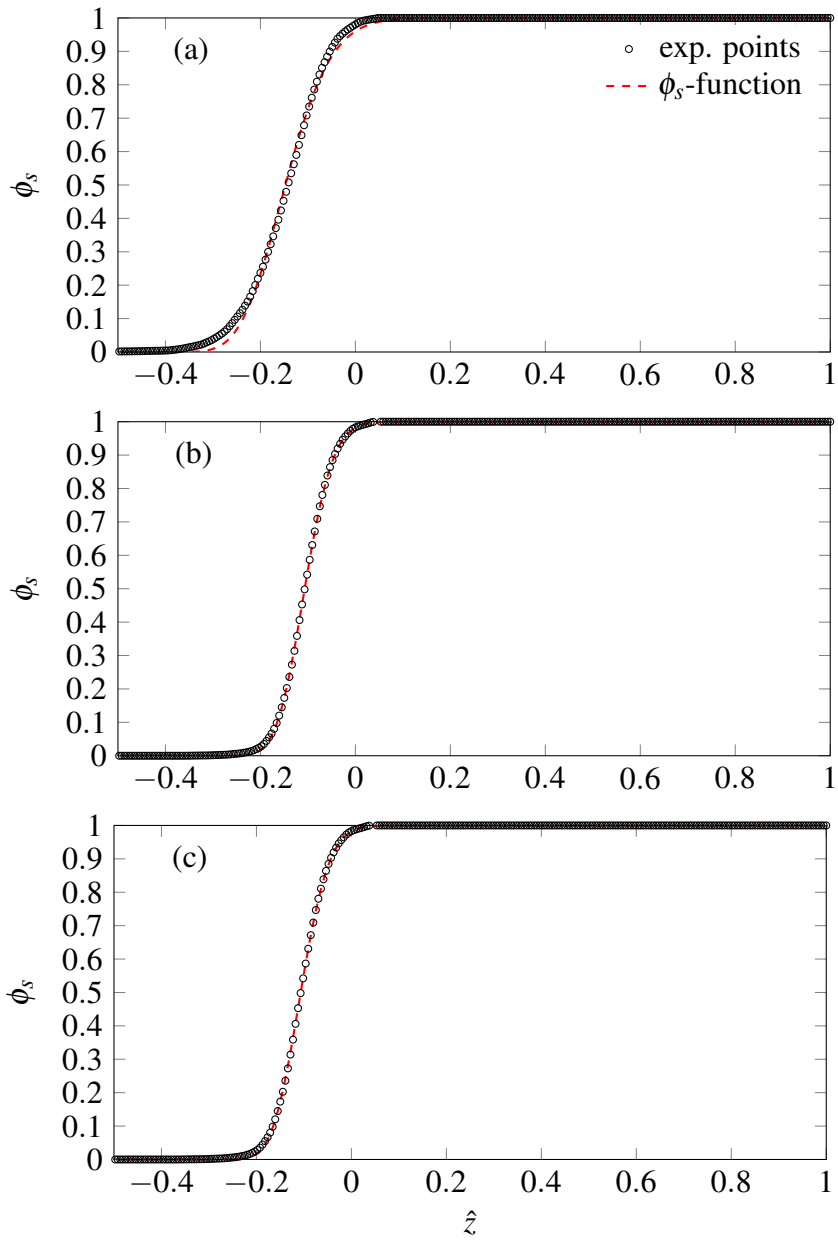


**Figure 3.8:** (a) pebbles bed geometry roughness function; (b) coarse gravel bed geometry roughness function; (c) gravel bed geometry roughness function.

The ADV consists of one emitter surrounded by four receivers (Figure 3.9), each of them measuring one projection of the velocity components.

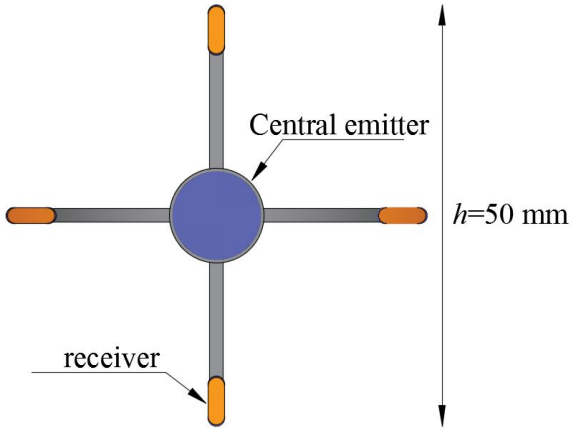


**Figure 3.9:** Acoustic Doppler Velocimetry.

The emitter generates an acoustic wave of frequency $f_e$ and wavelength $\lambda_e = c/f_e$, $c$ being the celerity of sound in the fluid. The acoustic wave is scattered by acoustic targets (water impurities) moving at the fluid velocity $v$, which are reflected and detected by the receiver. The reflected wavelength $\lambda_r$ and the corresponding frequency $f_r = c/\lambda_r$ of the acoustic wave are distorted by the target velocity (Figure 3.10).

The data sampling rate and the sampling duration were 100 Hz and 300 s, respectively; they were found to be adequate in order to achieve the statistically time independent turbulence quantities, as obtained by Dey and Das [40].

An ADV down-looking configuration probe was selected, because it allows exploring deeply into the roughness layer. On the other hand, since the ADV control volume is located 5 cm below the probe, the upper $\sim 5$ cm of the water column (close to the water surface) could not be an object of

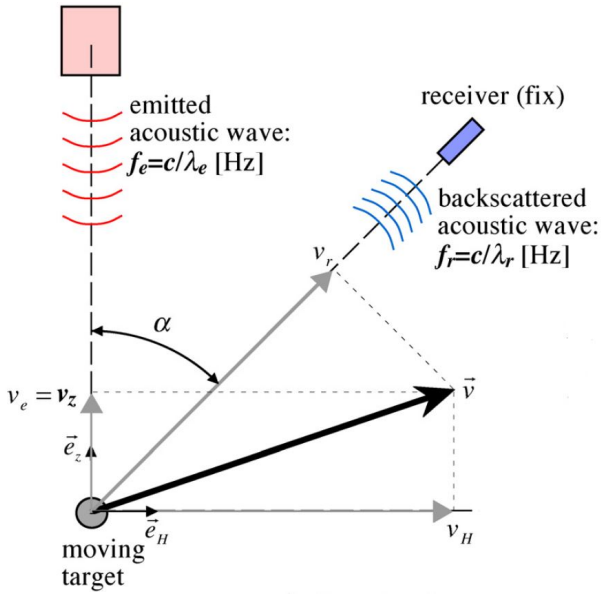


**Figure 3.10:** Acoustic Doppler Velocimetry operation [14].

measurement, owing to the fact that the ADV probe cannot work out of water (Figure 3.11). Hence, measurements were taken from the gaps among the sediment grains up to $\sim$ 5 cm below the water surface.

In the ADV user manual, the sampling volume is described as a cylinder with a fixed diameter of 6.5 mm and a variable height from 1 to 9 mm. The definition of the sampling volume is a crucial issue, in order to set the properly resolved scales in the spectral analysis: as widely discussed in the following sections, the resolved scales cannot be smaller than the sampling volume, producing a significant limit for the resolved scale even if the sampling frequency of the ADV could resolve smaller scales. This is due to the fact that inside the sampling volume an average velocity is computed. Namely, the particles (which are simultaneously present inside the sampling volume) transmit to the receiver their own distorted frequencies, which will be averaged by the instrument. Hence, it is easy to image that only coherent

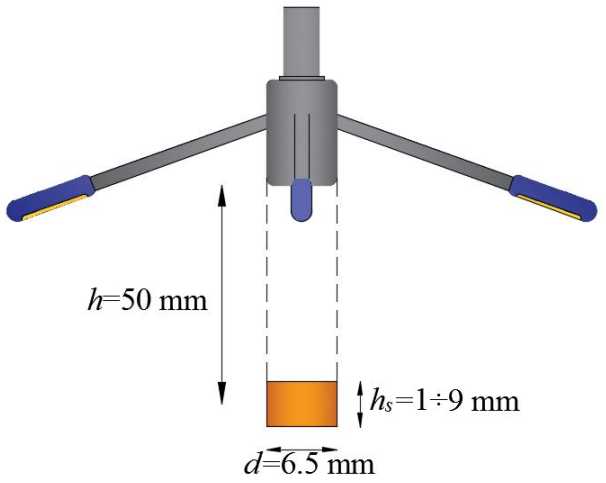


**Figure 3.11:** ADV sampling volume dimensions and position.

particle motions bigger than the sampling volume will be observed in the spectral analysis.

Although high resolution ADV measurements are known to suffer from parasitical noise contributions [49, 56, 84, 140, 95, 67], the four-receiver ADV gives redundant information on one velocity component, which provides an assessment of the noise level.

The four-beam Vectrino system has a redundancy for the $w$ component, since two components $w_1$ and $w_2$ are simultaneously measured by two beams. The variance $\sigma_z^2$ of the noise is expressed as $\sigma_z^2 = 0.5(\sigma_{z1}^2 + \sigma_{z2}^2)$, where $\sigma_{z1}^2 = \overline{w_1' w_1'} - \overline{w_1' w_2'}$ and $\sigma_{z2}^2 = \overline{w_2' w_2'} - \overline{w_1' w_2'}$. It was considered that data with $\sigma_z^2 < 0.3$ had no noise, as they corresponded satisfactorily to Doppler signal correlations between transmitting and receiving pair of pulses greater than 70. During the experiments, a minimum signal-to-noise ratio (SNR) was kept as 15. Even if the measurements are carefully taken and the conditions regarding the SNR and correlation coefficient are satisfied, the velocity signals can be

still affected by errors, producing spikes. Despiking is therefore necessary to discard the wrong measurements.

### 3.5.1 Velocity Data Despking

Goring and Nikora [59] detect the spikes as a result of aliasing of the Doppler signal and the phase shift between the outgoing and incoming pulses caused by the reflection from surfaces of complex geometries (e.g., pebbles). The first step of despiking is the spike individuation, which is based on a restrictive analysis of both methods which are presented here: the Acceleration Thresholding Method (ATM) and the Phase-Space Thresholding Method (PSTM). The ATM is based on the fact that in steady flow conditions the instantaneous acceleration cannot exceed the acceleration of gravity $g$ increased by a certain factor $\lambda_a$. By observation, respecting this condition can produce the rejection of valid data points. Therefore, an additional condition was introduced: in order to reject the points detected as spikes, the acceleration threshold and the absolute standard deviation $\lambda_\sigma \sigma$ with respect to the mean velocity should both exceed their respective limit values. The ATM can be summarized in the following steps:

1. calculate the temporal acceleration;
2. calculate the absolute standard deviation;
3. verify the condition on the acceleration threshold;
4. verify the condition on the absolute standard deviation;
5. if both conditions are satisfied, then replace the spikes with an average value (as explained later), otherwise the detected points are not considered as spikes and are not replaced;

6. repeat all the above steps until no more spikes are detected.

Goring and Nikora [59] introduced the PSTM, which uses the phase-space plot, in which the variable and its derivatives are plotted in various combinations. The authors identified an ellipsoid cloud, formed by a cluster of first and second velocity derivatives. Points outside the ellipsoid are designated as spikes and then rejected. The PSTM is an iterative method, which runs until the number of points identified as spikes falls to zero. Note that the PSTM uses no-temporal derivatives, because their values can procedure complex solutions. The iterative PSTM follows the next steps:

1. calculate non-temporal first and second derivatives (do not divide by the time step);

2. calculate the maximum standard deviations of all the three variables (velocity, first and second derivatives); note that the combination of the standard deviations is used to compute the ellipsoid axes;

3. calculate the rotation angle of the principal axis;

4. for each projection in phase-space, identify the points that lie outside the ellipse and replace them with an average value (as explained later).

Figure 3.12 from Goring and Nikora [59] shows the PSTM plots of a spike-contaminated signal. Spike replacement is an arbitrary procedure; for the purpose of this work, which is focused on the largest scale motion, the overall mean of the signal is considered as appropriate to replace the spikes.

## 3.6 Flow conditioning

A series of preliminary tests were conducted in order to prevent any source of noise in the measurements as much as possible. First of all, the free-stream

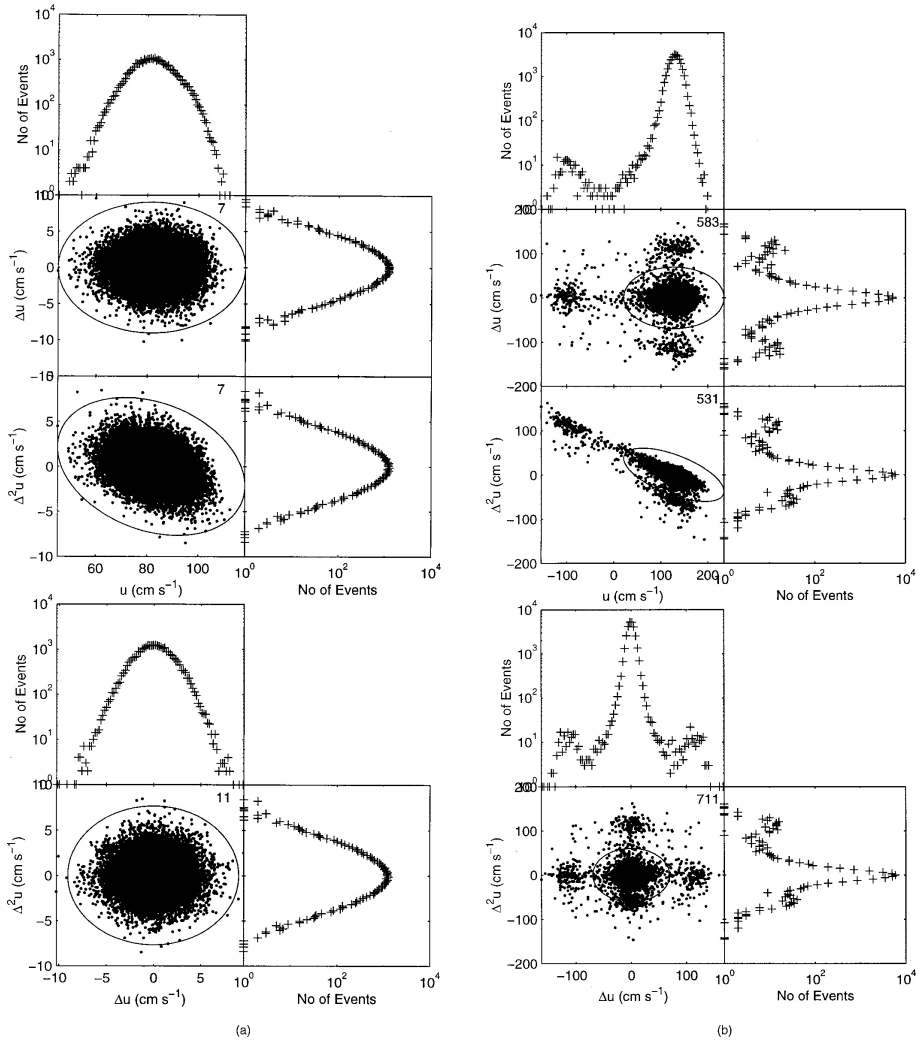


**Figure 3.12:** Goring and Nikora [59] Phase-space plots for clean dataset (left panels) and contaminated dataset (right panels).

turbulence intensity, defined as the ratio $T_u$ of the second order velocity moment $u_{rms}$ (rms: root mean square) to the mean free-stream velocity $U_\infty$, was computed as follows

$$T_u = \frac{u_{rms}}{U_\infty}. \tag{3.4}$$

In order to capture the incoming turbulence at the flume entrance, this parameter was calculated taking a measure near the inlet in a position out of the turbulent boundary layer (at $0.5h_w$ and 0.5 m downstream of the honeycomb in Figure 3.13).

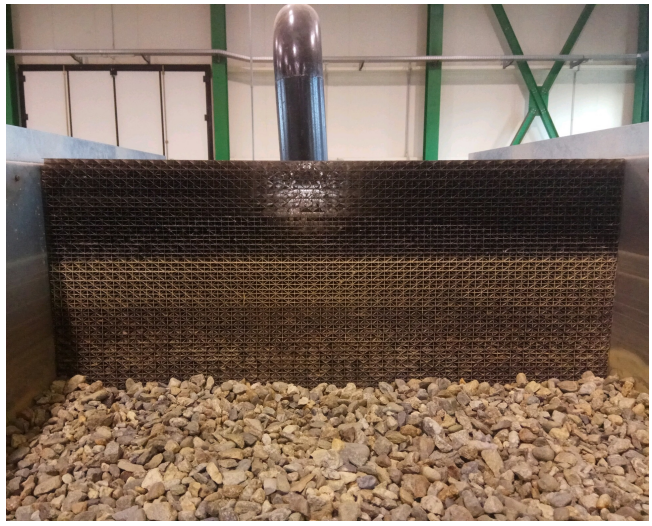

**Figure 3.13:** Inlet detail

In this position, the velocity signal is taken as an indicator of incoming turbulence generated by the pump-inlet pipe system. In table 3.3 the values of $T_u$ are reported in a configuration without any tool to reduce the incoming turbulence ($C_0$) and in a second configuration compounded by the perforated-pipe diffuser, the fine grid and the honeycomb described at 3.1 ($C_1$)

| | $Tu$ |
|---|---|
| $C_0$ (%) | 16.91 |
| $C_1$ (%) | 3.68 |

**Table 3.3:** Free stream turbulence

Configuration $C_1$ presents a strong reduction of $T_u$. Furthermore, the measurement window, located 10 m downstream of the inlet, is far enough to

guarantee the complete dissipation of incoming turbulence, which is replaced by the turbulence generated by the rough bed.

In addition, preliminary spectral analysis was carried out in order to compare the signal not affected by the turbulence generated in the highly rough bed, but only by the free-stream turbulence (measuring point is at $0.5h_w$ and 0.5 m downstream of the honeycomb). Figure 3.14 anticipates the spectral analysis presented in the next chapter.

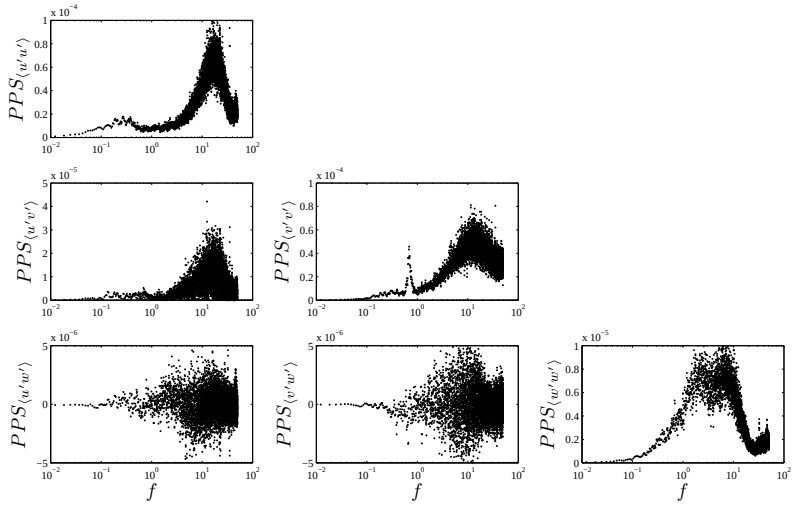


**Figure 3.14:** Free-stream turbulence spectra.

Figure 3.14 shows that the energy contained in the spectra is of the order of $10^{-4}$ m$^2$/s$^2$ for the spectra (diagonal subfigures) and $10^{-5}$ m$^2$/s$^2$ for the co-spectra (off-diagonal subfigures). However, this residual energy, generated by the pump, is negligible with respect to that generated by the bed roughness and flow motion. A specific frequency (30 Hz) is affected by a precise peak; this frequency is influenced by the pump rotation frequency, which is about 30 Hz. Anyway, the peak related to the pump was dissipated and it was not visible in any other spectra downstream (see section 5.3). The shape of $\langle u'w'\rangle$

premultiplied cospectra was very relevant, namely its mean value was $\sim 0$ at any frequency, which is a sign of isotropic turbulence from large to small scales.

## 3.7 Measuring grids

As specified in section 3.8, the test section is placed at 10.8 m downstream of the inlet, along the flume centerline, in order to avoid the side-wall effects. Figure 3.15 shows the measuring grid compound by 25 vertical velocity profiles, equally spaced each 2 cm along the streamwise direction, 0.5 cm vertically spaced in the upper part of the water depth (80% starting from the water surface) and 0.3 cm vertically spaced in the lower part of the water depth (in the remaining 20% of the water depth). The velocity profiles were measured in order to use the DAM properly in the following chapters. The measurement grid in the *xz*-plane was extended from the lowest accessible position into the bed gaps up to a level below the water surface where the last measure was compatible with the ADV configuration (see Figure 3.15).

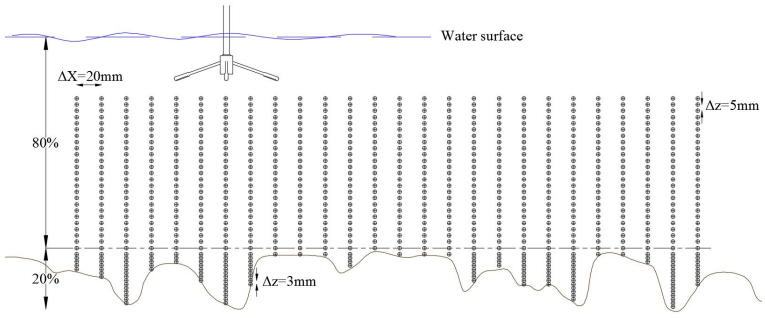


**Figure 3.15:** Example of measurement grid.

In Figure 3.16a a lack of points is visible in the measurement grid. In fact, some points were missing owing to the very high number of spikes in

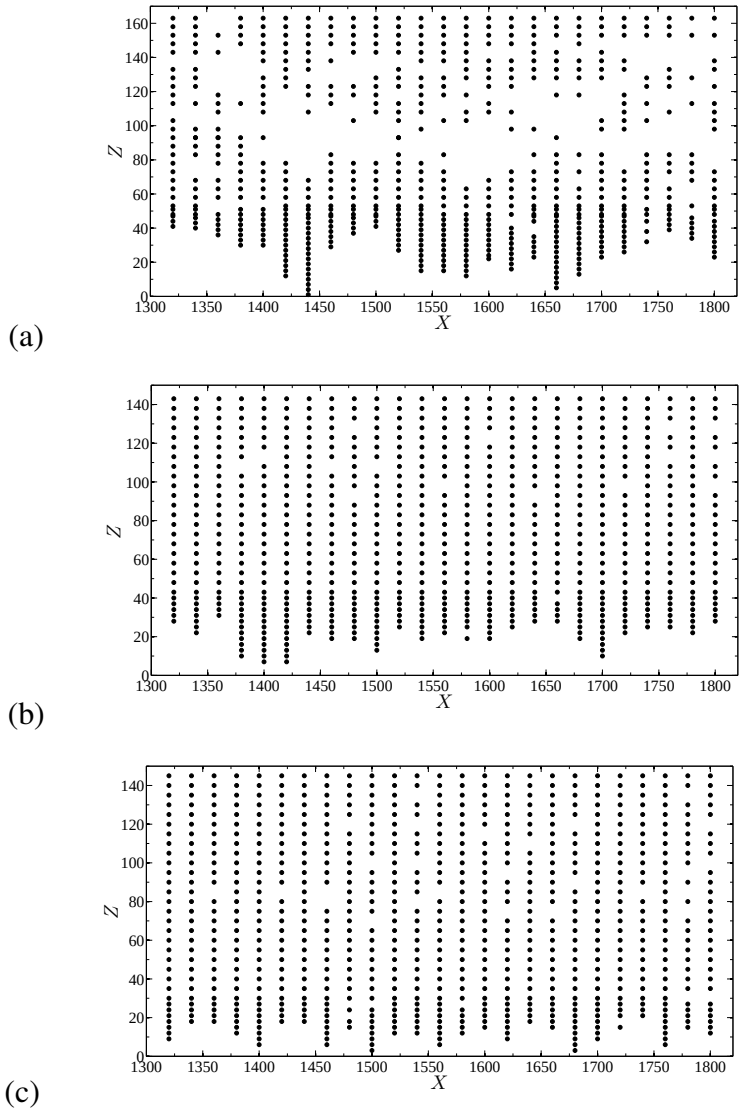


(a)

(b)

(c)

**Figure 3.16:** Measurement grid in Test 1.1 (a), Test 1.2 (b) and Test 1.3 (c)

the measurement records, which made the despiking method inapplicable. Such a situation may occur when the ADV pulses are reflected from a bed of complex geometries (e.g., pebbles or cobbles on the bed of a stream; [59]).

Hence, the cause of this kind of noise in a rough-bed is the overlap of reflected echoes because of the non-regular bed surface. Namely, the sound waves emitted by the ADV probe were reflected by the bed surface, overlapping the sound waves reflected in the ADV sampling volume. The velocity data corresponding to the missing points showed very noisy signals; therefore, a severe data manipulation was required, since the spikes affecting $u(t)$, $v(t)$ and $w(t)$ should be deleted and replaced in some way [59]. Hence, in order not to introduce an over-manipulation of the velocity signals, it was chosen to erase them. Today techniques do not allow clearing this kind of noise; therefore, the signals have to be discarded and reacquired. Unfortunately, after the reacquisition process, several missed points were still present because of the bed of complex geometries and could not be replaced (Figure 3.16 (a)).

## 3.8 Experimental campaign

The experimental campaign consisted of three long-duration tests. Each test referred to a different bed sediment (pebbles, coarse gravel and medium gravel); the median diameters are in table 3.1.

The number of 25 velocity profiles was chosen owing to the fact that the average velocity computed at a given elevation for all the longitudinal positions became constant (according to the equation 3.5) when more than 20 profiles were considered, whereas it varied for a lesser number.

$$\sum_{0}^{i} \bar{u}_i = \sum_{0}^{i+1} \bar{u}_i \tag{3.5}$$

where $i$ is the $i^{th}$ measurement in $x$ direction at a certain z. Hence, the measurement grid supported by a "real-time" analysis guaranteed a statistical convergence of the different mean quantities [41].

Table 3.4 reports the main hydraulic parameters of the experiments, $S$ being the flume slope, $B$ the flume breadth, $Q$ the water discharge, $h_w$ the water depth measured above the maximum grain crest level, $\Delta$ the relative submergence computed as $\Delta = h_w/\Delta_R$, $Re$ the Reynolds number and $Fr$ the Froude number.

| Parameter | Test 1.1 | Test 1.2 | Test 1.3 |
|---|---|---|---|
| $S$ (%) | 0.04 | 0.04 | 0.03 |
| $B$ (m) | 1.00 | 1.00 | 1.00 |
| $Q$ (l/s) | 46.5 | 57.2 | 57.8 |
| $h_w$ (m) | 0.185 | 0.175 | 0.187 |
| $\Delta$ | 3.13 | 6.58 | 10.07 |
| $Re$ | 46500 | 57200 | 57800 |
| $Fr$ | 0.19 | 0.25 | 0.23 |

**Table 3.4:** Flow details and hydraulics dimensionless numbers.

Table 3.4 shows that tests were designed in order to explore how the relative submergence can act on turbulent quantities. According to the following flow type classification proposed by Nikora et al. [107]:

- type 1, or high relative submergence flow, for $h_w >> \Delta$;
- type 2, or intermediate relative submergence flow, for $\delta_t < h_w < (2 \div 5)\Delta$, $\delta_t$ being the thickness of the boundary between the logarithmic and linear flow regions;
- type 3, or low relative submergence flow, for $h_w < \delta_t$.

Dingman [42] asserts that, in turbulent flows, eddies preclude the existence of strictly steady or uniform flow. Therefore, it is necessary to modify the definition of "steady" and "uniform" using average quantities, namely time-averaged over a period longer than the time-scale of turbulent fluctuations and space-averaged over a cross-section. Then, uniform flow is given by

**Figure 3.17:** Piezometers equipment used to measure the water surface slope.

$d\bar{u}/dx = 0$ at any instant. As stated by Chow [22]: "Theoretically speaking, the varied depth at each end approaches the uniform depth in the middle asymptotically and gradually. For practical purposes, however, the depth can be considered constant (and the flow uniform) if the variation in depth is within a certain margin, say, 1%, of the average uniform-flow depth."

The water surface slope $S_w$ within the test section was computed as the difference between the upstream water level and the downstream water level divided by $L_p$. Afterward, $S_w$ was compared to the flume slope $S$. The hydraulic conditions (discharge, flume slope, water depth) were varied until the condition $S_w = S$ was satisfied. According to Dingman [42] and Chow [22], in all tests the "steady-uniform" flow condition was carefully checked

in the test section by using two piezometers (see Figure 3.17). They were placed 5 cm before and after the test section at a mutual distance of $L_p = 2.6$ m. The piezometers were equipped with an electronic Vernier point gauge with an accuracy of 0.1 mm.

# Chapter 4

# Bulk statistics

*"Mechanical progress there is apparently no end:*
*for as in the past so in the future, each step in any direction will remove limits*
*and bring in past barriers which have till then blocked the way in other directions;*
*and so what for the time may appear to be a visible or practical limit will turn out*
*to be but a bend in the road."*
*Osborne Reynolds*

The chapter describes the results of Acoustic Doppler Velocimeter measurements made in a streamwise-wall-normal plane along the channel centerline. The aim of this chapter is twofold. First, a more rigorous analysis of the flow uniformity is shown and a further investigation on the distributions of spatially-averaged bulk velocity statistics is proposed. Evidence will be provided that momentum balance (as predicted through the DA Navier-Stokes) equation is respected along the streamwise direction; confidence will be also furnished about the quality of ADV data. Second, the validity of two classical paradigms of wall turbulence, namely the existence of a universal velocity

profile and the outer layer similarity hypothesis formulated by Townsend, will be investigated.

## 4.1 Momentum balance

In Figures 4.1 an overview is provided of the Reynolds stress along $\hat{z}$, with the relative form-induced and viscous stresses.

For a steady and uniform flow over a rough bed, the DA total shear stress $\langle\bar{\tau}\rangle$ (see Eq. 2.42 ), coming from the DANS equations [58, 107], is rewritten here as follows

$$\langle\bar{\tau}\rangle = -\rho\langle\tilde{u}\tilde{w}\rangle - \rho\langle\overline{u'w'}\rangle + \rho\nu\frac{d\langle\overline{u}\rangle}{dz} \tag{4.1}$$

where $-\rho\langle\tilde{u}\tilde{w}\rangle$ is the form-induced shear stress, $-\rho\left\langle\overline{u'w'}\right\rangle$ the DA Reynolds shear stress and $\rho\nu\, d\langle\overline{u}\rangle/d\hat{z}$ the DA viscous shear stress. In turbulent flows, the viscous shear stress in Eq. 4.1 is negligible across the flow depth.

Above the roughness layer, $-\rho\left\langle\overline{u'w'}\right\rangle$ dominates over $-\rho\langle\tilde{u}\tilde{w}\rangle$. The latter is not negligible only within the roughness sublayer, namely just above and below the roughness tops, i.e. for $\hat{z} < 0.1$ in tests 1.1 and 1.2, and for $\hat{z} < 0$ in test 1.3. In Eq. 4.1, all the shear stresses can be made non-dimensional dividing by $\rho u_*^2$ and expressed as a function of the non-dimensional vertical distance $\hat{z}$.

It is obvious that above the crests the main contribution to the DA total shear stress comes from the DA turbulent shear stress $-\rho\left\langle\overline{u'w'}\right\rangle$, as suggested for flows over rough beds by many authors [89, 145, 85]. In fact, the total shear stress expressed by Eq. 4.1 is tantamount to the turbulent shear stress above the grain crests, where the maximum shear stress is recorded.

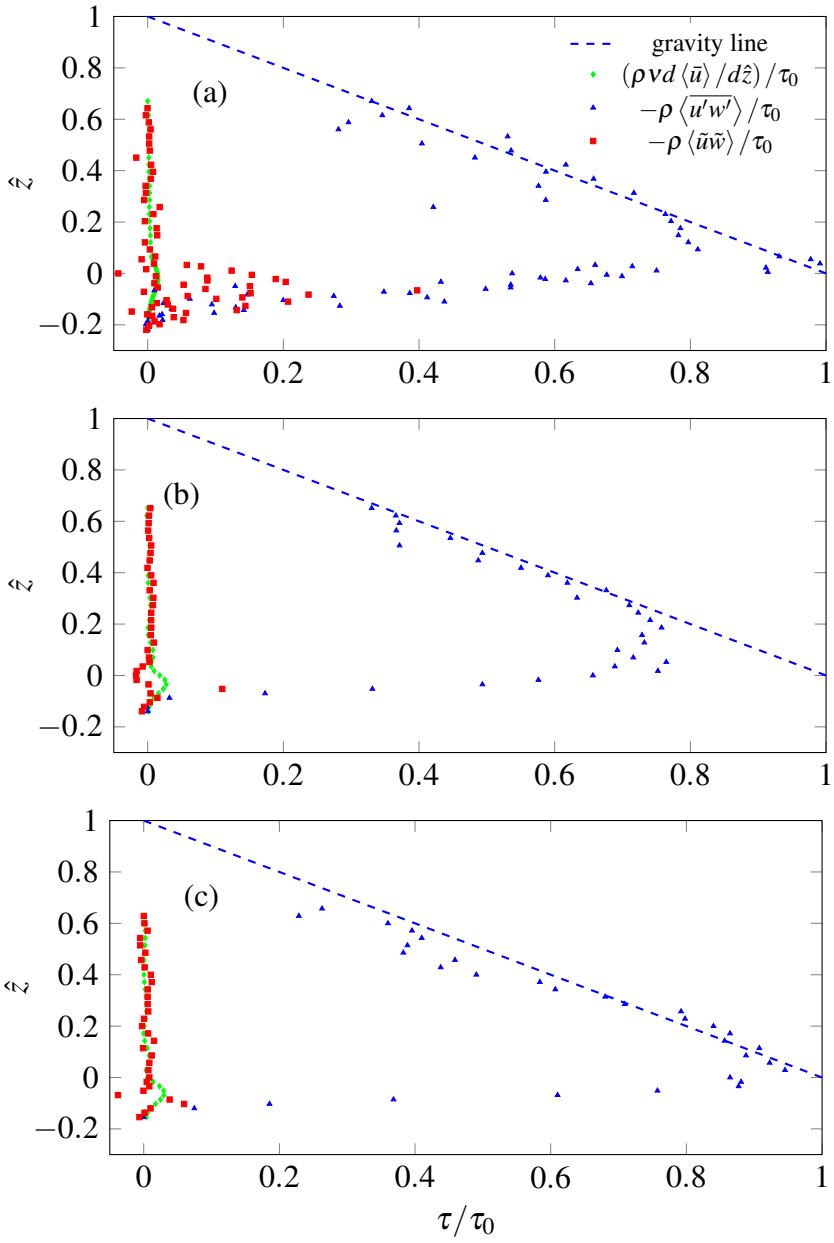


**Figure 4.1:** Shear stress in Test 1.1 (a); Test 1.2 (b) and Test 1.3 (c). ▲ represent the turbulent shear stress (Reynolds stress), ■ the form-induced stress, ● green circles the viscous shear stress and – – – is the gravity line.

The $-\left\langle \overline{u'w'} \right\rangle / u_*^2$ attains a peak close to the crest level $\hat{z} \approx 0$ and shows a sharp damping within the interfacial sublayer ($\hat{z} < 0.1$ in tests 1.1 and 1.2, whereas this elevation decreases down to $\hat{z} < 0$ in test 1.3). This behavior is clearly visible in Figure 4.1 (a) and in a gradually decreasing way in Figures 4.1 (b) and (c). In the interfacial sublayer, the DARSS $-\left\langle \overline{u'w'} \right\rangle / u_*^2$ is compensated by the FISS $-\langle \tilde{u}\tilde{w} \rangle / u_*^2$ (Figure 4.1). The FISS $-\langle \tilde{u}\tilde{w} \rangle / u_*^2$, which has a threshold point slightly above the maximum crest level, increases within the form-induced sublayer up to $\hat{z} = 0.1$ and then diminishes as $\hat{z}$ further decreases, approaching the maximum value among the roughness elements. While in Figure 4.1 (a) the FISS $-\langle \tilde{u}\tilde{w} \rangle / u_*^2$ contributes up to $\approx 30\%$ to the total shear stress, in Figures 4.1 (b) and (c) this contribution diminishes, according to the roughness $\Delta$ decrement; this result supports the work of Giménez-Curto and Lera [58], Manes et al. [90]. It may be pointed out that the $\rho \nu \, d\langle \overline{u} \rangle / d\hat{z}$ and $-\rho \langle \tilde{u}\tilde{w} \rangle$ are negligible above the roughness layer. Thus, the $-\left\langle \overline{u'w'} \right\rangle / u_*^2$ is the governing shear stress across the main flow layer [107, 98, 40].

### 4.1.1 Shear velocity

The shear velocity, $u_*$, is a basic parameter in order to scale the turbulence statistics. Unfortunately, over rough bed flows, inconsistency remains in its definition [112].

The well-known Clauser [23] method is commonly used to determine the shear velocity, by using the least-squares fitting of the measured time-averaged velocity distribution, assuming a universal logarithmic form. The log-law existence is, in turn, linked to the so-called overlap layer, which should appear somewhere across the water column [107]. Moreover, according to Nikora et al. [107], in the low and intermediate relative submergence the log-law distribution is not verified *a priori*. The Townsend [135] hypothesis asserts

that the overlap layer appears when the wall distance is the only relevant length scale influencing the flow. This means that there is need of more sophisticated analysis to establish the presence of the log-law distribution. Consequently, the Clauser chart method is not considered here.

Turbulent stress along $\hat{z}$ follows satisfactorily the gravity line computed as $\sqrt{\tau_{uw}/\rho} = u_*/(1-\hat{z})$ according to the hypothesis of steady and uniform flow. The sum of the three shear stress contributions reported in Eq. 4.1 is roughly linear above $\hat{z} \approx 0.1$ in each test, whereas beneath this elevation it becomes difficult to calculate accurately all the contributions to the shear stress. Hence, the linear trend of $\tau_{uw}$ up to $\hat{z} \approx 0.1$ can be exploited to extrapolate the correct value of shear stress at the reference bed level.

A new uncertainty arises from the choice of the reference bed level at which the bed shear stress can be extrapolated. This level can be set as the position obtained by considering of the so-called zero-plane displacement (ZPD) [78, 109], in the hypothesis of the occurrence of the log-law velocity distribution. The ZPD definition is a debated issue, since the low value of the relative submergence in the present tests would exclude the occurrence of the log-law velocity distribution. Moreover, Pokrajac et al. [112] suggested that the choice of the ZPD to define the reference bed level can lead to data misinterpretation. Pokrajac et al. [112] argued that the reference bed level can be set up at the crest level, providing an appropriate velocity scale.

Once confident that the total shear stress follows a linear trend, the bed shear stress can be extrapolated from the linear total shear stress profile, from the water surface to the bed reference level, which is fixed at the maximum crest level following the procedure by Manes et al. [90].

Table 4.1 compares the values of shear stress and shear velocity computed using the bed slope and the water depth ($u_{h_W} = \sqrt{\tau_0/\rho} = \sqrt{g h_w S}$), by using

the hydraulics radius ($u_R = \sqrt{\tau_R/\rho} = \sqrt{gRS}$), and the turbulent shear stress value extrapolated from the experimental data-set at $\hat{z} = 0$ ($u_* = \sqrt{\tau_0/\rho}$).

| | *Test* 1.1 | *Test* 1.2 | *Test* 1.3 |
|---|---|---|---|
| $\tau_R$ (Pa) | 0.5297 | 0.5085 | 0.5338 |
| $\tau_{h_w}$ (Pa) | 0.7256 | 0.6864 | 0.7335 |
| $\tau_0$ (Pa) | 0.5723 | 0.5988 | 0.5412 |
| $u_R$ (m/s) | 0.0230 | 0.0225 | 0.0231 |
| $u_{h_w}$ (m/s) | 0.0269 | 0.0262 | 0.0271 |
| $u_*$ (m/s) | 0.0239 | 0.0245 | 0.0233 |
| $Re_*$ (-) | 1211.7 | 639.5 | 433.4 |

**Table 4.1:** Bed-shear stress, shear velocity and shear Reynolds number in tests 1.1, 1.2 and 1.3.

Given the difficulties to compare the water surface slope with the granular bed slope (owing to the bed irregularities), the steady and uniform flow hypothesis was verified through the condition $\tau_R < \tau_0 < \tau_{h_w}$, which guaranties a good measurement accuracy and the applicability of the uniform flow equations [145]. In addition, the previous analysis provides confidence about the reliability of the ADV measurements, which respect the momentum balance across the flow depth, where the turbulent shear stress is the dominant one with respect to the sum of all the contributions.

## 4.2 Mean velocity profiles

The logarithmic velocity profile seems to be a feature of turbulent wall flows over rough walls, provided that the relative submergence is high enough. Manes et al. [90] assert that, using $u_*$ as a unique velocity scale, even at low relative submergence (i.e., in a condition in which the universal log-law does not occur) the option of a fictitious bed level (like that obtained with the ZPD) has to be avoided, since it does not provide a universal velocity scale. Hence,

the value of the shear velocity in Table 4.1 is considered reliable to scale the streamwise velocity distributions.

Despite Jiménez and del Alamo [71] indication on the logarithmic law application in lower relative submergence (see section 2.4.1), many efforts were made by the researcher in order to fit the universal log-law in these flow conditions. In particular, in rough-wall flows the log-law of the wall is determined by the von Kaŕmań constant, the ZPD, the roughness length and the friction velocity. The latter is provided by interpolating the shear stress profiles, as done in the previous section; the other three flow characteristics can be found by only interpolating experimental data, although this leads to a problem of overfitting. To overcome this issue, Nikora et al. [109] defined a ZPD ($d$), which can be determined from velocity measurements only, removing the hypothesis of a fixed value of the von Kaŕmań constant. Precisely, a linear region in the distribution of $dz/d\langle\bar{u}\rangle$ should be present to corroborate the existence of a logarithmic layer. The procedure proposed in Nikora et al. [109] and recalled in Koll [78] can be summarized as follows.

Over rough beds, the water column can be divided into three layers: the outer layer, the wall region and the subsurface layer. Furthermore, the wall region can be subdivided into the logarithmic layer and the roughness layer, with the top of the logarithmic layer at the 20% of the flow depth above the roughness layer [78]. In order to investigate the parameters of the vertical velocity profile, Koll [78] used the following equation

$$\frac{\langle\bar{u}\rangle}{u_*} = \frac{1}{\kappa}\ln\left(\frac{z-d}{z_r-d}\right) + \frac{u_r}{u_*} \tag{4.2}$$

where $\langle\bar{u}\rangle$ is the DA local velocity, $\kappa$ the von Kaŕmań constant, $d$ the ZPD, $z_r$ the upper bound of the roughness layer and $u_r$ the velocity at the elevation $z_r$.

The parameters involved in the above method can be computed directly by the streamwise velocity component through a linear and a logarithmic regression analysis in the roughness and logarithmic layer, respectively, as widely explained in Nikora et al. [109] and Koll [78]. The only exception is given by $u_*$, which is assessed as illustrated in the previous section.

Hence, following Koll [78], the ZPD and the von Kaŕmań $\kappa$ were obtained and summarized in Table 4.2. Table 4.2 shows that the von Kaŕmań $\kappa$ is a

| | *Test* 1.1 | *Test* 1.2 | *Test* 1.3 |
|---|---|---|---|
| $z(d)$ (-) | -0.049 | -0.040 | -0.032 |
| $\kappa$ (-) | 0.35 | 0.35 | 0.41 |

**Table 4.2:** zero plane displacement and von Kaŕmań constant in tests 1.1, 1.2 and 1.3.

function of the relative submergence for both data presented herein and taken from the literature. Specifically, at increasing $\Delta$, $\kappa$ approaches the classical value of 0.41. In Figure 4.2, the results of tests 1.1, 1.2 and 1.3 (red open circles) were compared with those presented in Koll [78], where the $\kappa$ versus $\Delta$ plot shows a good agreement ($h_d/\Delta$ is the relative submergence in Figure 4.2) .

Finally, the velocity fitting, which was obtained by using the procedure illustrated before, are shown in Figure 4.3.

To have a complete view, the velocity profiles in inner coordinates are plotted in Figure 4.4. As expected, the velocity profiles do not collapse on a single curve, suggesting that roughness governed the entire flow depth in the three tests.

Ultimately, considering that there are not enough elements to speculate on the log-law velocity distribution, a further analysis is required to dispel the remaining doubts on the existence of a log-law velocity distribution.

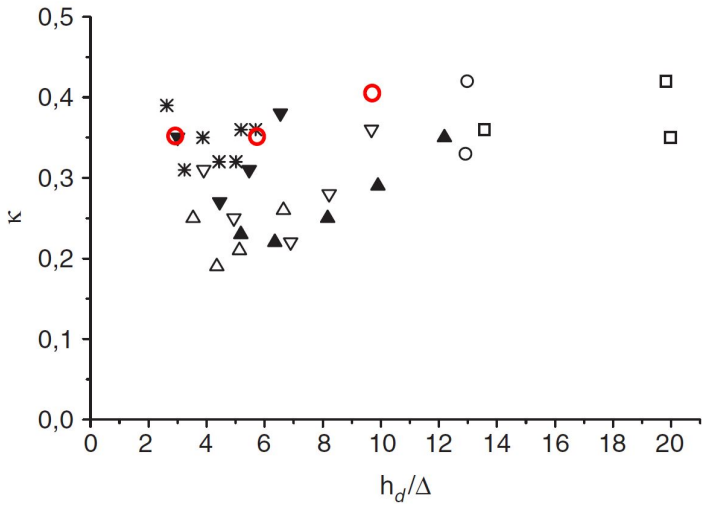


**Figure 4.2:** Relation between the constant of proportionality $\kappa$ and relative submergence $h_d/\Delta$; black and white symbols are those presented in Koll [78] in which open circles are related to beads roughness elements, square for cubes roughness elements, triangles are related to gravel bed, stars symbol for armour layer and open red circles are related to tests 1.1, 1.2 and 1.3.

In OCFs over rough beds, the shear production corresponds to the mean TKE, as stated by Ferreira et al. [46]. If the relative submergence is high enough, a local equilibrium between TKE production and dissipation is expected sufficiently far from the roughness elements.

Ferreira et al. [46] continues saying that: "in an open-channel flows over hydraulically rough beds with large enough relative submergence for which wall similarity holds [135], the longitudinal velocity profile above the roughness-influenced layer can be fitted to a logarithmic profile. For low submergence flows, considerable debate has taken place relatively to the parameters most affected by the higher relative protrusion of the roughness elements [43, 110, 51]".

In the literature few experiments are present having intermediate relative submergence with a high spatial variability, as in the present tests. In tests

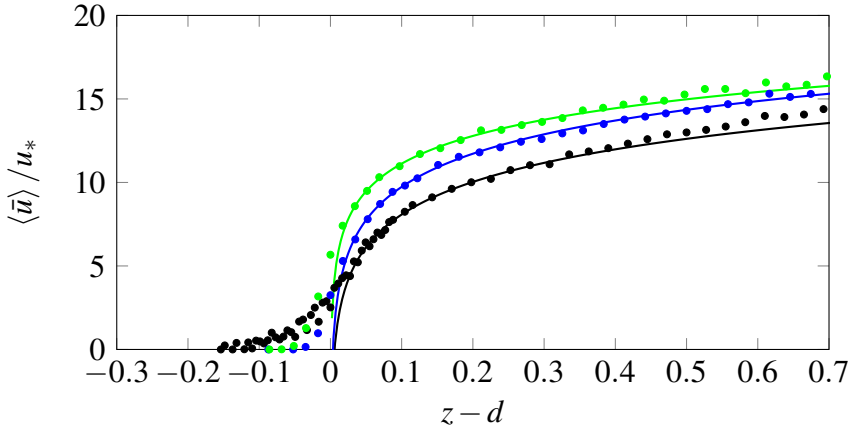


**Figure 4.3:** Velocity profiles fitted using the Koll [78] procedure. Test 1.1 (●), test 1.2 (●) and test 1.3 (●)

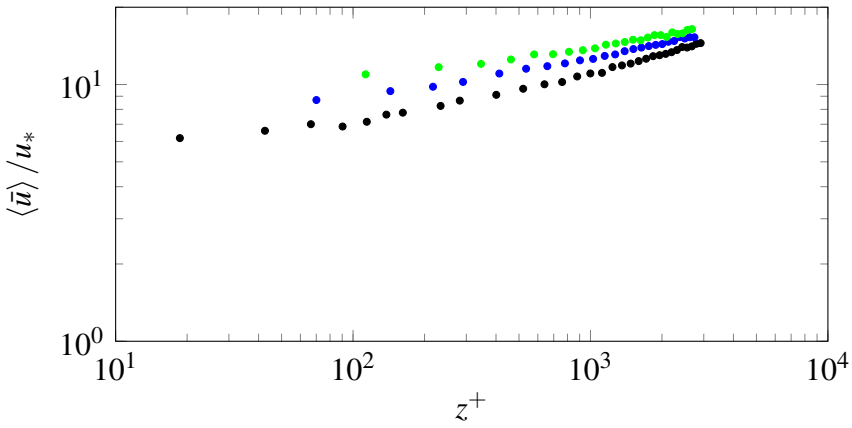


**Figure 4.4:** Velocity profiles in inner coordinates ($z^+ = zu_*/\nu$) in test 1.1 (●), test 1.2 (●) and test 1.3 (●).

with not high relative submergence, no equilibrium layer is expected. In order to verify this, an analysis based on the third-order moment equilibrium was performed. The log-law can be present only in the so-called overlap layer, in which the vertical turbulent transport term assumes a constant trend [106]. The vertical turbulent transport is defined as

$$\left\langle \overline{TKE} \right\rangle_w = \left\langle \overline{u'u'w'} \right\rangle + \left\langle \overline{v'v'w'} \right\rangle + \left\langle \overline{w'w'w'} \right\rangle . \tag{4.3}$$

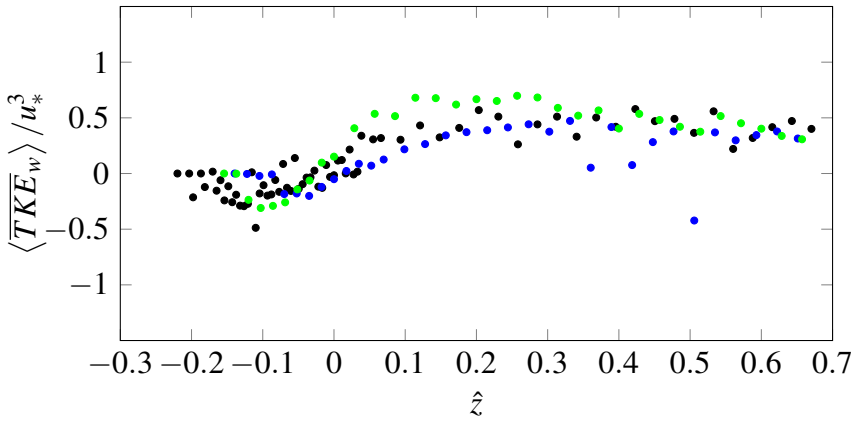


**Figure 4.5:** Vertical turbulent transport, in test 1.1 (●), test 1.2 (●) and test 1.3 (●).

Figure 4.5 shows that $\left\langle \overline{TKE}_w \right\rangle / u_*^3$ attain their peaks at $\hat{z} \approx 0.3$ above the grain crests having a magnitude between 0.4 and 0.65, which are in agreement with results of Hurther et al. [68]. The vertical TKE flux approaches the zero value at the crest level and becomes negative inside the roughness gaps, indicating a change in the direction of energy transfer.

Figure 4.5 shows that a clear plateau was evident only in test 1.3, i.e. in the run with the highest submergence, thus confirming that a log-law can be observed only when the scale separation between outer and inner variables is sufficiently high. According to Townsend [135] for highly rough flow, the

log-layer lower bound should appear at $z = 5 \times \Delta_R$. These results refine the observations drawn from the von Kaŕmań constant analysis shown in Figure 4.2. It seems that test 1.3 showed a logarithmic layer, whereas tests 1.1 and 1.2 definitely did not.

In fact, following Townsend [135], the only experiment supported by the third-order moment analysis is test 1.3, in which the log-law can occur and the von Kaŕmań $\kappa$ assumes the universal value (0.41).

## 4.3 Outer layer similarity hypothesis

In the following sections, the second-order velocity statistics are used to test the outer layer similarity. In particular, the streamwise and vertical turbulent intensities are employed to this purpose.

### 4.3.1 Turbulent intensity

Figure 4.6 and Figure 4.7 show the spatial average turbulence intensity in streamwise and vertical direction, respectively.

All the profiles collapse fairly well above $\hat{z} = 0.2$. Regarding Figure 4.6, a greater scattering is observable as the grain crests are approached, where the spatial average turbulence intensity distributions reach a magnitude contained in the range from 2.5 to 3 at an elevation between $(-0.05 \div 0.05)\ \hat{z}$. These peak magnitudes are in line with those reported in Nezu and Nakagawa [102]. The peak elevation of $\langle \bar{\sigma}_u \rangle$ over a rough bed shows disagreement with respect to literature results; e.g., Wang et al. [142] found the peak at $\sim 0.1 h_w$ above the crests in gravel-bed OCFs at a relative submergence of $0.64 \div 6$. On the other hand, Mignot et al. [98] showed a peak below the crests for gravel-bed OCFs, whereas a simulation by Singh et al. [128] over a rough-bed made

of spheres with $\Delta = 4$ showed a peak of the streamwise turbulence intensity at the crests level. The peaks in 4.6 contains all these cases; in particular, a dependence on relative submergence was observed. Namely, the smallest $\Delta$ (test 1.1) showed a peak at $\hat{z} \sim 0.05$, whereas intermediate $\Delta$ (test 1.2) presented a peak at the crest level and higher $\Delta$ (test 1.3) put in evidence a peak placed below the crest level.

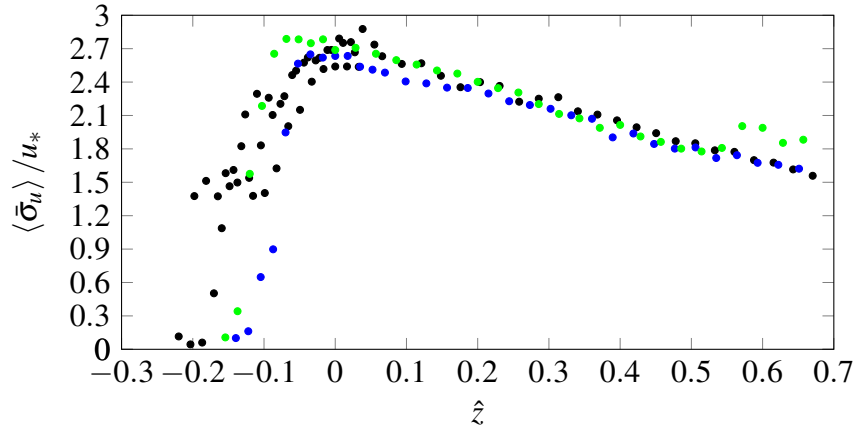


**Figure 4.6:** Streamwise turbulent intensities vs $\hat{z}$. Test 1.1 (•), test 1.2 (•) and test 1.3 (•).

Finally, the vertical turbulence intensities are shown in Figure 4.7. According to Manes et al. [90] and Singh et al. [128] these profiles do not show a clear peak; they evidenced that the distribution reached maximum values from 0.8 to 1.0. Once again, a good collapse is visible above $\hat{z} = 0.2$.

Hence, according to the literature [90, 90, 89], both $\langle \bar{\sigma}_u \rangle / u_*$ and $\langle \bar{\sigma}_w \rangle / u_*$ showed a linear trend, whereas $\langle \bar{\sigma}_u \rangle / u_*$ collapsed on a single curve above $\hat{z} = 0.2$ (which is typical of OCFs on rough beds) and $\langle \bar{\sigma}_w \rangle / u_*$ seemed to be influenced by the complex bed roughness geometry and the water surface fluctuations, showing a fair collapse in the range $0.2 < \hat{z} < 0.5$.

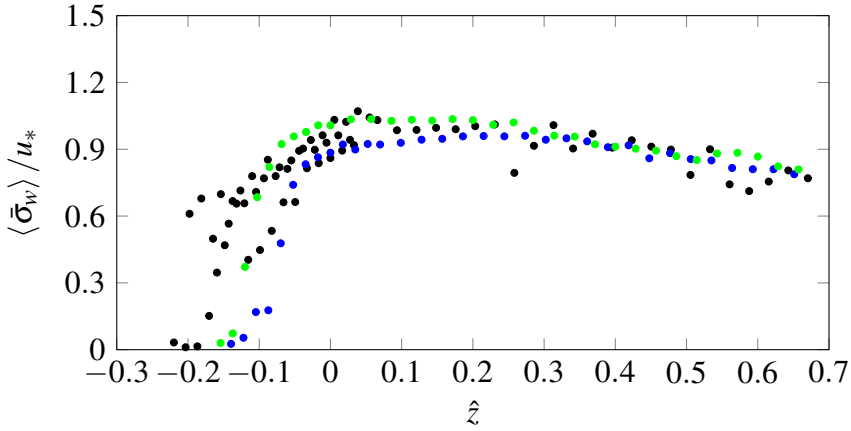


**Figure 4.7:** Vertical turbulent intensities vs $\hat{z}$. Test 1.1 (●), test 1.2 (●) and test 1.3 (●).

Hence, second-order statistics for all the tests seemed to collapse on a curve when plotted in outer-layer coordinates. This fact means that, despite the low submergence characterizing the three tests, the outer layer similarity hypothesis was respected, in line with the results of Schultz and Flack [124] for turbulent boundary layers and Manes et al. [90] for turbulent OCFs on rough beds.

# Chapter 5

# Large scales in OCFs and influence of relative submergence

*"See now the power of truth; the same experiment which at first glance seemed to show one thing, when more carefully examined, assures us of the contrary."*
*Galileo Galilei*

This chapter addresses turbulence-scaling in OCFs using a range of statistical methods, including auto-correlation functions, third-order structure functions and spectral methods. These techniques are used for two purposes: (i) investigating the existence and scaling of LS eddies; and (ii) verify the scaling of small scale turbulence and the existence of the so-called inertial sub-range for different relative submergence conditions and elevations above the bed. Before discussing the main core of the analysis, a relatively in-depth check of the Taylor hypothesis of frozen turbulence is presented to cast the discussion of results within a spatial framework of analysis, which, with respect to its temporal counterpart, is more intuitive and clearer.

## 5.1 Validity of the Taylor frozen-in hypothesis

The Taylor hypothesis [133] states that, at a measurement point, the flow field sensed by a hypothetical probe advects downstream without significant distortion (namely, the velocity fluctuations evolve slowly as compared to the mean velocity). When this condition is satisfied, it is possible to switch from the temporal to the spatial domain of analysis by multiplying time-scales by the local time-averaged velocity. Within the context of spectral analysis, if the Taylor hypothesis is respected, it is possible to switch from frequency to wave-number domain simply dividing the frequencies by the mean local velocity.

The condition, which should be verified in order to respect the classic Taylor frozen-in hypothesis, is

$$\langle \bar{\sigma}_u \rangle \ll \langle \bar{u} \rangle \tag{5.1}$$

where $\langle \bar{\sigma}_u \rangle$ is the DA standard deviation of the velocity fluctuations and $\langle \bar{u} \rangle$ is the local DA velocity. The DA method can be applied in order to obtain local statistics that are a function of the elevation only. This applies especially for flow regions in proximity of the rough-bed where the time-averaged flow is highly heterogeneous. Figure 5.1 shows that the condition $\langle \bar{\sigma}_u \rangle / \langle \bar{u} \rangle$ approaches unity only in proximity of the roughness tops where the Taylor hypothesis is therefore violated.

A more stringent condition for the Taylor hypothesis validity is provided by the work of Matthaeus and Goldstein [94]. According to these authors it is possible to carry out a more rigorous check of the Taylor hypothesis by comparing the advection time-scale of large eddies and a characteristic

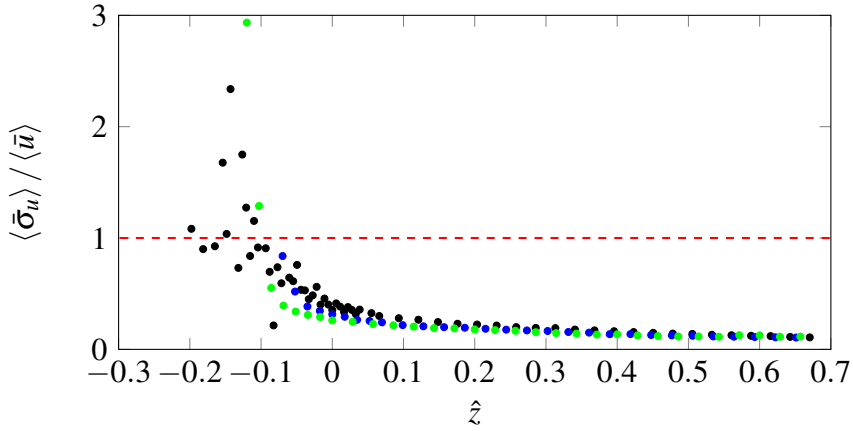


**Figure 5.1:** Classic Taylor violation along $\hat{z}$; • represent the test 1.1, • test 1.2 and • test 1.3.

nonlinear time-scale. The former is given by

$$\tau_{\langle \bar{u} \rangle}(k_x) = \frac{\lambda}{\langle \bar{u} \rangle} = \frac{2\pi}{k_x \langle \bar{u} \rangle}. \tag{5.2}$$

This time should be always smaller than the characteristic nonlinear time

$$\tau_{nl}(k_x) = \frac{1}{k_x \sqrt{k_x \langle \Phi_{uu}(k_x) \rangle}}. \tag{5.3}$$

where $\langle \Phi_{uu}(k_x) \rangle$ is the spectrum and $k_x \langle \Phi_{uu}(k_x) \rangle$ is its premultiplied form. Equation 5.3 can be viewed as the typical eddy time distortion. The Taylor hypothesis is valid if $\tau_{\langle \bar{u} \rangle}(k_x) \ll \tau_{nl}(k_x)$. This condition can be lumped into a single scalar function [45] as

$$\psi(k_x) = \frac{2\pi \sqrt{k_x \langle \Phi_{uu}(k_x) \rangle}}{\langle \bar{u} \rangle} \ll 1 \tag{5.4}$$

The condition expressed by equation 5.4 is well summarized in figure 5.2, where the maximum value of $\psi(k_{max})$ is plotted as a function of $\hat{z}$. In

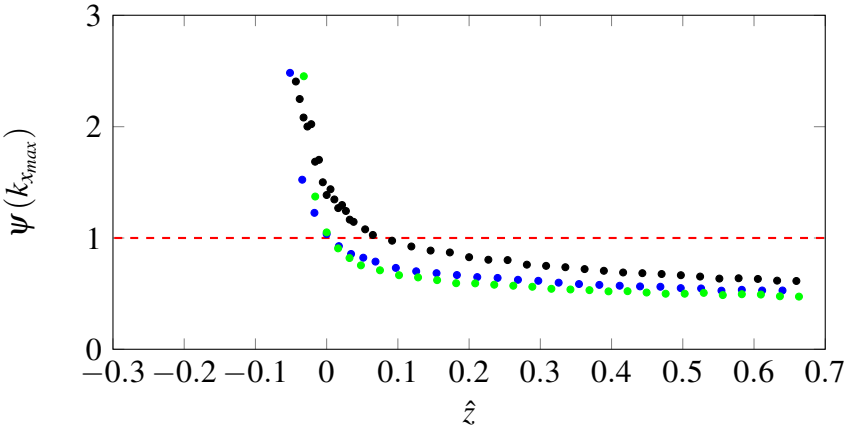


**Figure 5.2:** Taylor violation along $\hat{z}$;● represent test 1.1, ● test 1.2 and ● test 1.3.

figure 5.2 $k_{xmax}$ represents the wavenumber at which the maximum value of $\psi$ is obtained. As anticipated, comparing the results reported in Figure 5.1 and 5.2, it is clear that the method proposed by Matthaeus and Goldstein [94] is more restrictive. In fact, while in Figure 5.1 the Taylor hypothesis seems to be respected in all the tests even at the crest level, in Figure 5.2 $\psi(k_{max})$ approaches 1 at $\hat{z} = 0.1$ in test 1.1 and at $\hat{z} = 0$ in tests 1.2 and 1.3.

Hence, in the spirit of a conservative approach, the Taylor hypothesis can be considered satisfied for $\hat{z} > 0.1$.

## 5.2 Integral Length Scale

The auto-correlation function as expressed by equation 2.91 is here computed accounting for spatial heterogeneities and, consistently with the DAM, averaged over bed-parallel planes. The auto-correlation function 2.91 at a given

point **x** can be defined as

$$R(\mathbf{x},\tau) = \overline{u_i'(\mathbf{x},t)u_i'(\mathbf{x},t+\tau)}, \tag{5.5}$$

Note that the spatial dependence in the equation above is appropriate because, given the heterogeneity of the rough beds, the auto-correlation function depends slightly on the point where it is measured $\mathbf{x} = (x,\hat{z})$. Using the Taylor hypothesis, we can transform time lags into space increments, namely $r = |\overline{u}|\tau$ (where the time-averaged velocity is a function of $\hat{z}$). With the transformation $R(\mathbf{x},\tau) \rightarrow R(\mathbf{x},r)$, it is possible to define the integral length scale $\lambda_c$ as

$$\lambda_c(\mathbf{x},r) = \frac{1}{R(\mathbf{x},0)} \int_0^{r_{max}} R(\mathbf{x},r)dr. \tag{5.6}$$

where $r_{max}$ is the maximum space increment corresponding to a value of the auto-correlation function that is not significantly different from the noise-correlation value. Following the procedure suggested by Roy et al. [122], this noise value (i.e. $R_{lim}$) was estimated by correlating (with zero time-lag) two uncorrelated portions of the velocity time series. The results from this analysis showed that $R_{lim}$ is about $(1 \div 2)\ \sigma_u^2$. The integral length scale can be interpreted as a measure of the large-scale eddies in a turbulent flow. However, being an integral length scale, it represents only a "bulk" estimate.

Figure 5.3 shows the spatially-averaged integral length scale in streamwise direction $\langle\lambda_c\rangle$ normalized by the water depth $h_w$ versus $\hat{z}$. Here the spatial averaging provides two benefits: on one hand, it allows smoothing out spatial variations. On the other hand, it allows having more reliable estimates of the auto-correlation, which are computed over a large number of measurements at different points and hence result being associated with small confidence intervals. Although the linear increase in $\langle\lambda_c\rangle$ near the wall ($\hat{z} < 0.1$) is in line with the observation of Volino et al. [139] the determination of $\langle\lambda_c\rangle$ based

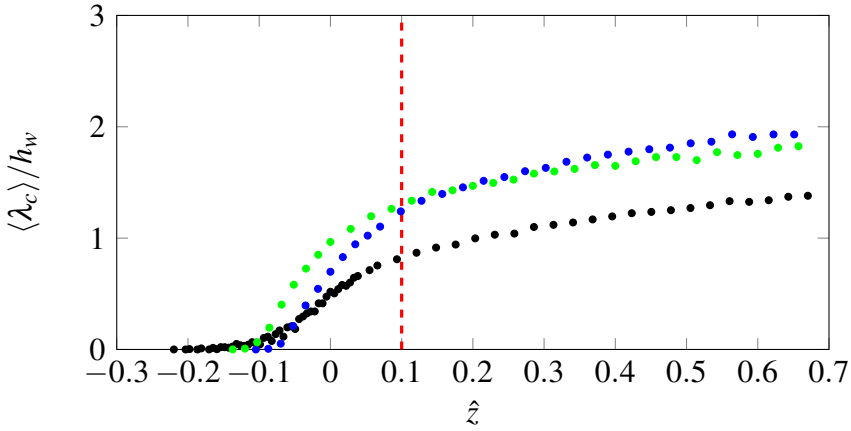


**Figure 5.3:** Energy containing scale $\langle\lambda_c\rangle/h_w$ versus $\hat{z}$ (● test 1.1, ● test 1.2 and ● test 1.3), – – – Taylor hypothesis edge.

on single point measurements (i.e. ADV measurements) requires the use of the Taylor hypothesis. Thus, according to the previous section, the results below the red-dashed line in Figure 5.3 are not considered. As expected, $\langle\lambda_c\rangle$ increases with $\hat{z}$ for all the experiments and in particular it has a weak steady growth across the water depth. More interestingly, it shows a strong dependency on the relative submergence $\Delta$. In particular the size of large-scale eddies in experiment 1.1 (i.e. the experiment with the lowest $\Delta$), seems to be significantly smaller than that of the large eddies in the other flow conditions.

This is in line with current paradigms suggested in the literature, as it seems that the larger the inner-outer scale separation (i.e., in this case, high relative submergence) the larger the size of energetic eddies [76, 52, 50]. This issue has been particularly investigated in smooth-wall flows, where it is commonly observed that LS eddies grow in size with increasing $Re_* = u_* h_w/\nu$ (where $\nu/u_*$ is the viscous length scale), which is effectively the ratio of outer and inner scales for smooth walls. For rough walls, the dependency of large-scale eddies on inner-outer scale separation (relative submergence)

has been only recently addressed by Cameron et al. [19], who found LSs size of the order of $\langle \lambda_c \rangle$.

A deeper analysis of LS eddies is provided in the following section through spectral analysis. In particular, spectra and co-spectra in premultiplied form are used to identify the scales of turbulence that contributes the most to TKE and to momentum transport. The next section, besides discussing large-scale eddies, provides also a general assessment of the existence of the inertial subrange, as defined by Kolmogorov, to identify spectral regions affected by experimental measurement noise, which is a crucial step to assess the reliability of the experimental measurements presented herein.

## 5.3 Spectral Analysis

The Welch method [13] with a weighting window was used to compute the frequency spectral densities from the velocity time series. Spectral densities were computed as follows: first auto-correlation functions $R(\mathbf{x},\tau) = \overline{u'(\mathbf{x},t+\tau)u'(\mathbf{x},t)}$ were calculated. Then, the Fourier transform of the above correlation function was tapered with a Hann window, which led to the spectral density $\Phi_{uu}(f,\mathbf{x}) \equiv \Phi_{uu}(f,x,\hat{z})$ in the frequency domain. As expected, spectra computed at different stream-wise locations $x$ and located at the same vertical elevation $\hat{z}$ were very similar, as they are associated with similar "footprints" (i.e., velocities measured at one point are the result of eddies advecting from upstream, that were generated by shear instabilities induced by an upstream portion of the rough bed, which, in turbulence jargon, is usually referred to as footprint). Hence, spectra that were estimated from measurements at the same vertical elevation were ensemble- (i.e., spatially-) averaged to improve the confidence interval associated with each spectral estimate $\langle \Phi_{uu} \rangle$.

In order to investigate the scales that mostly contribute to momentum transport, co-spectra were obtained from the cross-correlation function $R(\mathbf{x},\tau) = \overline{u'(\mathbf{x},t+\tau)w'(\mathbf{x},t)}$ and were spatially-averaged following an analogous procedure as described above for spectra.

Section 5.1 highlighted that the Taylor hypothesis can be applied fairly confidently for flow regions over 90% of the water depth. Here, for completeness, results from spectral analysis converted to the wavenumber domain are presented down to the elevation corresponding to the roughness tops (see analogous analyses in Dennis and Nickels [37], Cameron and Nikora [18], Ferraro et al. [45]), but they need obviously to be taken with caution as scales can be severely affected by the non-validity of the Taylor hypothesis.

Regarding Figure 5.4, it shows the spatial-averaged spectra $\langle\Phi_{uu}\rangle$ for several vertical distances $\hat{z}$ in tests 1.1, 1.2 and 1.3. A first comment is that the $k^{-5/3}$ slope is observed in all the spectra having different vertical elevation. We can say that the inertial subrange is well visible at the investigated *Re* numbers, showing a net scale separation, in which the inertial subrange is developed within a wavenumber range which is almost a logarithmic decade. At scales corresponding to $k_x h_w \sim 10$, a *bulge* is present. This bulge is also observed in the $\langle\Phi_{vv}\rangle$ spectra, but not in the $\langle\Phi_{ww}\rangle$ spectra. This fact suggests that its occurrence is related to the shape of the ADV sampling volume, (see Appendix A), which is characterized by a vertical length scale that is much smaller than the horizontal and lateral ones. Hence, the bulge is likely to be an instrument artefact associated with aliasing effects. Furthermore, within the range $k_x h_w > 2$, spectra become gradually affected by noise and hence are not reliable to infer the turbulence behavior.

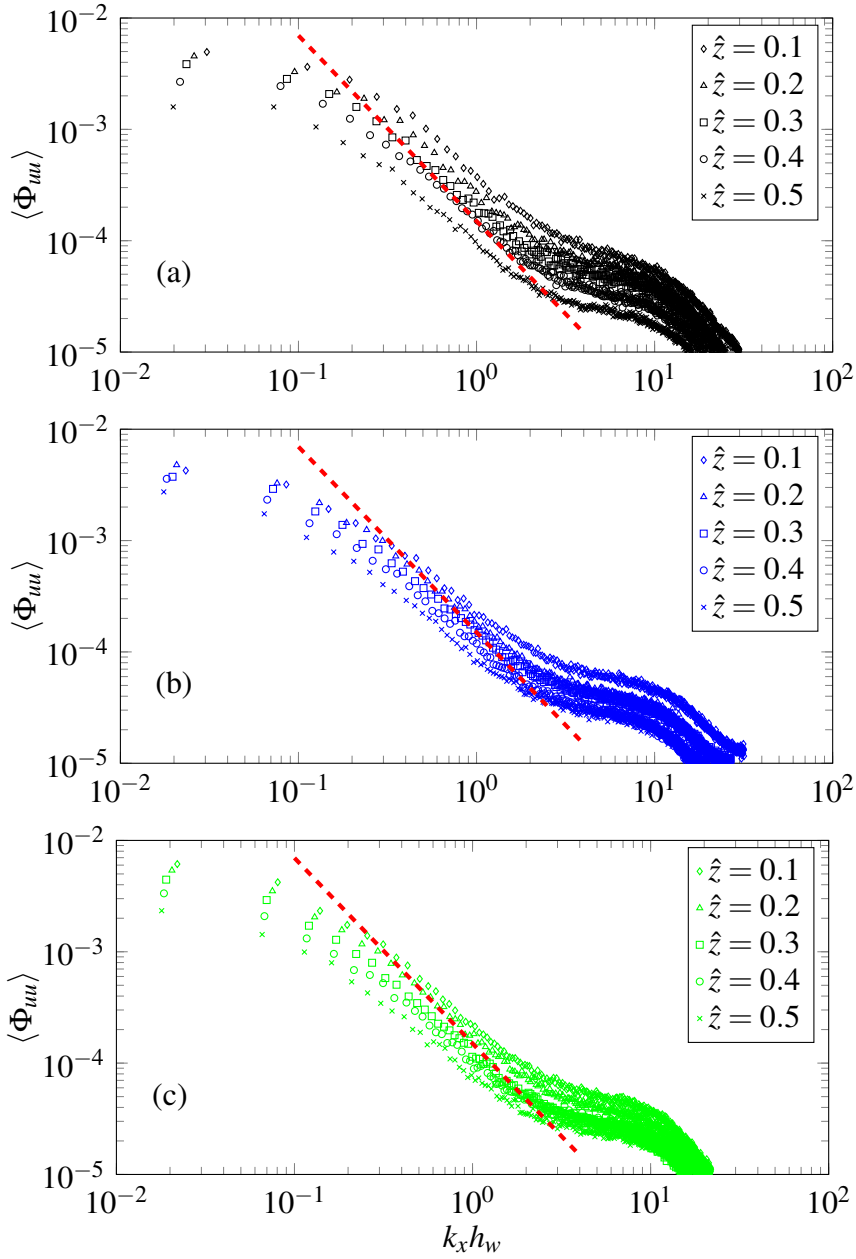


**Figure 5.4:** Spatial-averaged spectra $\langle \Phi_{uu} \rangle$ for several vertical distances $\hat{z}$. • represent test 1.1, • test 1.2, • test 1.3, – – – is the $k^{-5/3}$ slope.

### 5.3.1 The $4/5$ law of turbulence

The appearance of a $-5/3$ scaling region suggests for the occurrence of an inertial range within the Fourier space. In real space a more stringent way to check the existence of the Kolmogorov scaling is to consider the third-order structure functions [53].

According to Kolmogorov [79], within the inertial subrange, third-order longitudinal structure functions $D_u^3$ should follow equation 5.7. By plotting $\langle\varepsilon\rangle$ versus $r$ then, the appearance of a plateau indicates the existence of an inertial subrange and provides a way to estimate the TKE dissipation rate, as will be seen in the following [45].

One of the few exact theorems of turbulence is the Kolmogorov $4/5$-law, described by equation 2.76, which can be applied to locate the inertial subrange and to obtain the averaged TKE dissipation rate as

$$\langle\varepsilon\rangle = -\frac{5}{4r}\left\langle\overline{D_u^3}\right\rangle, \tag{5.7}$$

where $D_u = u(\mathbf{x}_*, x+r) - u(\mathbf{x}_*, x)$ is the space increment of the streamwise velocity. As usual, the overbar and the angle brackets identify time and spatial average, respectively. Equation 5.7 can be used to measure, in a reliable way, the TKE dissipation rate in any turbulent flow. The compensated Kolmogorov $4/5$-law, given by 5.7 for different vertical distances $\hat{z}$ in all the tests, is presented in Figures 5.5, where the horizontal dashed lines represent the fit of 5.7 in the inertial subrange.

Comparing Figures 5.5 and Figures 5.3, it is important to notice that the law is lost at scales comparable to the integral scale (or energy containing scale), as expected from the statistical theory of turbulence [53].

Figures 5.5 do display a plateau and, hence, suggest the occurrence of an inertial subrange as for the Kolmogorov theory. However, a word of

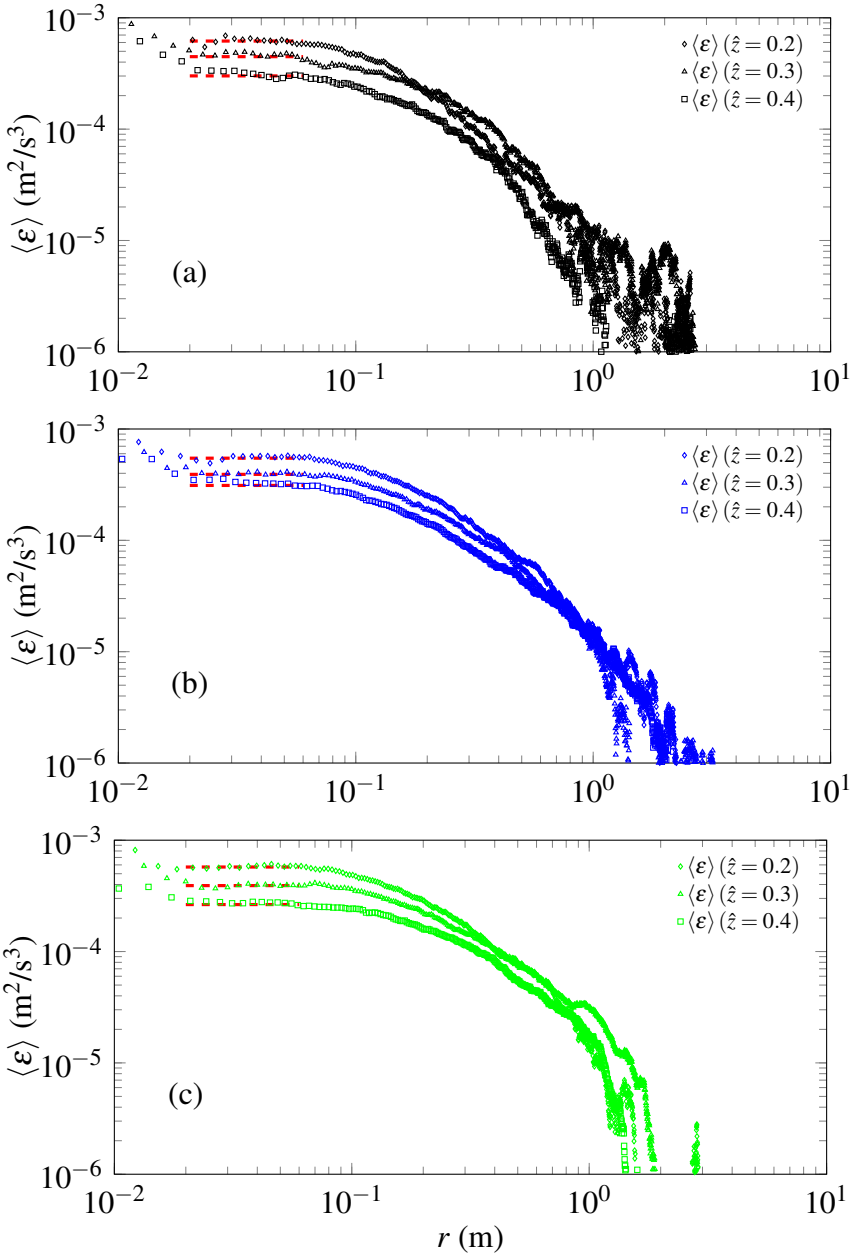


**Figure 5.5:** Compensated Kolmogorov $4/5$-law in natural-bed flow for different vertical distances showing the fit of 5.7 by the horizontal lines. Subfigure (a) refers to the test 1.1, (b) to 1.2 and (c) to 1.3.

caution is in order here. The corresponding plateaus in Figures 5.5 locate the inertial subrange observed in Figure 5.4 and the growth at $r < 0.01 \div 0.02$ corresponds to the wavenumber bulge already mentioned.

Note that, as reported in Ferraro et al. [45], the dissipation rate measured using the power spectrum as

$$\langle \varepsilon_\nu \rangle = 2\nu \int_0^\infty \left\langle k_x^2 \Phi_{uu} \right\rangle (k_x) dk, \tag{5.8}$$

can somewhat underestimate the realistic dissipation rate. That is, it converges only if the Kolmogorov scale is well-resolved, which is usually a difficult proposition in experiments [45]. Hence, the TKE dissipation rate estimated from the $4/5$ law is considered a more robust and precise method in order to measure the cascade intensity in laboratory experiments or natural-bed flows, such as in rivers.

Finally, the TKE dissipation rate computed from the $4/5$-law is shown in Figures 5.6 as a function of $\hat{z}$. The $\langle \varepsilon \rangle$ along $z$ shows a sort of similarity in all the tests (Figure 5.6).

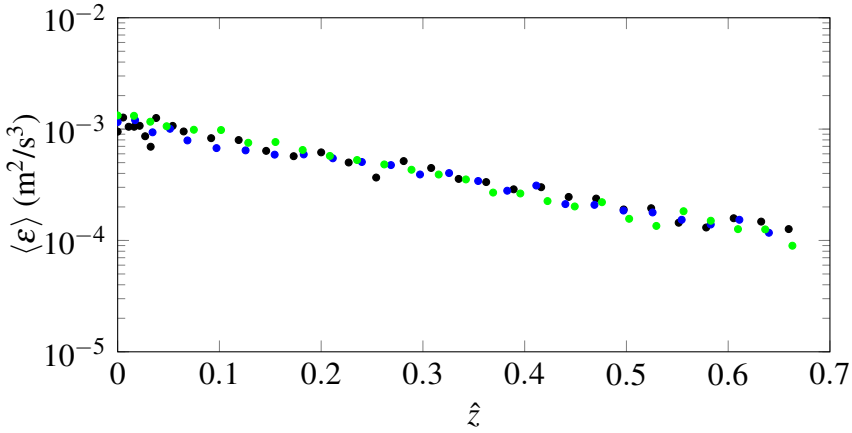


**Figure 5.6:** TKE dissipation rate $\langle \varepsilon \rangle$ as a function of $\hat{z}$.● test 1.1, ● test 1.2, ● test 1.3..

This should be expected, because all the experiments are characterized by similar friction velocities and zero-plane displacements (if applicable). In fact, assuming that within the overlap (i.e. logarithmic) layer TKE production and dissipation are balanced, the dissipation rate can be estimated as $\varepsilon = u_*^3/\kappa(z-d)$, which therefore should be roughly the same for all flow conditions as reported in Figure 5.6. Hence, it is concluded that the inertial sub-range identified by the third-order structure functions is not an artefact of measurements.

## 5.4 Premultiplied Spectra

In the literature pertaining to wall flows, 3-D velocity measurements are rare, as most studies report measurement of the longitudinal component and very few of the vertical one. This fact can provide an incomplete view of how turbulence structures contribute to TKE and momentum transport. This section attempts to fill this experimental gap by investigating relevant spectra and cospectra of all the three velocity components.

Premultiplied spectra provide a way to quantify the contribution of different eddy-scales to the TKE. Namely, peaks in the premultiplied spectra indicate wavelengths in which a significant amounts of energy resides.

Hence, the aim of this section is to exploit premultiplied spectra to identify the size of the large-scale eddies (which is identified as the wavelength where premultipled spectra show a peak) and how this depends on relative submergence.

Before proceeding with the analysis, a short preamble is needed. In Figure 5.7 the streamwise velocity spectra of test 1.1 is shown, in order to give some indications on how to interpret the plots. As expected, a clear peak at dimensionless wavenumbers that are compatible with LSs is clearly

visible, whereas the second peak at higher wavenumbers can be attributed to measurement noise associated with the sampling volume of the ADV probe across the longitudinal direction (see Appendix A). Hence, the dashed vertical red line constitutes a limit over the wave-number domain, beyond which the spectral analysis is not reliable.

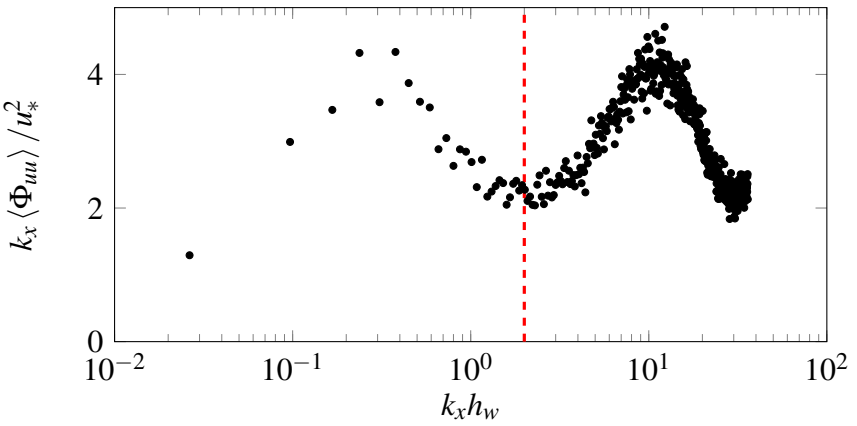


**Figure 5.7:** Spatial-averaged Premultiplied one-dimensional spectra $k_x\langle\Phi_{uu}\rangle$ at $\hat{z} = 0.2$, red dashed vertical line represents the ADV sampling volume wavelength

.

Figure 5.8 refers to the spanwise velocity spectra, which, according to the literature, should display a peak corresponding to LSs at about $k_x h_w \sim 1 \div 2$ [36, 134]. Unfortunately, the bulge peak also observed in $k_x \langle \Phi_{vv} \rangle$ disturbs the LS peak in figure 5.8.

Therefore, analysis of LS as inferred from spectra of the spanwise velocities will be omitted in this thesis.

As discussed in Appendix A, the ADV sampling volume is a cylinder of height significantly smaller than width. This implies that vertical velocity spectra $\langle \Phi_{ww} \rangle$ are less affected from noise than spectra of longitudinal and

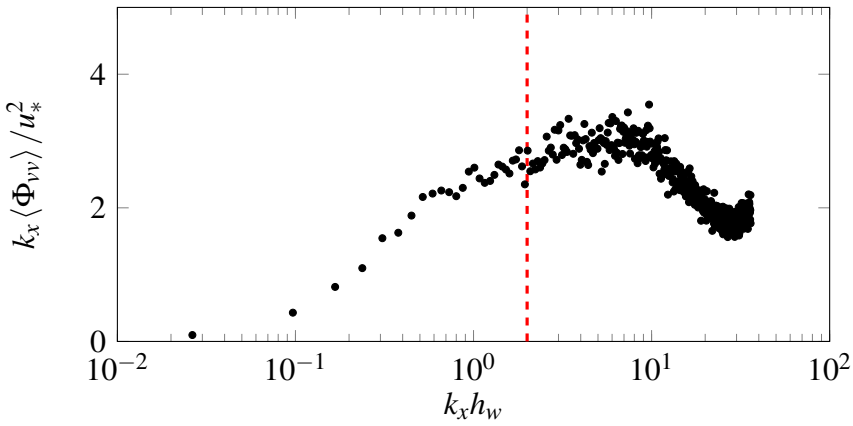


**Figure 5.8:** Spatial-averaged Premultiplied one-dimensional spectra $k_x\langle\Phi_{vv}\rangle$ at $\hat{z} = 0.2$, red dashed vertical line represents the sampling volume wavelength.

spanwise velocity components. Figure 5.9 indeed shows that vertical velocity spectra do not display the fictitious peak at high wavenumbers ranges.

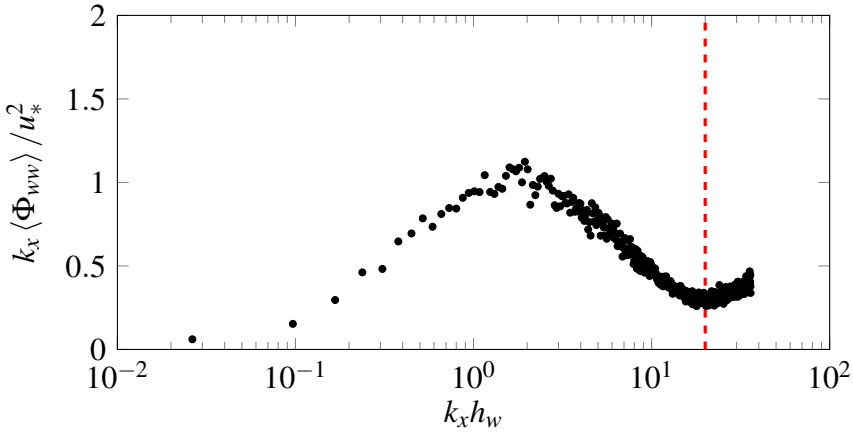


**Figure 5.9:** Spatial-averaged Premultiplied one-dimensional spectra $k_x\langle\Phi_{ww}\rangle$ at $\hat{z} = 0.2$, red dashed vertical line represents the sampling volume wavelength.

Figure 5.10 shows $k_x \langle \Phi_{uu} \rangle / u_*^2$ in outer scaling for tests 1.1, 1.2 and 1.3.

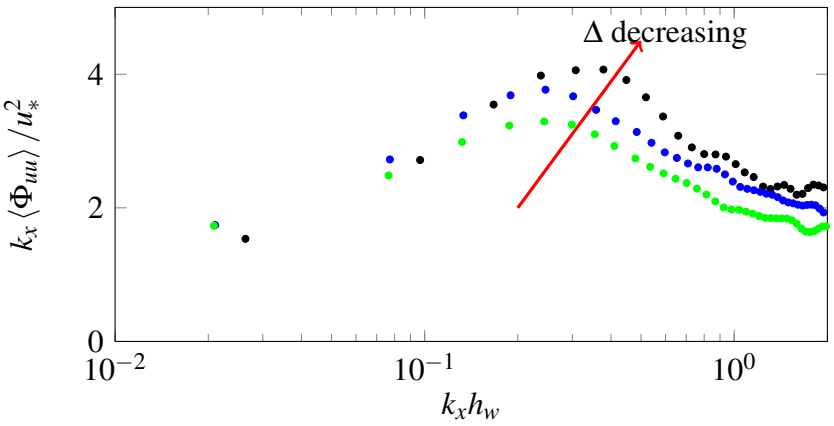


**Figure 5.10:** Comparison of $k_x \langle \Phi_{uu} \rangle / u_*^2$ at $\hat{z} = 0.2$ in test 1.1 (•), test 1.2 (•) and test 1.3 (•).

This figure is characterized by three striking features:(i) the premultiplied spectra of the longitudinal velocity fluctuations presented herein do not show a bimodal distribution showing a LS and a VLS peak; (ii) the intensity of the spectral estimates increases with decreasing relative submergence; (iii) the normalized wavenumber associated with the peak in the premultiplied spectra increases with decreasing relative submergence.

Features (i) and (ii) will be discussed in this section, whereas feature (iii) will be treated in the next one, as it requires a preamble that describes the procedure used to extrapolate the wave-numbers associated with spectral peaks.

Point (i) is at odds with results presented by Cameron et al. [19] for OCFs over rough walls. Furthermore, it is at odds with results presented for other canonical (hydrodynamically smooth) wall flows such as in pipes, channels and boundary layers, which also show the appearance of a bi-modal distribution too.

It is believed that this is unlikely to be a measurement artefact, as the ADV should be perfectly capable of capturing scales at such low frequen-

cy/wavenumbers; however it is not possible to provide a full explanation of the observed phenomenon. Usually, the appearance of VLSs is attributable to large separation between length scales characterizing the inner and outer layers. In the case of turbulent flows over rough walls, this translates in large values of the relative submergence. However, the experiments by Cameron et al. [19] and those presented herein were carried out at very similar ranges of relative submergence, meaning that this non-dimensional parameter is not appropriate to provide a reliable diagnostics of VLS occurrence. The only difference between the experiments presented herein and in Cameron et al. [19] resides in the ratio between the channel width ($B$) and the flow depth ($h_w$), which in Cameron et al. [19] ranges between 9 and 40, whereas in the present work is about 5. Cameron et al. [19] observed that the size of VLSs decreases significantly with decreasing $B/h_w$. This means that, in the experiments presented in this thesis, VLSs (if present) have perhaps reached a size, which is comparable with that of LSs and, therefore, is not detectable by spectral analysis. This hypothesis is speculative and cannot be substantiated herein. However, if verified, it would suggest that VLSs are a characteristic of "thin" wall flows, where "thin" should be interpreted as having a vertical size much smaller than the spanwise domain over which the flow develops. However, it is not clear which is the underlying physical mechanism. Why should the size of the flume interfere with VLS development?

There is an alternative explanation. Experiments in OCFs are usually carried out in flumes with relatively short length, i.e. of the order of $15 \div 20$m as in Cameron et al. [19] and in the present case. In such experiments, a turbulent boundary layer develops from the flume inlet and measurements are taken at usually $10 \div 15$m downstream of it, making sure that the boundary layer has developed enough to reach the free surface. Boundary layer development is notoriously a slow process, whereby turbulence statistics adjust to

the underlying surface very slowly (i.e. much slower than the mean velocity profile which is commonly used as the diagnostic turbulence statistics), with shear and normal Reynolds stresses being the slowest-to-adjust quantities [5, 6]. Since such stresses are the integral of spectra and co-spectra, it is plausible to assume that they also develop slowly with the boundary layer, perhaps even more slowly than their integral: in fact, energy and turbulent momentum transport, while being self-similar in their integral form, may still be subject to reshuffling among scales, while the boundary layer develops further downstream. Were the experiments carried out at fetches long enough to allow the occurrence of equilibrium boundary layer? This question still remains open. It is not possible to verify whether the boundary layer at the measurement location in both experimental setups was fully developed (in the sense of allowing the appearance of VLS), as that would require turbulence measurements over the entire length of the flume to verify self-similarity. It can be suggested that the non-dimensional parameter which drives the occurrence of VLSs is $X/h_w$ (where $X$ is the upstream fetch over which the boundary layer developed during the experiment) rather than $B/h_w$, as suggested by Cameron et al. [19], owing to the fact that this is related to a clearly defined physical mechanism, i.e. the boundary layer development. In Cameron et al. [19], $X/h_w$ ranged between 130 and 530, whereas in the present experiments it was fixed at about 50.

The lack of bimodal behavior in $k_x \langle \phi_{uu} \rangle$ occurs across the whole flow depth as shown in the premultiplied color maps reported in Figure 5.11.

This figure also confirms that in the near-wall region the flow with the lowest relative submergence is characterized by the most energetic peak in the co-spectra as already commented in point (ii). Similar considerations on point (i) and (ii) can be made on the vertical velocity spectra (Figures 5.12 and 5.13).

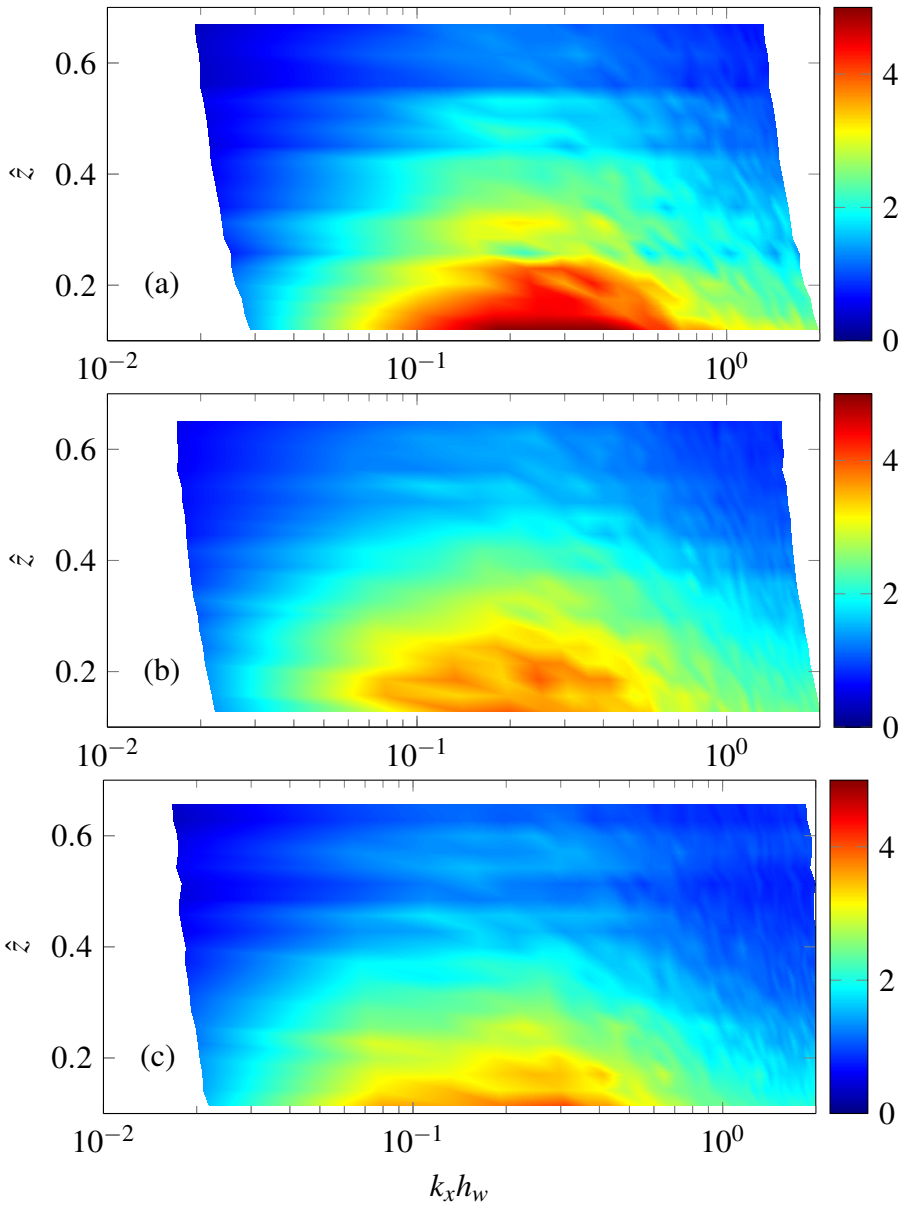


**Figure 5.11:** Premultiplied color maps of $k_x \langle \Phi_{uu} \rangle / u_*^2$. Subfigure (a) refers to the test 1.1, (b) to 1.2 and (c) to 1.3.

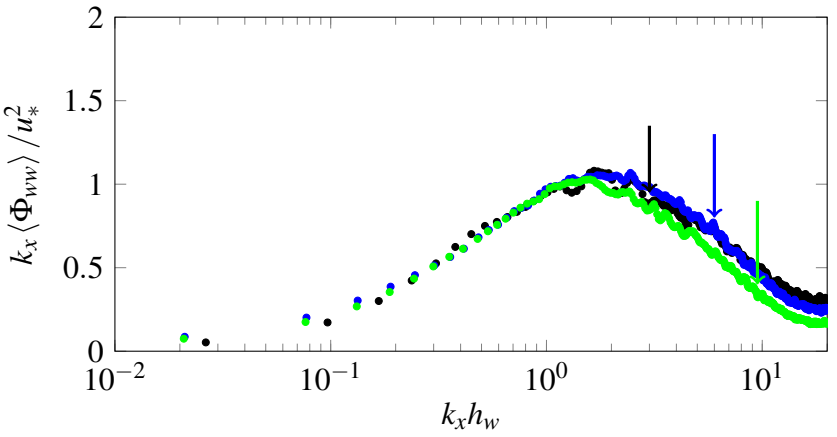


**Figure 5.12:** Comparison of $k_x \langle \Phi_{ww} \rangle / u_*^2$ at $\hat{z} = 0.2$ in test 1.1 (●), test 1.2 (●) and test 1.3 (●). Colored arrows represent the wavenumber roughness dimension in the color-related tests.

Premultiplied cospectra are reported in Figures 5.14 and 5.15. These show that co-spectra display behavior and shape similar to longitudinal velocity spectra, meaning that the near-wall peak is located at scales similar to those associated with peaks in the longitudinal velocity spectrum; the near wall peak of the lowest-submergence case is the one with the highest (normalized) energetic content. Furthermore, as per longitudinal spectra, no bimodal behavior is observed.

The similarity between longitudinal velocity spectra and cospectra was reported for atmospheric flows by McNaughton [96]. In this context, for the sake of clarity, Figure 5.16 provides an overall view of peak locations for longitudinal and vertical velocity spectra and for co-spectra. This figure confirms the alignment of spectral peaks of longitudinal spectra and co-spectra.

As regards point (ii), it is difficult to explain why the lowest submergence experiment displays the most energetic peaks in spectra and co-spectra. To this purpose, further experiments and data analysis are required.

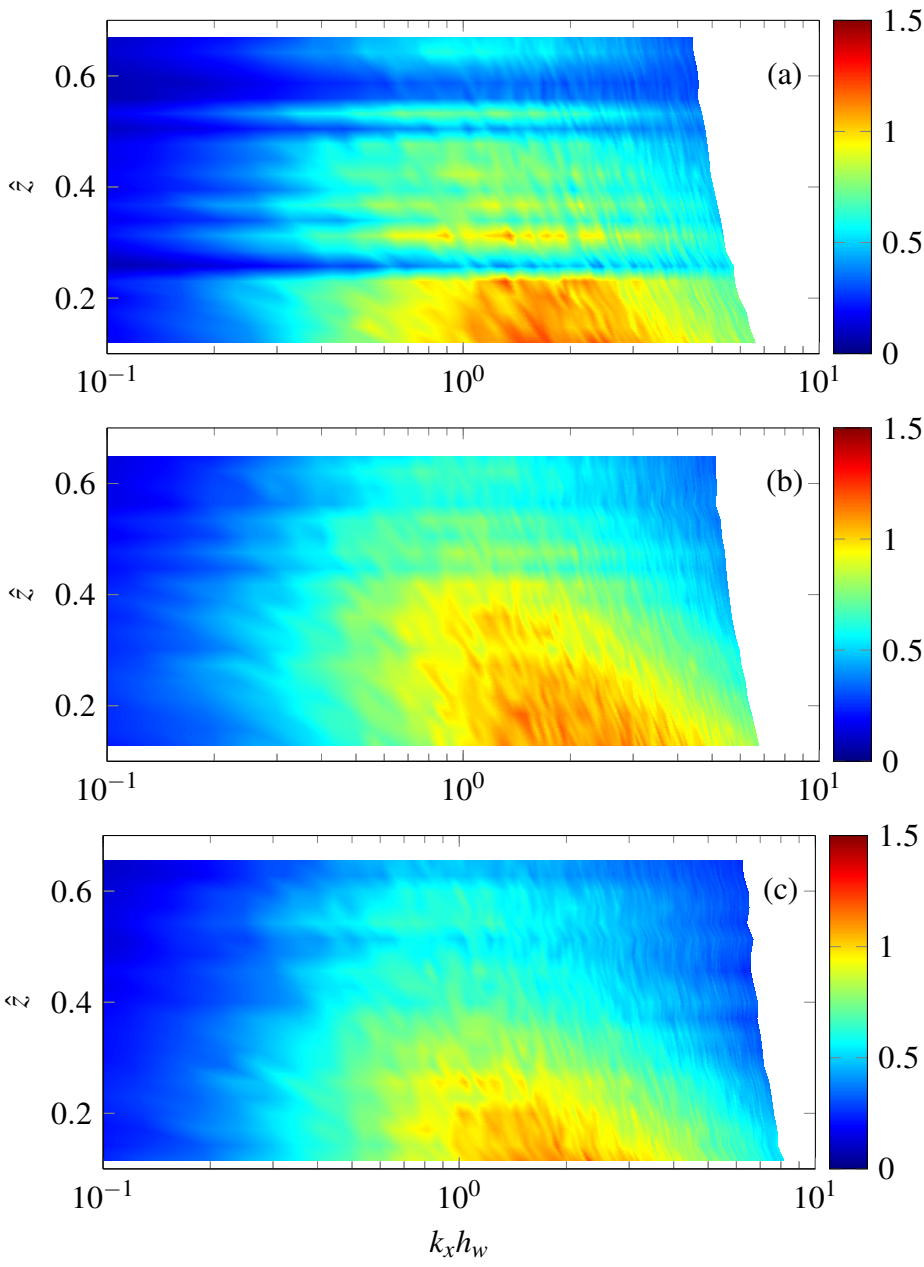


**Figure 5.13:** Premultiplied color maps of $k_x \langle \Phi_{ww} \rangle / u_*^2$. Subfigure (a) refers to the test 1.1, (b) to 1.2 and (c) to 1.3.

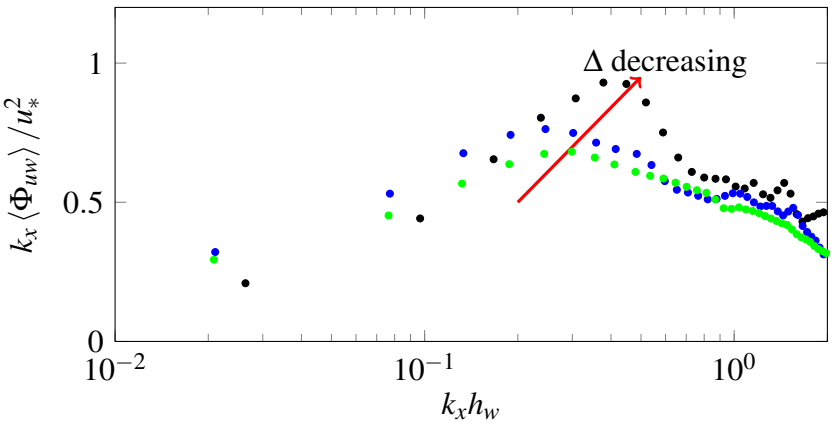


**Figure 5.14:** Comparison of $k_x \langle \Phi_{uw} \rangle / u_*^2$ at $\hat{z} = 0.2$ in test 1.1 (●), test 1.2 (●) and test 1.3 (●).

### Spectra Peaks analysis

In order to provide an in-depth analysis of LSs and their dependence on relative submergence, it is needed to define an unambiguous procedure to extract the peaks from premultiplied spectra.

The proposed procedure exploited the center of mass (CM) or centroid concept, which is briefly recalled.

The moment of a curve is the tendency to rotate around a point. Clearly, the greater the area (and the greater the distance from the selected point), the greater the moment is. In this work, the aim is to find the CM of the system, which is defined as the point which does not allow the rotation of the system itself.

The procedure consists in dividing the $k_x \langle \Phi_{uu} \rangle$ in rectangles, as reported in Figure 5.18, and in finding the abscissa associated with the CM as

$$k_{xpeak} = \frac{\sum M_i}{\sum A_i} \tag{5.9}$$

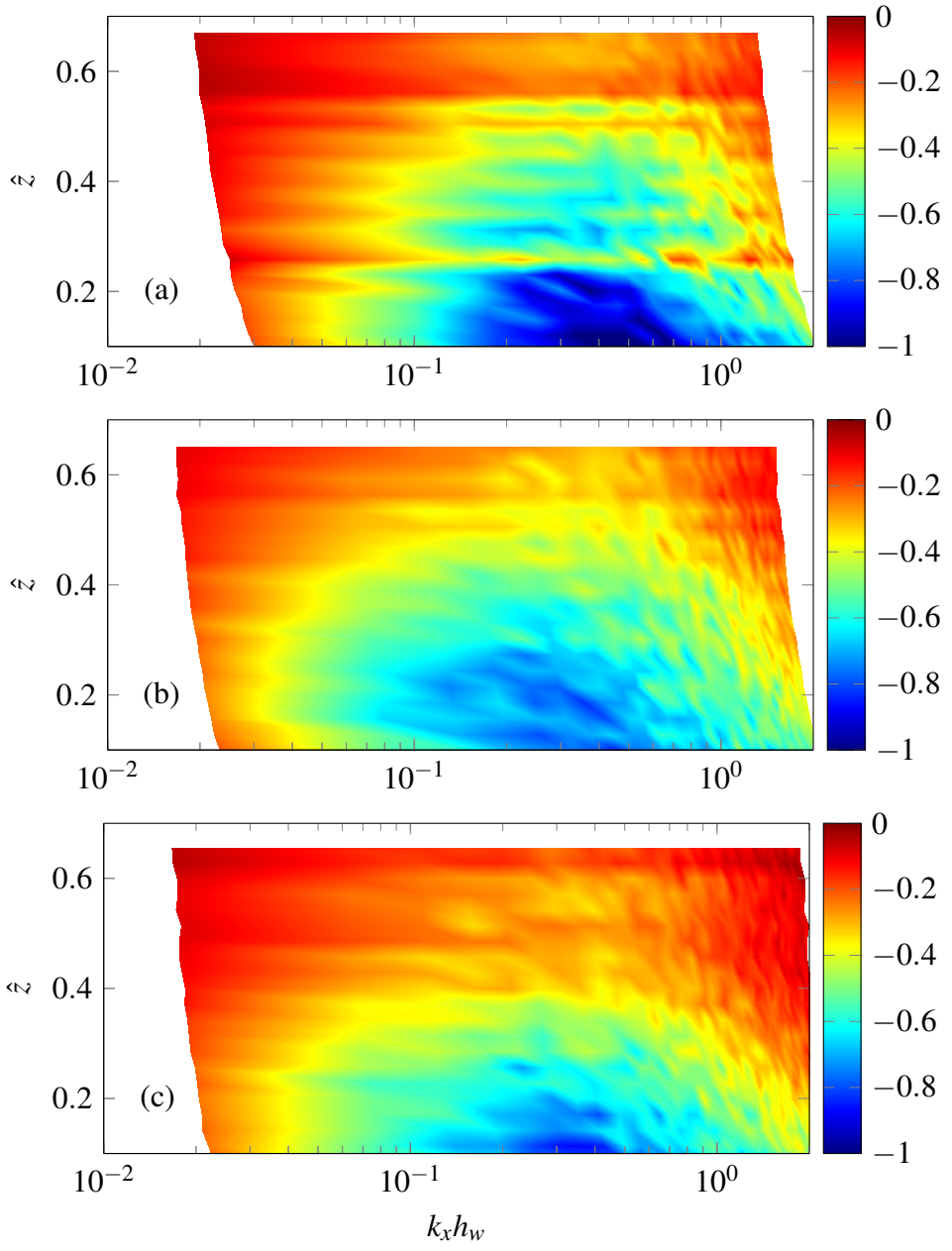


**Figure 5.15:** $k_x \langle \Phi_{uw} \rangle / u_*^2$. Subfigure (a) refers to the test 1.1, (b) to 1.2 and (c) to 1.3.

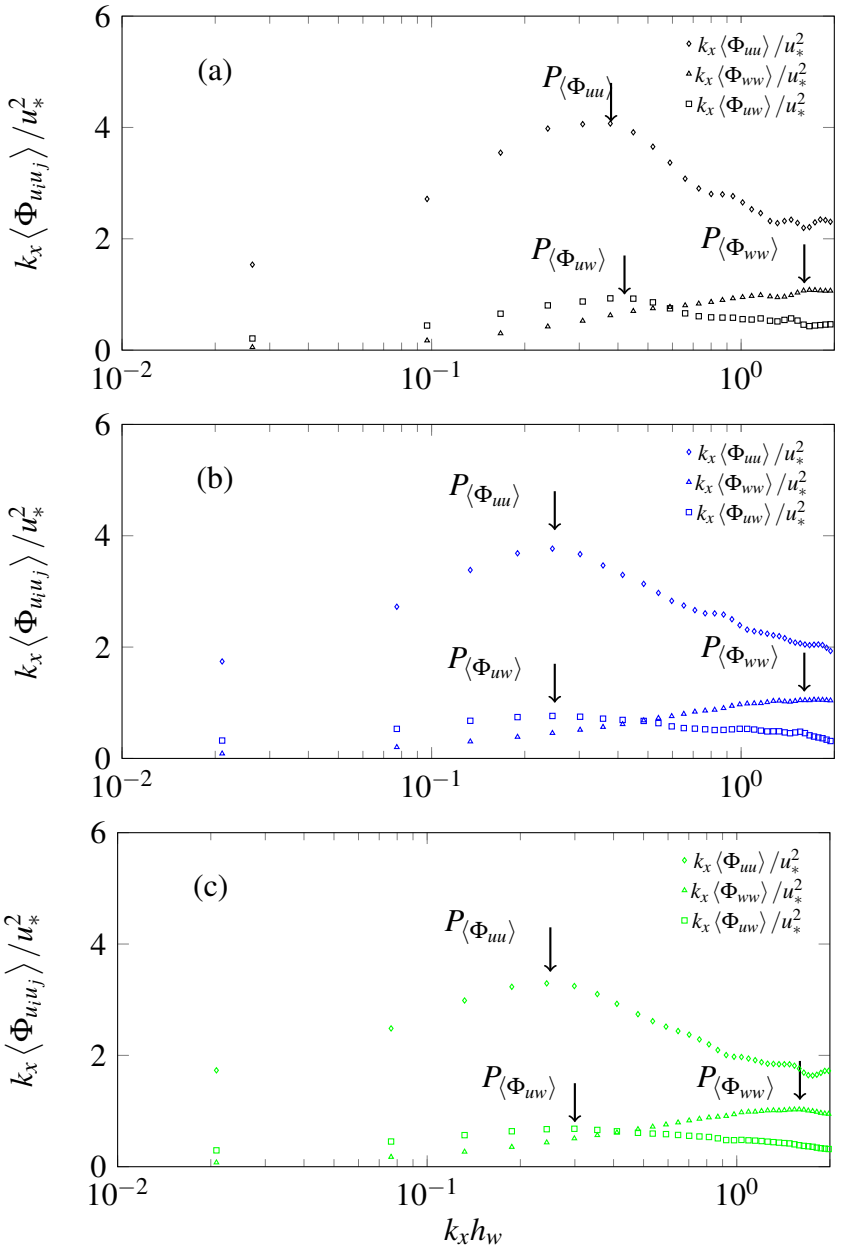


**Figure 5.16:** Comparison of spectra ($k_x \langle \Phi_{uu} \rangle / u_*^2$, $k_x \langle \Phi_{ww} \rangle / u_*^2$) and cospectrum ($k_x \langle \Phi_{uw} \rangle / u_*^2$) as a function of $k_x h_w$;(1.1) tests 1.1,(1.2) 1.2 and (1.3) 1.3.

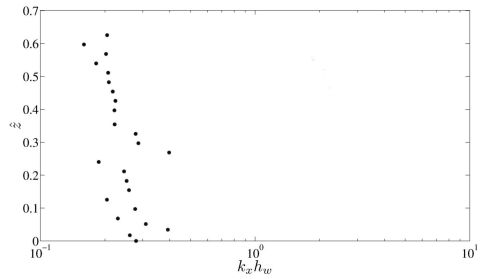


**Figure 5.17:** Maximum value position of $k_x \langle \Phi_{uu} \rangle$ versus $\hat{z}$.

where $M_i$ is the $i^{th}$ moment of the $i^{th}$ area $A_i$.

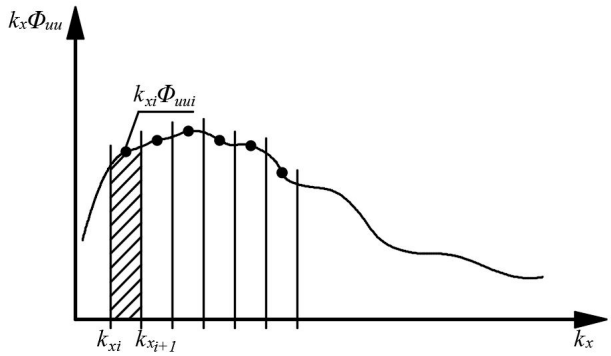


**Figure 5.18:** Center of mass calculation scheme.

The proposed procedure resulted to be very reliable in identifying spectral peaks.

Figure 5.19 (a) shows the peak distributions along $\hat{z}$ in outer scaling, namely $k_x h_w$, whereas figure 5.19 (b) reports the peak distributions in inner scaling ($k_x z$).

Both inner and outer scaling indicate that peak wavenumbers are weakly dependent on relative submergence. In outer scaling, especially for the flow region $\hat{z} < 0.3$, wavenumbers weakly decrease with increasing submergence. This is consistent with the idea that the size of near-wall turbulence structures

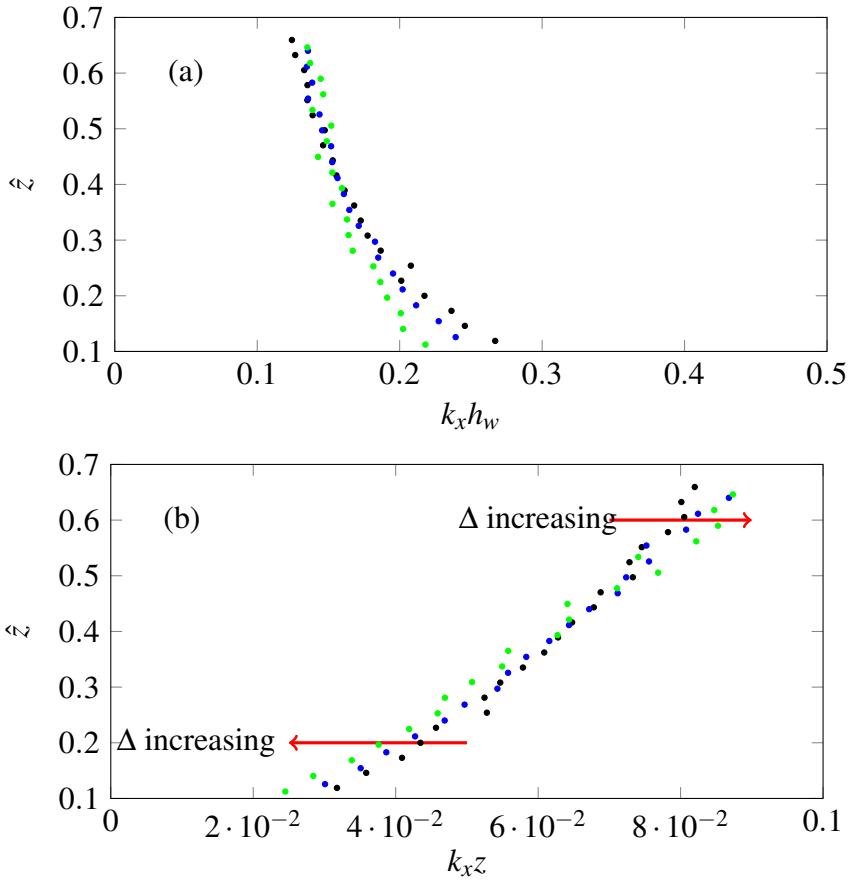


**Figure 5.19:** Outer scaling $k_x \langle \Phi_{uu} \rangle$ peaks distribution (a) and inner scaling $k_x \langle \Phi_{uu} \rangle$ peaks distribution (b), • represents test 1.1, • test 1.2 and • test 1.3.

depends on inner-outer scale separation. In inner scaling this trend is observed too. However, this is reversed at $\hat{z} > 0.3$, and this fact is difficult to be interpreted. It can be considered that these results should be taken with caution, as peak detection is difficult and the validity of the Taylor hypothesis, especially in the near-wall region, can be questionable. As expected, peaks of co-spectra behave as in the longitudinal velocity spectra; therefore, they are not commented further (see Figure 5.20).

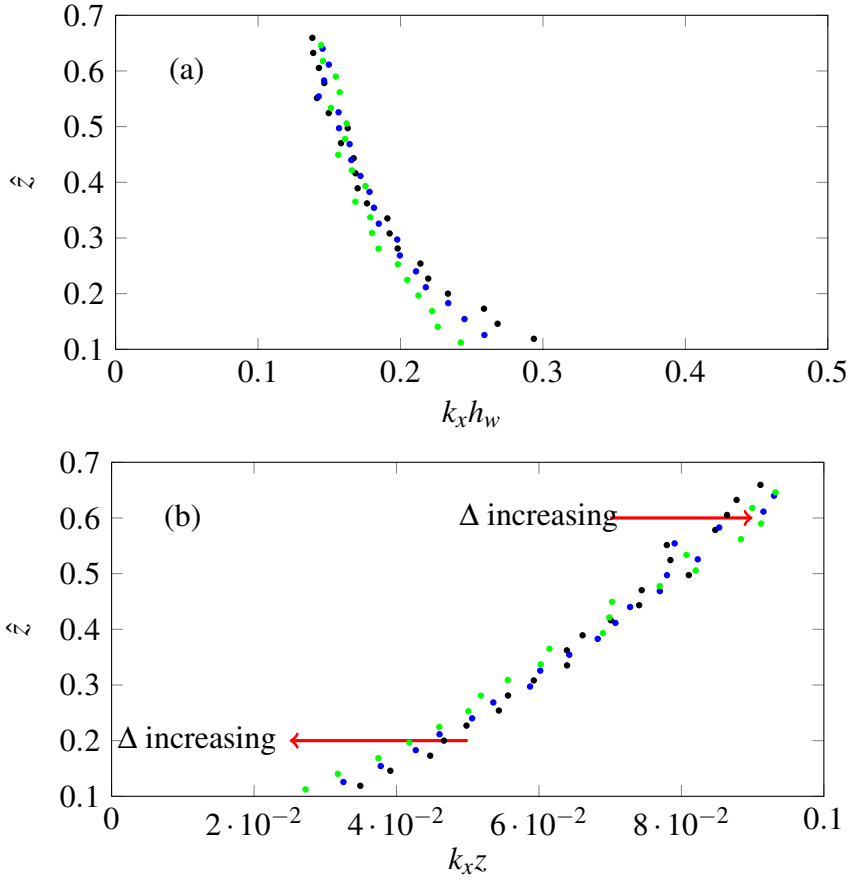


**Figure 5.20:** Outer scaling $k_x \langle \Phi_{uw} \rangle$ peaks distribution (a) and inner scaling $k_x \langle \Phi_{uw} \rangle$ peaks distribution (b), • represents test 1.1, • test 1.2 and • test 1.3.

Figure 5.21 presents the distribution of peak wavenumbers for the vertical velocity spectra in inner and outer scaling. Two comments are necessary.

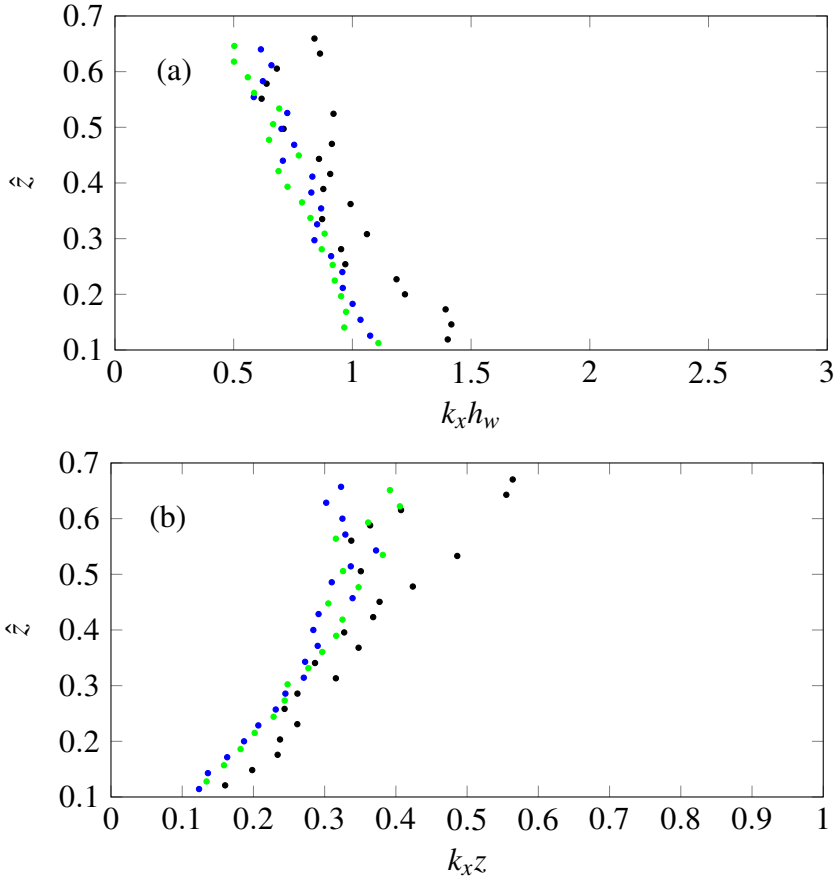


**Figure 5.21:** Outer scaling $k_x \langle \Phi_{ww} \rangle$ peaks distribution (a) and inner scaling $k_x \langle \Phi_{ww} \rangle$ peaks distribution (b), • represents test 1.1, • test 1.2 and • test 1.3.

Firstly, in inner scaling the wavenumber profile is never constant along $z$, indicating that eddies do not seem to scale with elevation over the bed or, in other words, they are not "attached" in the sense of Townsend. Secondly, peak wavenumbers associated with intermediate and highest submergence seem to overlap in both inner and outer scaling, whereas peaks associated

with the lowest submergence stand out, being much higher in both scaling. This data suggests that attached eddies do not strictly occur at the investigated submergences (or they are not the main contributors to TKE) and that the vertical dimension of energetic eddies seems to be significantly dependent on relative submergence.

The only roughly linear relationship between peak location and $\hat{z}$ was observed in test 1.1 having the smallest relative submergence, in accordance with the work of McNaughton [96], suggesting that eddies are attached to the bed surface even when their size increases up to the water depth.

# Chapter 6

# Conclusions

This thesis is aimed at adding some knowledge on the turbulence structure developed over a highly rough bed in OCFs by varying the relative submergence. Namely, three long-duration experiments were performed by using a 100 Hz ADV down-looking probe, in order to register the 3D velocity vector in each point belonging to a grid composed of 25 vertical profile of $30 \div 40$ points each. The sampling time was 300 s in each point. The velocities signals were despiked by using Goring and Nikora [59] procedure and in case of a signal severely disrupted the velocity signal were re-measured. In order to investigate different relative submergences, the bed roughness was varied by using three sediment sizes, from pebble to gravel. In this way, the relative submergence assume the values of 3.13 in test 1.1, 6.58 in test 1.2 and 10.07 in test 1.3.

First of all, averaged velocity profiles, second- and third-order moments results were discussed. These statistics were in accordance with those already observed for canonical turbulent OCFs having the same range of relative submergence.

The uniform flow condition, preliminarily checked through the comparison between the bed-slope and the water surface slope, was confirmed by the linearity of the total fluid shear stress distribution across the water column. The turbulent Reynolds stress, $-\rho \left\langle \overline{u'w'} \right\rangle$, was dominant over the roughness crest level, whereas the viscous and the form induced shear stress give a contribution in the near bed and inside the roughness gaps, respectively. In addition, while the viscous shear stress is one order of magnitude less than the turbulent shear stress, the form induced stress shows an influence equal to $\approx 30\%$ in test 1.1 and $\approx 5\%$ in tests 1.2 and 1.3. Once confident that the total shear stress follows a linear trend, the bed shear stress was extrapolated from the linear total shear stress profile, from the water surface onto the bed reference level, which is fixed at the maximum crest. Hence, by the use of the bed shear stress, the shear velocity was computed and used as the unique velocity scale.

The existence of a logarithmic velocity profile was investigated showing von Kaŕmań constant values slightly smaller than the well-known 0.41 value in the experiments which showed the lowest relative submergences. This fact prompted the author to investigate the existence of the overlap layer, which is required in order to have a universal log-law. Finally, the vertical momentum transfer was computed and a non-constant trend was observed in tests 1.1 and 1.2 suggesting the absence of an overlap layer, which is theoretically needed in order to fit a universal log-law. A clear plateau in the vertical momentum transfer was shown only in experiment 1.3, i.e. in the test with the highest submergence, confirming that a universal log-law can be observed only when there is enough scale separation between outer and inner variables. It seems that experiment 1.3 is likely to show a logarithmic layer, whereas experiments 1.1 and 1.2 definitely not. Regarding second-order moment, according to the literature [91, 89], both $\left\langle \bar{\sigma}_u \right\rangle / u_*$ and $\left\langle \bar{\sigma}_w \right\rangle / u_*$ show a linear trend, reaching

the maximum value of $2 \div 3$ at the crest level $\langle \bar{\sigma}_u \rangle / u_*$ and $\approx 1$ for $\langle \bar{\sigma}_w \rangle / u_*$. The outer layer similarity hypothesis formulated by Townsend was tested, showing a fairly well collapse of the data over $\hat{z} > 0.2$.

Within the context of spectral analysis, which was fundamental in this work, the Taylor hypothesis violation was checked through an alternative validation. It was computed comparing two time-scales, namely the LS advection time and the characteristic nonlinear time. The Taylor hypothesis resulted violated near the bed $\hat{z} > 0.1$ in test 1.1 and $\hat{z} > 0$ in tests 1.2 and 1.3, identifying a value of $\hat{z}$ under which no speculation was made in the analysis. The proposed method, based on the characteristic eddies time-scales, is more restrictive with respect the classic frozen-in Taylor hypothesis view, in which a simple comparison between the flow velocity and the fluctuation magnitude is made.

The integral length scale $\langle \lambda_c \rangle$ can be interpreted as a measure of the large-scale eddies in a turbulent flow. In this work $\langle \lambda_c \rangle$ increased with $z$ for all the experiments, showing a strong dependency on the relative submergence $\Delta$. In particular, the size of large-scale eddies in experiment 1.1. (with the lowest relative submergence) was significantly smaller than the that of large eddies in the other flow conditions, in accordance with the work of Cameron et al. [19], who found LS size of the order of $\langle \lambda_c \rangle$.

A deeper analysis of LS eddies was provided thanks to the spectral analysis which was carried out in the wave-number domain by dividing frequencies by local mean velocities as in Dennis and Nickels [37], Cameron and Nikora [18], Ferraro et al. [45]. The $k^{-5/3}$ slope observed in all the spectra at different vertical elevations confirmed that the inertial subrange is well visible at the three investigated *Re* numbers, showing a net scale separation, in which the inertial subrange was developed within a wavenumber range which was almost a logarithmic decade.

The legitimacy of the $-5/3$ scaling region was corroborated by using the third-order longitudinal velocity structure function, which, expressed as a function of TKE dissipation rate, showed a constant trend within the inertial subrange. The $4/5$-law is a sophisticated method to define the inertial subrange. The constant region of $\varepsilon$ versus $r$ is then a test of the existence of an inertial subrange and provides an estimate of the magnitude of the TKE dissipation rate.

Premultiplied spectra provide a way to quantify the contribution of different eddy-scales (peaks in the premultiplied spectra) and indicate wavelengths in which a significant amount of energy resides.

The main results are summarized as follows: (i) the premultiplied spectra of the longitudinal velocity fluctuations presented herein do not show a bimodal distribution, but an LS and a VLS peak in contrast to Cameron et al. [19]; (ii) the spectral intensity increases as the relative submergence decreases; (iii) the normalized wavenumber associated with the peak in the premultiplied spectra increases as the relative submergence decreases. Similar considerations on points (i) and (ii) can be made on the vertical velocity co-spectra.

The experiments by Cameron et al. [19] and those presented herein were carried out at very similar ranges of relative submergence, meaning that this non-dimensional parameter is not appropriate to provide a reliable diagnostics of VLS occurrence. The only difference between the experiments presented herein and in the study of Cameron et al. [19] resides in the ratio between the channel width ($B$) and the flow depth ($h_w$), which in Cameron et al. [19] ranges between 9 and 40, whereas in the present work is about 5. Cameron et al. [19] observed that the size of VLS decreases significantly with decreasing $B/h_w$. However, it is not clear what is the underlying physical mechanism. The question why the size of the flume should interfere with the VLS development

is still open. Anyway, there is an alternative explanation. Experiments in OCFs are usually carried out in flumes of relatively short length, whereas the boundary layer development is notoriously a slow process, the shear and normal Reynolds stresses being the slowest-to-adjust quantities [5, 6] as, consequently, their integral (spectra and co-spectra). Further research can be devoted to investigating whether the experiments were carried out at fetches long enough to allow the occurrence of the equilibrium boundary layer. Although in the present work no measurements were taken over the entire flume length to verify self-similarity, it can be hypothesized that the non-dimensional parameter which drives the occurrence of VLS is $X/h_w$ ($X$ being the upstream fetch over which the boundary layer developed during the test).

In order to locate the normalized wavenumber associated with the peak in the premultiplied spectra, a systematically procedure to find the correct position of these peaks is proposed. It is based on the center of mass concept, resulting very reliable in identifying spectral peaks. The results about the peaks of longitudinal velocity spectra and co-spectra suggest that both inner and outer scaling indicate that peak wavenumbers are weakly dependent on relative submergence. In outer scaling, especially for the flow region $\hat{z} < 0.3$, wavenumbers weakly decrease as relative submergence increases, but these results should be taken with caution, as peak detection is difficult. The distribution of peak wavenumbers for the vertical velocity spectra, in inner scaling, is never constant with $z$, indicating that eddies do not seem to be "attached" in the sense of Townsend. These data suggest that attached eddies are not strictly occurring at the investigated relative submergences and that the vertical dimension of energetic eddies seems to be significantly dependent on relative submergence.

## 6.1 Future Investigations and Engineering Applications

The explanation of the difference between the experiments presented herein and the study of Cameron et al. [19] about the occurrence of the VLS require further investigations. Namely, the physical mechanism suggested in Cameron et al. [19], who link the VLS development to the ratio $B/h_w$, is not clear. Moreover, an additional non-dimensional parameter which can drive the occurrence of VLS could be $X/h_w$ rather than $B/h_w$ as suggested by Cameron et al. [19], which has a clearly defined physical mechanism (i.e. the boundary layer development). To this purpose, future experiments are required to clarify the conjecture expressed before. The Kolmogorov $4/5$ law (Eq. 5.7) can be used to measure, in a reliable way, the TKE dissipation rate in any turbulent flow. It was verified that $\langle \varepsilon \rangle$ can be computed through velocity signals coming from user-friendly instruments (i.e. ADV), which can be employed in field. Hence, new scenarios of research can be opened as well as direct engineering applications. In order to make the following procedure available in engineering practice, a series of experimental campaign should be carried out. These experimental campaigns need to be focused on the definition of a rough estimator of $\langle \varepsilon \rangle$ as a function of dimensionless parameters (i.e. Reynolds number, relative submergence, and so on).

### 6.1.1 Velocity Scale

A new velocity scale can be computed exploiting the most general definition of the TKE energy dissipation rate

$$\varepsilon = \frac{\dot{u}^3}{\dot{d}}, \tag{6.1}$$

where $\dot{u}$ is a velocity associated with a length scale $\dot{d}$, $\varepsilon$ being valid in the range from the Taylor microscale $\lambda_\tau$ to the integral length scale $\lambda_c$ [53]. With this assumption, $\lambda_c$ at the bed crest level $\hat{z} = 0$ should be of the order of the maximum roughness height ($\Delta_R$); therefore, a new velocity scale can by calculated as follows:

$$\dot{u} = \sqrt[3]{\varepsilon \Delta_R}. \tag{6.2}$$

### 6.1.2 Drag Force

Manipulating the hydrodynamic drag force $F_D$

$$F_D = \frac{1}{2} C_D \rho L^2 \bar{u}^2, \tag{6.3}$$

where $C_D$ is the dimensionless drag coefficient, $\rho$ is the fluid density function, $L^2$ is the object area exposed to the flow and $\langle \bar{u} \rangle$ is the flow velocity. Furthermore, $C_D$ is a function of Reynolds number, and in particular it becomes a constant at high $Re$. Davidson [29] calculates the amount of kinetic energy distribution per unit time as

$$W = F_D \bar{u} = \frac{1}{2} C_D \rho L^2 \bar{u}^3, \tag{6.4}$$

which becomes per unit mass

$$\varepsilon = \frac{W}{\rho L^3} = \frac{1}{2} C_D \frac{\bar{u}^3}{L}. \tag{6.5}$$

Equation 6.5 is bound by the same limitations, suggesting that $C_D$ does not depend on $Re$. Applying the results obtained by the $4/5$-law [80], one can

assess the TKE dissipation rate and, then, find $C_D$ as a function of

$$C_D = \frac{2\varepsilon L}{\bar{u}^3}. \tag{6.6}$$

# Bibliography


[1] Aberle, J. (2007). Measurements of armour layer roughness geometry function and porosity. *Acta Geophysica*, 55(1):23–32.

[2] Aberle, J., Koll, K., and Dittrich, A. (2008). Form induced stresses over rough gravel-beds. *Acta Geophysica*, 56(3):584–600.

[3] Adrian, R., Meinhart, C., and Tomkins, C. (2000). Vortex organization in the outer region of the turbulent boundary layer. *Journal of Fluid Mechanics*, 422:1–54.

[4] Antohe, B. and Lage, J. (1997). A general two-equation macroscopic turbulence model for incompressible flow in porous media. *International Journal of Heat and Mass Transfer*, 40(13):3013–3024.

[5] Antonia, R. and Luxton, R. (1971). The response of a turbulent boundary layer to a step change in surface roughness part 1. smooth to rough. *Journal of Fluid Mechanics*, 48(4):721–761.

[6] Antonia, R. and Luxton, R. (1972). The response of a turbulent boundary layer to a step change in surface roughness. part 2. rough-to-smooth. *Journal of Fluid Mechanics*, 53(04):737–757.

[7] Antonia, R., Ould-Rouis, M., Anselmet, F., and Zhu, Y. (1997). Analogy between predictions of Kolmogorov and Yaglom. *Journal of Fluid Mechanics*, 332:395–409.

[8] ARPA, L. (2011). Attività di monitoraggio della qualità dell'aria: i modelli di dispersione degli inquinanti in atmosfera e le misure in atmosfera.

[9] Batchelor, G. K. (2000). *An introduction to fluid dynamics*. Cambridge university press.

[10] Batchelor, G. K. and Proudman, I. (1956). The large-scale structure of homogeneous turbulence. *Philosophical Transactions of the Royal Society of London A: Mathematical, Physical and Engineering Sciences*, 248(949):369–405.

[11] Bathurst, J. (1982). Flow resistance in boulder-bed streams. *Gravel-bed rivers: Chichester, England.*

[12] Bayazit, M. (1976). Free surface flow in a channel of large relative roughness. *Journal of Hydraulic Research*, 14(2):115–126.

[13] Bendat, J. S. and Piersol, A. (2000). Random data: Analysis and measurement procedures, john wieley & sons.

[14] Blanckaert, K. and Lemmin, U. (2006). Means of noise reduction in acoustic turbulence measurements. *Journal of hydraulic Research*, 44(1):3–17.

[15] Bray, D. (1980). Evaluation of effective boundary roughness for gravel-bed rivers. *Canadian Journal of Civil Engineering*, 7(2):392–397.

[16] Buffin-Bélanger, T., Roy, A. G., and Kirkbride, A. D. (2000). On large-scale flow structures in a gravel-bed river. *Geomorphology*, 32(3):417–435.

[17] Burkham, D. E. and Dawdy, D. R. (1976). Resistance equation for alluvial-channel flow. *Journal of the Hydraulics Division*, 102(ASCE# 12462).

[18] Cameron, S. and Nikora, V. (2008). Eddy convection velocity for smooth-and rough-bed open-channel flows: particle image velocimetry study. In *River Flow 2008, Proceedings of the International Conference on Fluvial Hydraulics, Cesme-izmir-Turkey*, pages 143–150.

[19] Cameron, S., Nikora, V., and Stewart, M. (2017). Very-large-scale motions in rough-bed open-channel flow. *Journal of Fluid Mechanics*, 814:416–429.

[20] Cellino, M. and Lemmin, U. (2004). Influence of coherent flow structures on the dynamics of suspended sediment transport in open-channel flow. *Journal of Hydraulic Engineering*, 130(11):1077–1088.

[21] Cho, J. Y., Anderson, B. E., Barrick, J. D., and Thornhill, K. L. (2001). Aircraft observations of boundary layer turbulence- intermittency and the

cascade of energy and passive scalar variance. *Journal of Geophysical Research. D. Atmospheres*, 106:32.

[22] Chow, V. (1959). *Open-channel hydraulics*. McGraw-Hill.

[23] Clauser, F. H. (1956). The turbulent boundary layer. *Advances in applied mechanics*, 4:1–51.

[24] Coles, D. (1956). The law of the wake in the turbulent boundary layer. *Journal of Fluid Mechanics*, 1(02):191–226.

[25] Cooper, J. and Tait, S. (2008). The spatial organisation of time-averaged streamwise velocity and its correlation with the surface topography of water-worked gravel beds. *Acta Geophysica*, 56(3):614–641.

[26] Cooper, J. R. and Tait, S. J. (2010a). Examining the physical components of boundary shear stress for water-worked gravel deposits. *Earth Surface Processes and Landforms*, 35(10):1240–1246.

[27] Cooper, J. R. and Tait, S. J. (2010b). Spatially representative velocity measurement over water-worked gravel beds. *Water Resources Research*, 46(11).

[28] Csanady, G. T. (2012). *Turbulent diffusion in the environment*, volume 3. Springer Science & Business Media.

[29] Davidson, P. A. (2015). *Turbulence: an introduction for scientists and engineers*. Oxford University Press.

[30] Davidson, P. A., Kaneda, Y., Moffatt, K., and Sreenivasan, K. R. (2011). *A voyage through turbulence*. Cambridge University Press.

[31] De Karman, T. and Howarth, L. (1938). On the statistical theory of isotropic turbulence. In *Proceedings of the Royal Society of London A: Mathematical, Physical and Engineering Sciences*, volume 164, pages 192–215. The Royal Society.

[32] de Lemos, M. (2006). Modeling and applications. In Amsterdam, T. N., editor, *Turbulence in Porous Media*. Elsevier.

[33] de Lemos, M. and Pedras, M. (2001). Recent mathematical models for turbulent flow in saturated rigid porous media. *J. Fluids Eng.*, 123:935–940.

[34] del Álamo, J. C. and Jiménez, J. (2003). Spectra of the very large anisotropic scales in turbulent channels. *Physics of Fluids*, 15(6):L41.

[35] Del Alamo, J. C. and Jiménez, J. (2009). Estimation of turbulent convection velocities and corrections to taylor's approximation. *Journal of Fluid Mechanics*, 640:5–26.

[36] Del Alamo, J. C., Jiménez, J., Zandonade, P., and Moser, R. D. (2004). Scaling of the energy spectra of turbulent channels. *Journal of Fluid Mechanics*, 500:135–144.

[37] Dennis, D. J. and Nickels, T. B. (2008). On the limitations of taylor's hypothesis in constructing long structures in a turbulent boundary layer. *Journal of Fluid Mechanics*, 614:197–206.

[38] Dennis, D. J. and Nickels, T. B. (2011). Experimental measurement of large-scale three-dimensional structures in a turbulent boundary layer. part 1. vortex packets. *Journal of Fluid Mechanics*, 673:180–217.

[39] Dey, S. (2014). Turbulence in open-channel flows. In *Fluvial Hydrodynamics*, pages 95–187. Springer.

[40] Dey, S. and Das, R. (2012). Gravel-bed hydrodynamics: double-averaging approach. *Journal of Hydraulic Engineering*, 138(8):707–725.

[41] Dey, S., Das, R., Gaudio, R., and Bose, S. (2012). Turbulence in mobile-bed streams. *Acta Geophysica*, 60(6):1547–1588.

[42] Dingman, S. L. (2009). *Fluvial hydraulics*. oxford university press New York.

[43] Dittrich, A. and Koll, K. (1997). Velocity field and resistance of flow over rough surface with large and small relative submergence. *Int. J. Sediment Res.*, 12(3):21–33.

[44] Ferraro, D. and Dey, S. (2015). Principles of mechanics of bedforms. In *Rivers–Physical, Fluvial and Environmental Processes*, pages 79–98. Springer.

[45] Ferraro, D., Servidio, S., Carbone, V., Dey, S., and Gaudio, R. (2016). Turbulence laws in natural bed flows. *Journal of Fluid Mechanics*, 798:540–571.

[46] Ferreira, R., Amatruda, M., Ricardo, A. M., Franca, M. J., and Di Cristo, C. (2010). Production and dissipation of turbulent kinetic energy in the roughness layer. In *Proceedings of the I European IAHR conference, Edinburgh*.

[47] Finnigan, J. (1985). Turbulent transport in flexible plant canopies. In *The Forest-Atmosphere Interaction*, pages 443–480. Springer.

[48] Finnigan, J. (2000). Turbulence in plant canopies. *Annual Review of Fluid Mechanics*, 32(1):519–571.

[49] Franca, M. and Lemmin, U. (2006). Eliminating velocity aliasing in acoustic doppler velocity profiler data. *Measurement Science and Technology*, 17(2):313.

[50] Franca, M. J. and Brocchini, M. (2015). Turbulence in rivers. In *Rivers–Physical, Fluvial and Environmental Processes*, pages 51–78. Springer.

[51] Franca, M. J., Ferreira, R. M., and Lemmin, U. (2008). Parameterization of the logarithmic layer of double-averaged streamwise velocity profiles in gravel-bed river flows. *Advances in Water Resources*, 31(6):915–925.

[52] Franca, M. J. and Lemmin, U. (2015). Detection and reconstruction of large-scale coherent flow structures in gravel-bed rivers. *Earth Surface Processes and Landforms*, 40(1):93–104.

[53] Frisch, U. (1995). *Turbulence: the legacy of AN Kolmogorov*. Cambridge University Press.

[54] Gallay, T. and Maekawa, Y. (2011). Three-dimensional stability of burgers vortices. *Communications in Mathematical Physics*, 302(2):477–511.

[55] Ganapathisubramani, B., Longmire, E. K., and Marusic, I. (2003). Characteristics of vortex packets in turbulent boundary layers. *Journal of Fluid Mechanics*, 478:35–46.

[56] Garbini, J. L., Forster, F. K., and Jorgensen, J. E. (1982). Measurement of fluid turbulence based on pulsed ultrasound techniques. part 2. experimental investigation. *Journal of Fluid Mechanics*, 118:471–505.

[57] Giménez-Curto, L. A. and Corniero, M. A. (2002). Flow characteristics in the interfacial shear layer between a fluid and a granular bed. *Journal of Geophysical Research: Oceans*, 107(C5):12–1.

[58] Giménez-Curto, L. A. and Lera, M. A. C. (1996). Oscillating turbulent flow over very rough surfaces. *Journal of Geophysical Research: Oceans*, 101(C9):20745–20758.

[59] Goring, D. G. and Nikora, V. I. (2002). Despiking acoustic Doppler velocimeter data. *Journal of Hydraulic Engineering*, 128(1):117–126.

[60] Gray, W. and Lee, P. (1997). On the theorems for local volume averaging of multiphase systems. *Int. J. Multiphase Flow*, 3:333–340.

[61] Guala, M., Hommema, S., and Adrian, R. (2006). Large-scale and very-large-scale motions in turbulent pipe flow. *Journal of Fluid Mechanics*, 554:521–542.

[62] Hardy, R. J., Best, J. L., Lane, S. N., and Carbonneau, P. E. (2009). Coherent flow structures in a depth-limited flow over a gravel surface: The role of near-bed turbulence and influence of reynolds number. *Journal of geophysical research: earth surface*, 114(F1).

[63] Hardy, R. J., Best, J. L., Lane, S. N., and Carbonneau, P. E. (2010). Coherent flow structures in a depth-limited flow over a gravel surface: The influence of surface roughness. *Journal of Geophysical Research: Earth Surface*, 115(F3).

[64] Hinze, J. (1975). Turbulence mcgraw-hill. *New York*, 218.

[65] Hofland, B. and Booij, R. (2004). Measuring the flow structures that initiate stone movement. In *River flow*, pages 821–830.

[66] Hsu, T.-J., Sakakiyama, T., and Liu, P. L.-F. (2002). A numerical model for wave motions and turbulence flows in front of a composite breakwater. *Coastal Engineering*, 46(1):25–50.

[67] Hurther, D. and Lemmin, U. (2001). A correction method for turbulence measurements with a 3d acoustic doppler velocity profiler. *Journal of Atmospheric and Oceanic Technology*, 18(3):446–458.

[68] Hurther, D., Lemmin, U., and Terray, E. A. (2007). Turbulent transport in the outer region of rough-wall open-channel flows: the contribution of large coherent shear stress structures (lc3s). *Journal of Fluid Mechanics*, 574:465–493.

[69] Hutchins, N. and Marusic, I. (2007). Evidence of very long meandering features in the logarithmic region of turbulent boundary layers. *Journal of Fluid Mechanics*, 579:1–28.

[70] Hwang, Y. and Cossu, C. (2010). Self-sustained process at large scales in turbulent channel flow. *Physical review letters*, 105(4):044505.

[71] Jiménez, J. and del Alamo, J. (2004). Computing turbulent channels at experimental reynolds numbers. *Computing*, 13:17.

[72] Kelvin, W. T. B. (1869). *On vortex motion*. Royal Society of Edinburgh.

[73] Kim, K. and Adrian, R. (1999). Very large-scale motion in the outer layer. *Physics of Fluids (1994-present)*, 11(2):417–422.

[74] Kindsvater, C. E. and Carter, R. W. (1959). Discharge characteristics of rectangular thin-plate weirs. *Transactions of the American Society of Civil Engineers*, 124(1):772–801.

[75] Kirkbride, A. (1993). Observations of the influence of bed roughness on turbulence structure in depth limited flows over gravel beds. *Turbulence: perspectives on flow and sediment transport*, pages 185–196.

[76] Kirkbride, A. D. and Ferguson, R. (1995). Turbulent flow structure in a gravel-bed river: Markov chain analysis of the fluctuating velocity profile. *Earth Surface Processes and Landforms*, 20(8):721–733.

[77] Klaven, A. (1966). Investigation of structure of turbulent streams. *Tech. Report of the State Hydro-Geological Inst.(GGI)*, 136.

[78] Koll, K. (2006). Parameterisation of the vertical velocity profile in the wall region over rough surfaces. In *River flow*, pages 163–172.

[79] Kolmogorov, A. (1941a). The Local Structure of Turbulence in Incompressible Viscous Fluid for Very Large Reynolds' Numbers. *Akademiia Nauk SSSR Doklady*, 30:301–305.

[80] Kolmogorov, A. N. (1941b). Dissipation of energy in locally isotropic turbulence. *Akademiia Nauk SSSR Doklady*, 32:16.

[81] Kraichnan, R. H. (1959). The structure of isotropic turbulence at very high reynolds numbers. *Journal of Fluid Mechanics*, 5(04):497–543.

[82] Lacey, R. J. and Roy, A. G. (2008). The spatial characterization of turbulence around large roughness elements in a gravel-bed river. *Geomorphology*, 102(3):542–553.

[83] Leopold, L., Wolman, M., and Miller, J. (1964). Fluvial processes in geomorphology wh freeman and company san francisco. *California Google Scholar*.

[84] Lhermitte, R. and Lemmin, U. (1994). Open-channel flow and turbulence measurement by high-resolution doppler sonar. *Journal of Atmospheric and Oceanic Technology*, 11(5):1295–1308.

[85] Lim, S.-Y. and Yang, S.-Q. (2006). Discussion of shear stress in smooth rectangular open-channel flows by junke guo and pierre y. julien. *Journal of hydraulic engineering*, (6):629–631.

[86] Limerinos, J. T. and of Water Resources, C. D. (1970). Determination of the manning coefficient from measured bed roughness in natural channels.

[87] MacVicar, B. and Roy, A. (2007a). Hydrodynamics of a forced riffle pool in a gravel bed river: 1. mean velocity and turbulence intensity. *Water Resources Research*, 43(12).

[88] MacVicar, B. and Roy, A. (2007b). Hydrodynamics of a forced riffle pool in a gravel bed river: 2. scale and structure of coherent turbulent events. *Water resources research*, 43(12).

[89] Manes, C., Poggi, D., and Ridolfi, L. (2011). Turbulent boundary layers over permeable walls: scaling and near-wall structure. *Journal of Fluid Mechanics*, 687:141–170.

[90] Manes, C., Pokrajac, D., and McEwan, I. (2007). Double-averaged open-channel flows with small relative submergence. *J. Hydraul. Eng.*, 133(8):896–904.

[91] Manes, C., Pokrajac, D., McEwan, I., and Nikora, V. (2009). Turbulence structure of open channel flows over permeable and impermeable beds: A comparative study. *Physics of Fluids*, 21(12):125109.

[92] Marquis, G. A. and Roy, A. G. (2006). Effect of flow depth and velocity on the scales of macroturbulent structures in gravel-bed rivers. *Geophysical research letters*, 33(24).

[93] Marquis, G. A. and Roy, A. G. (2011). Bridging the gap between turbulence and larger scales of flow motions in rivers. *Earth Surface Processes and Landforms*, 36(4):563–568.

[94] Matthaeus, W. H. and Goldstein, M. L. (1982). Measurement of the rugged invariants of magnetohydrodynamic turbulence in the solar wind. *Journal of Geophysical Research*, 87:6011–6028.

[95] McLelland, S. J. and Nicholas, A. P. (2000). A new method for evaluating errors in high-frequency adv measurements. *Hydrological Processes*, 14(2):351–366.

[96] McNaughton, K. (2004). Attached eddies and production spectra in the atmospheric logarithmic layer. *Boundary-layer meteorology*, 111(1):1–18.

[97] Mejia-Alvarez, R., Wu, Y., and Christensen, K. (2014). Observations of meandering superstructures in the roughness sublayer of a turbulent boundary layer. *International Journal of Heat and Fluid Flow*, 48:43–51.

[98] Mignot, E., Barthelemy, E., and Hurther, D. (2009). Double-averaging analysis and local flow characterization of near-bed turbulence in gravel-bed channel flows. *Journal of Fluid Mechanics*, 618:279–303.

[99] Monin, A. S. and Yaglom, A. M. (1971). Mechanics of turbulence. In Boston, editor, *Statistical fluid mechanics*. MIT Press.

[100] Monin, A. S. and Yaglom, A. M. (1975). *Statistical fluid mechanics: Mechanics of turbulence. Volume 2 /revised and enlarged edition/.* MIT.

[101] Nezu, I. and Nakagawa, H. (1993). . In Rotterdam, T. N., editor, *Turbulence in open-channel flows*. Balkema.

[102] Nezu, I. and Nakagawa, T. (1993). *Turbulence in Open-Channel Flows*. IAHR Monograph series.

[103] Nield, D. (2001). Alternative models of turbulence in a porous medium, and related matters. *TRANSACTIONS-AMERICAN SOCIETY OF MECHANICAL ENGINEERS JOURNAL OF FLUIDS ENGINEERING*, 123(4):928–934.

[104] Nikora, V. (2004). Spatial averaging concept for rough-bed open-channel and overland flows. In *Proc. Sixth Int. Conf. on Hydro-Science and Engineering, Brisbane, Australia*, volume 10.

[105] Nikora, V., Ballio, F., Coleman, S., and Pokrajac, D. (2013). Spatially averaged flows over mobile rough beds: definitions, averaging theorems, and conservation equations. *Journal of Hydraulic Engineering*, 139(8):803–811.

[106] Nikora, V. and Goring, D. (2000). Flow turbulence over fixed and weakly mobile gravel beds. *Journal of Hydraulic Engineering*, 126(9):679–690.

[107] Nikora, V., Goring, D., McEwan, I., and Griffiths, G. (2001). Spatially averaged open-channel flow over rough bed. *Journal of Hydraulic Engineering*, 127(2):123–133.

[108] Nikora, V., Koll, K., McEwan, I., McLean, S., and Dittrich, A. (2004b). Velocity distribution in the roughness layer of rough-bed flows. *Journal of Hydraulic Engineering*, 130(10):1036–1042.

[109] Nikora, V., Koll, K., McLean, S., Dittrich, A., and Aberle, J. (2002). Zero-plane displacement for rough-bed open-channel flows. In *Proc of Int Conf on Fluvial Hydraulics, River Flow 2002, Belgium*, volume 1, pages 83–91. Balkema Publishers.

[110] Nikora, V., McEwan, I., McLean, S., Coleman, S., Pokrajac, D., and Walters, R. (2007). Double-averaging concept for rough-bed open-channel and overland flows: Theoretical background. *J. Hydraul. Eng.*, 133(8):873–883.

[111] Pedras, M. H. and de Lemos, M. J. (2001). Macroscopic turbulence modeling for incompressible flow through undeformable porous media. *International Journal of Heat and Mass Transfer*, 44(6):1081–1093.

[112] Pokrajac, D., Finnigan, J., Manes, C., Mcewan, I., and Nikora, V. (2006). On the definition of the shear velocity in rough bed open channel flows. In *Int. Conf. on Fluvial Hydraulics River Flow 2006*, pages 89–98.

[113] Pokrajac, D. and Kikkert, G. A. (2011). Radins equations for aerated shallow water flows over rough beds. *Journal of hydraulic research*, 49(5):630–638.

[114] Pokrajac, D., McEwan, I., and Nikora, V. (2008). Spatially averaged turbulent stress and its partitioning. *Experiments in Fluids*, 45(1):73–83.

[115] Pope, S. B. (2000). *Turbulent flows*. Cambridge University Press.

[116] Prat, M., Plouraboué, F., and Letalleur, N. (2002). Averaged reynolds equation for flows between rough surfaces in sliding motion. *Transport in Porous Media*, 48(3):291–313.

[117] Raupach, M. and Shaw, R. (1982). Averaging procedures for flow within vegetation canopies. *Boundary-Layer Meteorology*, 22(1):79–90.

[118] Reynolds, O. (1883). An experimental investigation of the circumstances which determine whether the motion of water shall be direct or sinuous, and of the law of resistance in parallel channels. *Proceedings of the royal society of London*, 35(224-226):84–99.

[119] Rosenberg, B., Hultmark, M., Vallikivi, M., Bailey, S., and Smits, A. (2013). Turbulence spectra in smooth-and rough-wall pipe flow at extreme reynolds numbers. *Journal of Fluid Mechanics*, 731:46–63.

[120] Roy, A. and Buffin-Bélanger, T. (2001). Advances in the study of turbulent flow structures in gravel-bed rivers. *Gravel-bed river. V. Edited by MP Mosley. New Zealand Hydrological Society, Christchurch, New Zealand*, pages 375–397.

[121] Roy, A. G., Biron, P. M., Buffin-Bélanger, T., and Levasseur, M. (1999). Combined visual and quantitative techniques in the study of natural turbulent flows. *Water Resources Research*, 35(3):871–877.

[122] Roy, A. G., Buffin-Bélanger, T., Lamarre, H., and Kirkbride, A. D. (2004). Size, shape and dynamics of large-scale turbulent flow structures in a gravel-bed river. *Journal of Fluid Mechanics*, 500:1–27.

[123] Sarkar, S. and Dey, S. (2010). Double-averaging turbulence characteristics in flows over a gravel bed. *Journal of Hydraulic Research*, 48(6):801–809.

[124] Schultz, M. P. and Flack, K. A. (2009). Turbulent boundary layers on a systematically varied rough wall. *Physics of Fluids*, 21(1):015104.

[125] Schwarz, H. A. (1890). Über ein die flächen kleinsten flächeninhalts betreffendes problem der variationsrechnung. In *Gesammelte Mathematische Abhandlungen*, pages 223–269. Springer.

[126] Séchet, P. and le Guennec, B. (1999). The role of near wall turbulent structures on sediment transport. *Water Research*, 33(17):3646–3656.

[127] Shvidchenko, A. B. and Pender, G. (2001). Macroturbulent structure of open-channel flow over gravel beds. *Water Resources Research*, 37(3):709–719.

[128] Singh, K., Sandham, N., and Williams, J. (2007). Numerical simulation of flow over a rough bed. *Journal of Hydraulic Engineering*, 133(4):386–398.

[129] Slattery, J. (1999). . In Cambridge, U., editor, *Advanced Transport Phenomena*. Cambridge University Press.

[130] Smits, A. J., McKeon, B. J., and Marusic, I. (2011a). High-Reynolds number wall turbulence. *Annual Review of Fluid Mechanics*, 43:353–375.

[131] Sreenivasan, K. R. and Dhruva, B. (1998). Is there scaling in high-Reynolds-number turbulence? *Progress of Theoretical Physics Supplement*, 130:103–120.

[132] Taylor, G. I. (1935). Statistical theory of turbulence. In *Proceedings of the Royal Society of London A: Mathematical, Physical and Engineering Sciences*, volume 151, pages 421–444. The Royal Society.

[133] Taylor, G. I. (1938). The spectrum of turbulence. *Royal Society of London Proceedings Series A*, 164:476–490.

[134] Tomkins, C. and Adrian, R. (2005). Energetic spanwise modes in the logarithmic layer of a turbulent boundary layer. *Journal of Fluid Mechanics*, 545:141–162.

[135] Townsend, A. A. (1980). *The structure of turbulent shear flow*. Cambridge university press.

[136] Van Isacker, J. (1961). Generalized harmonic analysis. *Advances in Geophysics*, 7:189–214.

[137] Van Prooijen, B. C., Battjes, J. A., and Uijttewaal, W. S. (2005). Momentum exchange in straight uniform compound channel flow. *Journal of hydraulic engineering*, 131(3):175–183.

[138] van Prooijen, B. C. and Uijttewaal, W. S. (2002). A linear approach for the evolution of coherent structures in shallow mixing layers. *Physics of Fluids (1994-present)*, 14(12):4105–4114.

[139] Volino, R., Schultz, M., and Flack, K. (2007). Turbulence structure in rough-and smooth-wall boundary layers. *Journal of Fluid Mechanics*, 592:263–293.

[140] Voulgaris, G. and Trowbridge, J. H. (1998). Evaluation of the acoustic doppler velocimeter (adv) for turbulence measurements. *Journal of Atmospheric and Oceanic Technology*, 15(1):272–289.

[141] Vulpiani, A. and Livi, R. (2003). *The Kolmogorov legacy in physics*, volume 636. Springer Science & Business Media.

[142] Wang, J., Dong, Z., Chen, C., and Xia, Z. (1993). The effects of bed roughness on the distribution of turbulent intensities in open-channel flow. *Journal of Hydraulic Research*, 31(1):89–98.

[143] Wang, L.-P., Chen, S., Brasseur, J. G., and Wyngaard, J. C. (1996). Examination of hypotheses in the kolmogorov refined turbulence theory through high-resolution simulations. part 1. velocity field. *Journal of Fluid Mechanics*, 309:113–156.

[144] Wilson, N. and Shaw, R. (1977). A higher order closure model for canopy flow. *J. Appl. Meteorology*, 16:1197–1205.

[145] Yang, S.-Q. and Chow, A. T. (2008). Turbulence structures in non-uniform flows. *Advances in Water resources*, 31(10):1344–1351.

# Appendix A

# Velocity Data

## ADV measurements test

Instruments like the Acoustic Doppler Velocimeter (ADV) constrain the user to adopt many precautions before taking correct measures.

A first check is related to the misalignment of the ADV probe. In our tests, such error has been checked moving the ADV Vectrino with an automatic movement system (the Traverse System by HR Wallingford Ltd., UK) in still water. Namely, the flume was filled with water up to a certain level; then, the ADV probe was moved in the streamwise direction and it must be checked that the registered velocity signals be $u \neq V_t$, $v = 0$ and $w = 0$, where $V_t$ is the velocity of the Traverse System (see figure A.1).

A second check must be performed using the *Vectrino+* software. The *Vectrino+* mask displays:

- Signal-to-noise ratio (SNR), which should not be less than $15 \div 20$;
- Correlation, which should not be less than 70% in turbulent flows.

**Figure A.1:** Traverse System.

Moreover, the ADV requires setting the sampling frequency and volume. As a general rule, the user should operate using the minimum sampling volume height. As we can see in figure A.2, the ADV sampling volume is a cylinder having a diameter $d$ of 6.5 mm and a variable height ($1 \leq z' \leq 9.1$ mm).

Why should the user set the sampling volume height as small as possible? The answer resides into the fact that most of the known laws in turbulence must be applied in the so-called inertial subrange. Hence, the sampling volume has to be compatible with this range. Just remind that the inertial subrange is contained between the integral scale and the Kolmogorov microscale [29]

$$\eta \sim \sqrt{15} l Re^{-1/2}. \tag{A.1}$$

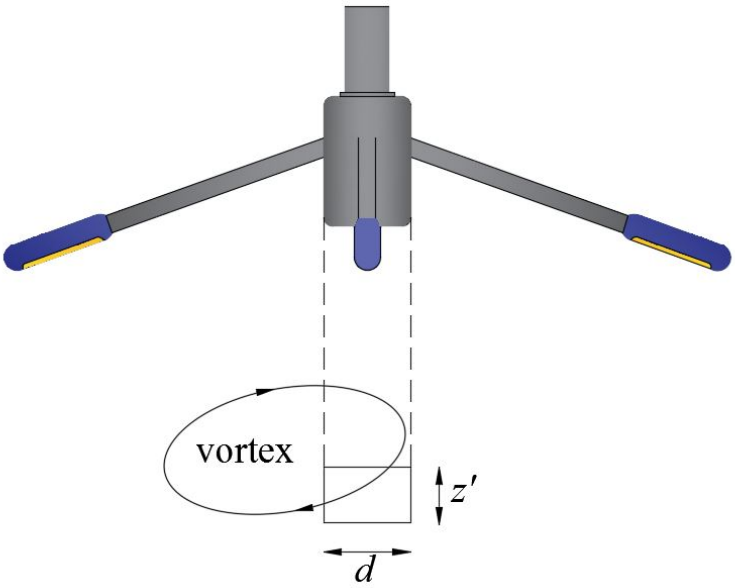


**Figure A.2:** ADV probe sampling volume.

The Kolmogorov microscale, being the lower limit of the inertial subrange, is quite difficult to reach by using laboratory instruments like ADV. Hence, we can exploit the Taylor microscale definition, which is still contained in the inertial subrange, but it is larger than the Kolmogorov one.

$$\lambda \sim lRe^{-3/4}. \tag{A.2}$$

Equation A.2 can be used to check and set a-priori the ADV sampling volume, which should be of the order of $\lambda$ to glimpse the inertial subrange.

After a careful check of these parameters, the next step is to have a look at the acquired raw velocity signals. Usually we observe signals affected by spikes, as reported in figure A.3. Goring and Nikora [59] identify these spikes as a result of a sum of problems like the Doppler noise floor, the aliasing of

the Doppler signal and the phase shift between the outgoing and incoming pulses reflected from the bed complex geometries.

According to the indication on the SNR and the correlation, the points not respecting such limit must be rejected. After this step, the Phase-Space Thresholding Method by Goring and Nikora [59] has to applied in order to despike the signals. The steps described before were implemented in Maltab, making the entire process automatic. A despiking example is reported in figure A.3.

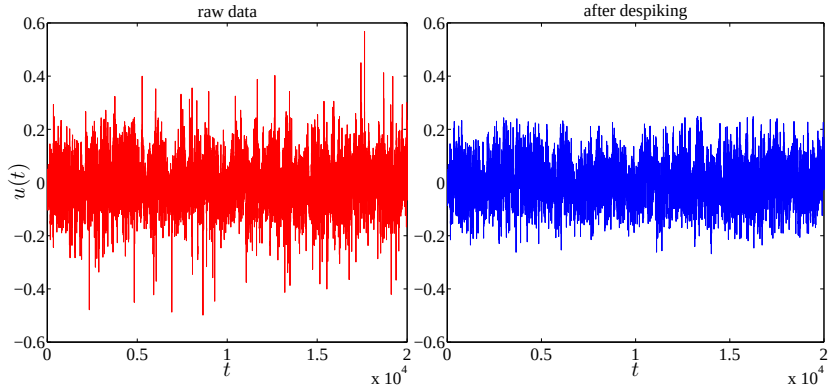


**Figure A.3:** Comparison of raw velocity signal and the velocity signal after despiking process.

Proceeding in the analysis shown in chapter 5, we notice a bulge in the spectra, which always occurs at frequencies of $10 \div 20$ Hz (see figure 5.4). Such, unexpected bulge prompted us to make further checks. First of all, a check on the ADV literature and the ADV Nortek forum was carried out. Unfortunately, there was nothing interesting for our case; only a lot of confusion on this problem reported in the ADV Nortek forum.

To be more precise the bulge was observed in the $\langle \phi_{uu} \rangle$ and $\langle \phi_{vv} \rangle$, whereas in $\langle \phi_{ww} \rangle$ it disappeared, but why? The answer to this question resides in the shape of the sampling volume, which has an equal length in streamwise $x$ as in

spanwise $y$ direction, and a different length in vertical $z$ direction, according to figure A.2.

It is a short step to find a solution. Just imagine a vortex which crosses the ADV sampling volume, having similar dimensions along the streamwise and spanwise directions. Such vortex will have a drift velocity equal to the local mean flow velocity, let's say $\bar{u}$. The interesting vortices which create the bulge in the spectra should have, at least, the same dimension of the sampling volume $d$. The relation linking these quantities to the frequency is the following one:

$$\bar{u} = d \cdot f_{bulge}, \tag{A.3}$$

from which we can calculate the bulge expected frequency

$$f_{bulge} = \frac{\bar{u}}{d}. \tag{A.4}$$

Anyway, something more can be done. As visible in the spectra of chapter "Results and Analysis", the bulge influences the spectra in a certain frequency band. Extending the previous procedure, it is still possible to individuate the bulge influence frequency band. To compute the low and high frequencies edge, the standard deviation of the velocity signal has to be evaluated, as follows

$$\bar{u} - 3\sigma_u < \bar{u} < \bar{u} + 3\sigma_u. \tag{A.5}$$

Hence, using the velocities $\bar{u} - 3\sigma_u$ and $\bar{u} + 3\sigma_u$, the frequency edges are found to be

$$f_{bulge-} = \frac{\bar{u} - 3\sigma_u}{d}, \tag{A.6}$$

and

$$f_{bulge+} = \frac{\bar{u} + 3\sigma_u}{d}. \tag{A.7}$$

An example of the bulge frequencies, computed thanks to the previous method is reported in Figure A.4.

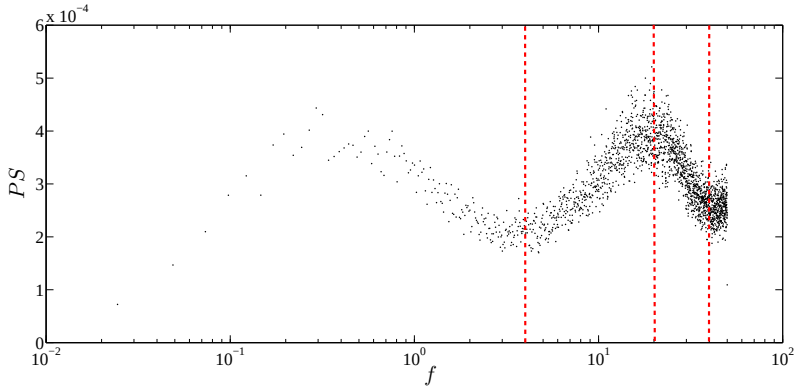


**Figure A.4:** Example of bulge frequencies calculation.

This method can be applied along the spanwise and vertical directions. Just remind that the sampling volume height is quite smaller than the streamwise and spanwise sizes, resulting most of the time appropriate to produce no bulge in the *ww* spectrum.